Imaging of intestinal inflammation and extracellular matrix changes with very small superparamagnetic iron oxide nanoparticle enhanced magnetic resonance imaging

INAUGURAL-DISSERTATION

to obtain the academic degree

Doctor rerum naturalium (Dr. rer. nat.)

submitted to the Department of Biology, Chemistry, Pharmacy

of Freie Universität Berlin

by

LAURA GOLUSDA

Berlin, 2022

This work was conducted at the Department for Gastroenterology, Infectious Diseases and Rheumatology at the Charité – Universitätsmedizin Berlin, Campus Benjamin Franklin under the supervision of PD Dr. Anja A. Kühl starting from January 2019 until December 2022.

1st Reviewer: PD Dr. Anja A. Kühl

2nd Reviewer: Prof. Dr. Sigmar Stricker

Date of disputation: March 10th, 2023

ACKNOWLEDGEMENT

DECLARATION OF ORIGINALITY

I hereby confirm that this thesis is the results of my own work and I have not used any sources or resources other than those documented by me.

I also declare that I have not submitted the dissertation in this or any other form to any other institution as a dissertation.

Hierdurch versichere ich, dass ich meine Dissertation selbstständig verfasst und keine anderen als die von mir angegeben Quellen und Hilfsmittel verwendet habe.

Die Dissertation ist in keinem früheren Promotionsverfahren angenommen oder abgelehnt worden.

_____

Laura Golusda   Berlin, December 2022

TABLE OF CONTENTS

SUMMARY

Diagnosis of inflammatory bowel diseases (IBD) often requires invasive procedures, such as endoscopy, which entails a burden for the patient. Non-invasive techniques like magnetic resonance imaging (MRI) are a desirable alternative. Currently, MRI is used to examine the small bowel in Crohn's disease patients. MRI examination of intestinal inflammation usually involves a gadolinium-based contrast agent, but recent findings question the safety of those agents. Iron oxide-based contrast agents, like very small superparamagnetic iron oxide nanoparticles (VSOPs), gained attention as a promising alternative. VSOPs were shown to have high biocompatibility and good imaging properties. Their feasibility in MRI examinations has been reported in neuroinflammatory diseases and atherosclerosis. Components within the extracellular matrix (ECM), specifically glycosaminoglycans (GAGs), seem to be involved in binding of VSOPs. Synthesis and degradation of ECM components are highly dynamic but strictly controlled in healthy tissue. During inflammation, such as in IBD, this balance can be disrupted, either resulting in excessive degradation or synthesis of ECM components. The integrity of the ECM is therefore a great indicator of inflammation and presents a promising target for diagnostics. This work presents the imaging of intestinal inflammation in three different mouse models of intestinal inflammation. VSOP-enhanced MRI successfully showed a visual and quantitative decrease in contrast in colon walls of DSS-induced colitis mice compared with wild-type mice but not in the colon walls of mice with transfer colitis and the ileum of $TNF^{\Delta ARE}$ mice. MRI examinations were found to be more sensitive in detecting early-onset inflammation compared to histopathological evaluation of colon tissue. This work hypothesizes that increasing hyaluronic acid (HA) content in colon tissue of DSS-induced colitis mice might be the reason for successful VSOP-accumulation in the DSS mouse model. In contrast, an increase in HA content is not observed in the transfer colitis model: Indeed, the results indicated that macrophages expressing the HA receptor CD44 either co-localize or phagocytose VSOPs and are present in the colon tissue of mice with DSS-induced colitis as well as to a lower extent in transfer colitis mice. This suggests a possible link between the high HA content in colon tissue and VSOP-containing CD44$^+$ macrophages. Long-term exposure to VSOPs did neither influence the phenotype nor the frequency of mononuclear cells in mesenteric lymph nodes of transfer colitis mice. Furthermore, no aggravation of tissue inflammation in liver, colon, cecum, and small intestine in VSOP-exposed animals was observed. *In vitro* experiments confirmed previous results indicating no influence on viability of VSOP-treated human primary monocytes. In summary, VSOPs successfully accumulate in inflamed tissue and do not induce cytotoxic effects. Based on the findings in this work VSOP-enhanced MRI might be a valuable alternative and could be implemented in clinical practice.

ZUSAMMENFASSUNG

Die diagnostischen Maßnahmen bei chronisch entzündlichen Darmerkrankungen (CED) beinhalten invasive Methoden, wie zum Beispiel die der Endoskopie und Koloskopie, welche eine hohe Belastung für die zu behandelnde Person darstellt. Nicht-invasive Techniken, wie die Magnetresonanztomographie (MRT), stellen attraktive Alternativen da. Das MRT wird aktuell für die Untersuchung des Dünndarms in Morbus Crohn Patienten genutzt. Die MRT Untersuchung von intestinalen Entzündungen, beinhaltet außerdem die Gabe von Gadolinium-basierten Kontrastmitteln, dessen Sicherheit aufgrund neuer Erkenntnisse angezweifelt wurde. Eisenoxid-basiere Kontrastmittel, wie zum Beispiel die „very small superparamagnetic iron oxide nanoparticles" (VSOPs), sind eine vielversprechende Alternative. VSOPs zeigen eine hohe Verträglichkeit und gute Bildgebungseigenschaften. Ihre Anwendung in MRT-Untersuchungen von neuronalen Entzündungen und Arteriosklerose wurde bereits gezeigt. Komponenten der extrazellulären Matrix (EZM), im Speziellen die Glykosaminoglykane, scheinen in der Bindung der VSOPs eine Rolle zu spielen. Die Synthese und Degradierung von EZM Komponenten ist sehr dynamisch, unterliegt jedoch einer strengen Kontrolle. Währen einer Entzündung, wie im Fall der CED, gerät das Gleichgewicht beider Prozesse außer Kontrolle, was in einer höheren Syntheserate oder aber auch exzessiver Degradierung der EZM resultieren kann. Die Integrität der EZM ist damit ein guter Indikator für Entzündungsprozesse und somit eine vielversprechende Hilfe für die Diagnose. Diese Arbeit präsentiert die Bildgebung intestinaler Entzündungen in drei unterschiedlichen Mausmodellen für CED. Die MRT-Untersuchungen mit VSOPs als Kontrastmittel zeigten einen erfolgreichen Signalabfall im Dickdarm des DSS-induzierten Mausmodells im Vergleich zu wildtypischen Mäusen, jedoch nicht in dem Dickdarm des Transferkolitis Modells und im Ileum von $TNF^{\Delta ARE}$ Mäusen. Zusätzlich zeigen die MRT-Untersuchungen eine höhere Sensitivität gegenüber der Detektion einer Entzündung im Vergleich zu der histopathologischen Evaluierung des Darmgewebes. Diese Arbeit schlägt vor, dass ein steigender Gehalt an Hyaluronsäure (HS) im Dickdarmgewebe der DSS-induzierten Kolitis der Grund für die erhöhte Ansammlung von VSOPs in diesem Model ist. Im Gegensatz dazu wurde kein Anstieg an HS in dem Transferkolitis-Modell festgestellt. Tatsächlich zeigten weitere Ergebnisse, dass Makrophagen, die den HS-Rezeptor CD44 exprimieren, mit den VSOPs kolokalisieren oder diese phagozytieren. Die Präsenz dieser CD44^{+} Makrophagen mit VSOPs im Dickdarmgewebe der DSS-induzierten Kolitis ist außerdem deutlich höher als im Gewebe der Transferkolitis, wo sie jedoch auch vorhanden sind. Dies lässt einen Zusammenhang zwischen dem hohen HS-Gehalt und der CD44^{+} Makrophagen schließen. Außerdem wurde anhand des Transferkolitis-Modells gezeigt, dass nach Gabe von VSOPs der Phänotyp und auch die Frequenz von mononukleären Zellen aus den mesenterialen Lymphknoten nicht beeinflusst

wird. Zusätzlich induzierte die Langzeitaussetzung auch keine Entzündung in Leber, Dickdarm, Blinddarm und Dünndarm dieser Mäuse. *In vitro* Experimente zeigten keinen Einfluss auf die Lebensfähigkeit von Monozyten, welche mit VSOPs behandelt worden sind. Zusammenfassend ist eine erfolgreiche Ansammlung an VSOPs im entzündeten Darmgewebe zu beobachten welche keine zytotoxischen Effekte zeigt. Basierend auf den Ergebnissen dieser Arbeit könnte eine MRT Untersuchung mit VSOPs als Kontrastmittel eine wertvolle Alternative sein und einen Gebrauch in der klinischen Praxis finden.

1 INTRODUCTION

1.1 Inflammatory bowel diseases and diagnostics

Inflammatory bowel disease (IBD) is a group of chronic recurring inflammatory disorders of the gastrointestinal tract and comprises two main forms, namely ulcerative colitis (UC) and Crohn's disease (CD). IBD is characterized by symptoms such as diarrhea, weight loss, abdominal pain and hematochezia (Guan 2019) and affects an estimate of 0.2% of the European population (Zhao et al. 2021). It is commonly accepted that in genetically predisposed individuals onset of IBD occurs during the second and third decade of life (Xavier and Podolsky 2007). Apart from genetic predispositions, environmental and microbial factors as well as excessive mucosal immune responses influence pathogenesis of IBD (Zhang and Li 2014). Pathologies and manifestations differ slightly between UC and CD.

Inflammation in UC is mainly limited to the mucosa of the colon. The process of inflammation usually starts in the rectum and continuously spreads proximal (Ordas et al. 2012). Based on location, inflammation can be restricted to the rectum (proctitis), spread beyond rectum to splenic flexure (left-sided colitis) or even reach the mucosa proximal to splenic flexure (extensive colitis; pancolitis) (da Silva et al. 2014) (**Figure 1-1, A**). Onset of UC occurs largely between 20 and 30 years of age with a second peak between 60 and 70 years (Cosnes et al. 2011).

In CD, the onset happens during age of 20-40 years with a smaller peak described in the age group 50-60 years (Molodecky et al. 2012). Inflammation in CD can occur throughout the complete gastrointestinal tract, from mouth to anus, while 40% of the cases represent inflammation in the terminal ileum (**Figure 1-1, B**) (Kaplan 2015). In CD, the inflammatory process in intestinal tissues is discontinuous and transmural (Baumgart and Sandborn 2012, Torres et al. 2017).

Early diagnosis of IBD is a significant factor in controlling disease development and predicting treatment response. Diagnosis of CD and UC does not include a single "gold-standard" procedure but is a combination of endoscopy, histological examinations of biopsies, radiology, inflammatory markers, and microbiological analysis of stool samples (Gikas and Triantafillidis 2014, Gomollon et al. 2017, Magro et al. 2017). Diagnostic procedures are mainly performed in the presence of acute symptoms. Especially endoscopy is a very invasive method. Patients suffering from IBD need to undergo endoscopy repeatedly, which is often accompanied by anesthesia. In UC, the most common endoscopic features are mucosal friability, spontaneous bleeding, and ulcerations (Magro et al. 2017). In CD, endoscopic characteristics are a patchy distribution of inflammation, skip lesions, strictures, and fistulas (Gomollon et al. 2017).

To a lesser extent several imaging techniques are applied for diagnosis and monitoring of disease. Ultrasound (US) is mainly used for follow-up examination of patients with an already existing diagnosis (Magro et al. 2017, Gomollon et al. 2017). Computed tomography (CT) combined with positron emission tomography (PET/CT) and magnetic resonance imaging (MRI) are currently the standard procedures in the clinic for assessing the small intestine in patients with CD (Golusda et al. 2021). However, CT exposes the patient to radiation and the accompanied health risks need to be considered. On the contrary, MRI uses non-ionizing electromagnetic radiation and is therefore harmless to the human body.

The technique of MRI is based on nuclear magnetic resonance, where atomic nuclei of hydrogens are exposed to a strong external magnetic field. The resulting contrast in the MR image depends then on the character of the tissue in regard to proton density and relaxation times (Yousaf, Dervenoulas and Politis 2018) but can further be influenced by adjusting the type and properties of the applied MRI sequence. The relaxation times in MRI include the longitudinal relaxation time T1, that is defined by the rate at which magnetization returns to baseline after excitation, and transverse relaxation time T2, that is defined by the rate of signal decay after excitation (Tang et al. 2018, Yousaf et al. 2018). The sequence can be adjusted by modulation of the repetition time as well as the echo time. On the one hand, sequences with short repetition time and short echo time will produce T1-weighted images (T1w) while on the other hand long repetition time and long echo time will produce T2-weighted images (T2w) (Yousaf et al. 2018). For example, in a T1w sequence where the contrast in the MR image is defined by the T1 properties of the tissue, for example cerebrospinal fluid will appear dark, while in a T2w sequence it will appear bright.

Various studies validated that in IBD disease progression, activity and mucosal lesions can be diagnosed with high accuracy by MRI (Panes et al. 2011, Florie et al. 2005, Hyun et al. 2011). For MRI examinations of small intestine, luminal contrast agents need to be applied to assure accurate diagnosis (Negaard et al. 2007). A systemic meta-analysis comparing CT with magnetic resonance enterography (MRE) with oral and intravenous contrast agents, concluded equal accuracy in the assessment of small bowel inflammation in CD (Qiu et al. 2014). Additionally, MRI is of great use to identify stenosis, fistulas and abscesses (Panes et al. 2011). However, sampling during endoscopy is limited to intestinal mucosa and does not allow broad overview, which in turn can be provided by cross-sectional imaging techniques (Bettenworth et al. 2019). In CD, up to 17-50% of patients suffer from fistulas (Nielsen et al. 2009). Formation of fistulas is most likely associated with reduced migration of fibroblasts and reduced synthesis of extracellular matrix (ECM) components in regions of ulceration (Rieder et al. 2007, Leeb et al. 2003). Stenosis is defined by an excessive production of ECM components resulting in reduction of the lumen diameter (Rieder et al. 2013). The above-

described tissue changes can be successfully detected by MRI, however diagnosis with MRI is still not used routinely in the clinic. IBD can further be accompanied by several extra intestinal manifestations. The most common extraintestinal manifestations observed in IBD patients are different classes of joint manifestation (Rogler et al. 2021). For example, axial spondyloarthropathy might occur in IBD patients, and the current gold standard for diagnosis is MRI. Here, inflammation can be visualized before bone lesions might occur (Magro et al. 2017, Braun et al. 2004, Puhakka et al. 2004). In general, MRI is already implemented as a regular procedure in CD diagnosis but would further be a great addition or even alternative in the routine of IBD diagnostics by combining advantages of being non-invasive, lacking ionization and better tissue overview due to cross-sectional imaging.
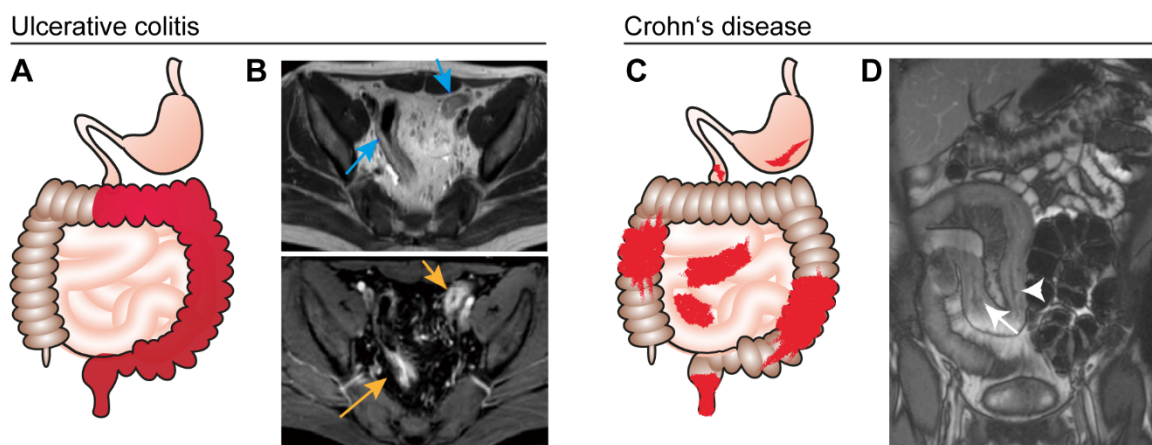
Figure 1-1: Inflammatory bowel disease (IBD) manifestations and magnetic resonance imaging (MRI). Ulcerative colitis (UC) with continuous inflammation of the colon starting from rectum visualized by red color **(A)**. Exemplary axial MRI of patient with UC involving rectum and sigmoid colon. T2w MRI without fat saturation, inflammation is indicated by blue arrows (upper image) and MRI with rapid gadolinium enhancement, inflammation indicated by orange arrows (lower image). Patient image adapted from (Yu et al. 2015) **(B)**. Crohn's disease (CD) with patchy inflammation appearing throughout the whole gastrointestinal tract illustrated by red color **(C)**. Exemplary coronal MRI image of CD patient with bowel wall thickening in the ileum. White arrowhead pointing to early ulcers in mucosa and white arrow indicating ulcer with lateral extension to submucosa. Patient image adapted from (Sinha et al. 2009) **(D)**.

1.1.1 Imaging of intestinal inflammation in mouse models

Various mouse models of intestinal inflammation are used in research and are of great importance for insights into IBD pathology. Intestinal inflammation in mice can be induced with chemical compounds, by genetic engineering, cell transfer or can occur spontaneously. For example, a colitis can be induced chemically by administration of 1-5% dextran sulfate sodium (DSS) in the drinking water. Continuous administration of DSS mimics acute inflammation, whereas termination leads to spontaneous recovery of the intestinal epithelium (Mizoguchi 2012). Apart from colonic inflammation, mice experience shortening of colon length,

hematochezia, and ulcerations. So far, few MRI studies investigating intestinal inflammation by using the DSS-induced colitis mouse model have been reported. Colon wall thickness measured with MRI in DSS-induced colitis mice was successfully correlated to different levels of inflammation severity, that were induced by differing concentrations of DSS and periods of treatment (Beltzer et al. 2016, Bianchi et al. 2016, Biton et al. 2018). A bench-top MRI is able to discriminate between DSS-treated and untreated mice (Walldorf et al. 2015). Additional to colon wall thickness, T2w signal and contrast-enhanced T1w signal were used to assess inflammation in DSS-induced colitis model (Larsson et al. 2006, Melgar et al. 2007). Breynaert *et al*. described detection of fibrotic tissue changes in DSS-induced colitis mice additional to inflammatory processes in *in vivo* MRI T2 relaxometry (Breynaert et al. 2013).

When working with models of intestinal inflammation, histomorphological evaluation of intestinal tissue is of great importance and serves as a stable reference. Erben *et al*. described a broad histopathological scoring scheme fitting the pathological appearance of inflammation in various mouse models for intestinal inflammation (Erben et al. 2014). In general, pathological scoring schemes for intestinal inflammation assess the severity and extend of inflammatory cell infiltrate and evaluate epithelial changes and mucosal architecture (Erben et al. 2014, Asseman, Read and Powrie 2003, Zimmermann et al. 2016). For chemically induced colitis models, the scoring scheme is summarized in **Table 1-1**.

An example for a cell transfer model is the transfer colitis model with adoptive transfer of naïve CD4$^+$ T cells (CD4$^+$CD45RB^{high} T cells) isolated from spleens of wild-type (WT) mice into young (6-8 weeks) immune deficient *Rag^{1tm1Mom}* mice. These mice do not harbor T and B cells and due to the lack of a regulatory T cell response in the recipient mice, the injected T cells induce a colitis through production of tumor necrosis factor (TNF) and Interferon γ (Mizoguchi 2012, Powrie and Mason 1990). Transfer colitis mice show continuous inflammation in the colon and exhibit associated hepatitis (Mathies et al. 2018). The scoring scheme or colonic inflammation mediated by disturbed immune cell homeostasis is summarized in **Table 1-2**.

A model exhibiting terminal ileitis is the *TNF^{ΔARE}* mouse model. Mice harbor a mutation in the adenosine-uracil rich elements of the 3'- untranslated region of the transcript encoding for TNF. This mutation leads to stabilization of mRNA encoding for TNF and therefore high TNF translation, leading to spontaneous inflammation in the terminal ileum of those animals starting approximately at three weeks of age (Mizoguchi 2012, Kontoyiannis et al. 1999). The scoring scheme for mouse models with small intestinal inflammation in consequence of cytokine imbalance is summarized in **Table 1-3**.

Table 1-1: <u>Scoring scheme for chemically induced colonic inflammation.</u> Adapted from Erben *et al.* 2014.

Inflammatory cell infiltrate			*Intestinal architecture*		
Severity	**Extent**	**Score I**	**Epithelial changes**	**Mucosal architecture**	**Score II**
Mild	Mucosa	1	Focal erosions		1
Moderate	Mucosa and submucosa	2	Erosions	± Focal ulcerations	2
Marked	Transmural	3		Extended ulcerations ± granulation tissue ± pseudopolyps	3
Possible sum of score I and II:					**0-6**

Table 1-2: <u>Scoring scheme for colonic inflammation mediated by disturbed immune cell homeostasis.</u> Adapted from Zimmerman *et al*. based on Asseman & Powrie. (Zimmermann et al. 2016, Asseman et al. 2003).

Mucosal infiltration	**Submucosal Infiltration**	**Epithelial hyperplasia**	**Goblet cell loss**	**Crypt abscesses**	**Area affected**	**Score**
None	None	None	None	None	None	0
Mild	Minimal, focal	Mild	Mild	Sporadic	<25%	1
Moderate	Mild	Moderate	Moderate	Few	<50%	2
Severe	Moderate, diffuse	Severe	Severe	Many	>50%	3
	severe			Crypt loss		4
	Transmural					5
Possible sum of core						**0-21**

Table 1-3: Scoring scheme for small intestinal inflammation in consequence of cytokine imbalance. Adapted from Erben *et al.* 2014.

Inflammatory cell infiltrate		*Intestinal architecture*		
Severity	**Extent**	**Epithelial changes**	**Mucosal architecture**	**Score**
Mild	Mucosa			1
Mild	Mucosa and submucosa			2
Moderate	Mucosa and submucosa	Mild hyperplasia	Mild villous blunting	3
Marked with submucosal lymphoid aggregates and granuloma	Mucosa and submucosa, sometimes transmural	Moderate hyperplasia	Moderate villous blunting	4
Marked with submucosal granuloma	Mucosa, submucosa and transmural	Marked hyperplasia	Villous atrophy, branched crypts	5
Possible sum of score				**0-5**

1.2 Contrast-enhanced magnetic resonance imaging

In IBD, specifically in CD, contrast-enhanced MRI is of great value in diagnosis of strictures and fibrosis. For this, gadolinium-based contrast agents (GBCA) are currently used in the clinical set-up. In general, in 25-30% MRI examinations a non-specific GBCA is intravenously injected into patients, inducing a positive signal in T1w MRI (**Figure 1-2, A and B**) (Aime and Caravan 2009, Jeon et al. 2021). Nevertheless, safety of GBCA has recently been called into question. Two possible reactions incurring toxicity have been reported so far. First, direct damage by gadolinium chelates in tissue or second, indirect damage due to interaction with macrophages and fibroblasts (Pasquini et al. 2018). Kanda *et al.* reported high signal intensity in brain MR images of patients long after exposure to GBCA (Kanda et al. 2014). Moreover, long-term GBCA depositions in various organs are reported by numerous studies (White, Gibby and Tweedle 2006, Flood et al. 2017, Wang et al. 2019). A possible link between nephrogenic systemic fibrosis and GBCA application was reported as well. Swaminthan *et al.* suggested that GBCA interact with CD163^{+} macrophages expressing the iron exporter ferroportin. This interaction leads to labile iron release which is reported to induce fibrosis like

in nephrogenic systemic fibrosis (Swaminathan 2016).Therefore, an alternative to GBCA is desirable.

Iron oxide-based nanoparticles (IONPs) represent a potential alternative. Different IONPs have been investigated as contrast agents for MRI and can be separated into groups based on their hydrodynamic diameter: Standard superparamagnetic iron oxide particles (SPIOs) ranging from 180-50 nm, ultra-small superparamagnetic iron oxide particles (USPIOs) ranging from 10-50 nm and very small superparamagnetic iron oxide particles with a size less than 10 nm (Weinstein et al. 2010). IONPs can be applied in T2 or T1 contrast enhancement or even T1/T2 dual-modal imagining (Chen et al. 2022). In IONPs-enhanced MRI, a T2 contrast is induced, resulting in a negative contrast change. Here, the transverse relaxation time of protons is shortened by the presence of IONPs and induces a darker image (**Figure 1-2, C and D**) (Chen et al. 2022). Further, IONPs are reported to be biodegradable and non-toxic (Jeon et al. 2021). In addition, IONPs represent long blood half-lives and flexibility in their surface coating, which can vary from simple monomer coating to a more complex polymer coating. Surface coating and size of IONPs strongly influences biocompatibility and further distribution and internalization of particles by surrounding tissues. Larger particles of >200 nm are captured by the spleen, smaller particles with a size of <10 nm are removed by renal clearance and particles between 10-100 nm mainly accumulate in the liver (Malhotra et al. 2020). Elimination of IONPs from blood circulation primarily occurs via the reticular endothelial system and mononuclear phagocytic system, again depending on size and surface coating of IONPs (Singh et al. 2010). The polymer polyethylene glycol (PEG) is the most popular polymer used for surface coating of IONPs and was reported to delay uptake by macrophages (Jokerst et al. 2011). Macrophages can polarize into pro-inflammatory macrophages, responsible for mediating inflammatory processes, or anti-inflammatory macrophages, characterized by suppressing the immune response. Several studies reported re-polarization of anti-inflammatory macrophages into inflammatory macrophages upon stimulation with neutrally charged SPIOs (Zhang et al. 2020, Zanganeh et al. 2016, Liao et al. 2021). However, a broad analysis of the different IONPs and their effect on cellular phenotype and function is still missing.

Degradation of IONPs is similar to physiological processing of iron. Consequently, IONPs might induce an increase in iron level within the organism (Ali et al. 2016). Iron overload is described as one of the main IONP-induced toxicity effects due to production of reactive oxygen species (ROS) (Geppert and Himly 2021). Up to today, the U.S. Food and Drug Administration (FDA) has approved a carbohydrate-coated IONP called ferumoxytol for treatment of iron deficiency in adults but not yet for contrast-enhanced MRI (Jeon et al. 2021, Fang et al. 2009). Nevertheless, IONPs are of use in pre-clinical investigations, like detection

of vascular inflammation associated with abdominal aortic aneurysms (McBride et al. 2016). Further, ferumoxytol was successfully used in imaging pathology of myocardial infarction and differentiating progression and pseudoprogression in glioblastoma (Yilmaz et al. 2013, Nasseri et al. 2014). In the clinic, ferumoxytol is currently used as an off-label contrast agent in MR angiography (MRA) for patients with renal failure since commercial contrast agents, that are cleared via the kidneys, induce a high burden on these patients (Dulinska-Litewka et al. 2019, Thakor et al. 2016).

Originally, the FDA approved the IONPs Resovist® and Feridex®, for contrast-enhanced MRI but withdrew the approval again due to safety concerns (Dulinska-Litewka et al. 2019). Upon IONPs application mitochondrial dysfunction, generation of apoptotic bodies and generation of ROS were reported (Singh et al. 2010). Thus, there is significant need to further investigate the influence of IONPs on the cellular and physiological level.

Smaller particles, for example very small superparamagnetic iron oxide particles (VSOPs) are currently investigated as an alternative contrast agent. VSOPs have a hydrodynamic diameter of 7 nm and an even longer blood half-life as uptake is likely not limited to cells of the mononuclear phagocytic system. In 2000, Taupitz *et al* first reported application of monomer-coated VSOPs (VSOP-C63) for MR blood pool contrast medium in MRA in rats. Their study suggests efficient first-pass MRI, due to long blood half-life of VSOPs. Followed by a subsequent equilibrium MRA (Taupitz et al. 2000). The next paragraph will summarize VSOP application and provide a concise review of the relevant literature.
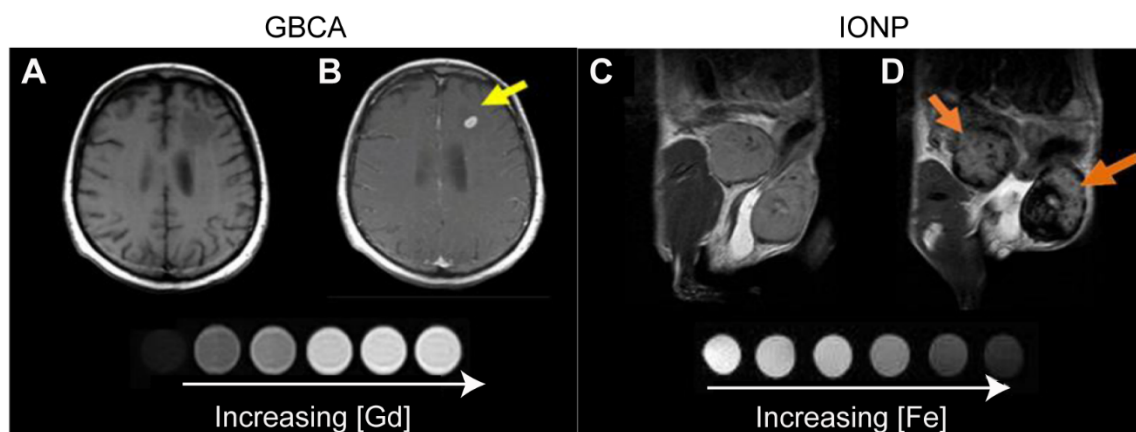
Figure 1-2: Behavior of gadolinium-based contrast agents (GBCA) and iron oxide nanoparticles (IONP) in MRI. Pre contrast **(A)** and post contrast **(B)** T1w MRI with GBCA of patient with brain metastasis. Phantom samples shown in the lower part of the GBCA panel with increasing gadolinium concentration, reflect behavior of T1 contrast agents that produce brighter contrast. Pre **(C)** and post **(D)** T2w MRI with IONPs of mouse with inflammation and mammary gland tumors. Phantom samples shown in the lower part of the IONPs panel with increasing concentration of iron (Fe) reflect behavior of T2 contrast agents that induce a decrease in signal. Image adapted from Jeon *et al.* 2021.

1.2.1 Very small superparamagnetic iron oxide particles

VSOPs are a promising alternative to commercial IONPs due to their long blood half-life and persistence in tissues after application. Instead of standard polymer coating, VSOPs are coated by a citrate monomer. Further, compared to conventional IONPs, they have a significant smaller size of 7 nm. Absorption of VSOPs mainly happens via monocytes and macrophages. VSOPs locate within the cellular vesicles and further on cellular surface and extracellular aggregates (Ludwig et al. 2013). Previous research has focused on MRA with VSOPs (Taupitz et al. 2002, Schnorr et al. 2002). Application of VSOP-C91 was reported to improve visualization of coronary arteries in cardiac MR examinations of pigs (Taupitz et al. 2002). Further, comparing the efficacy of VSOP-C184 and GBCA in first pass MRA of pigs, the differences were statistically not significant when investigating image quality, contrast and delineation of vessels (Schnorr et al. 2004). Initial trials to evaluate VSOP-C184 for coronary MRA in humans demonstrated feasibility and moderate diagnostic accuracy to detect coronary stenosis (Wagner et al. 2011). Additionally, VSOP-C184 have been further investigated in application for liver MRI. VSOP-C184 produced high contrast between liver and tumor tissues in rat liver-tumor models by shortening T2 relaxation time of healthy liver tissue and were as efficient as conventional IONPs (Schnorr et al. 2006, Kaufels et al. 2008). An additional area of interest for VSOPs is imaging of atherosclerotic plaques by MRI instead of using MRA (Wagner et al. 2013, Uca et al. 2021). Additionally, VSOP-enhanced MRI was done to assess neuronal inflammations. Here, VSOP-enhanced MRI specifically visualized brain lesions in experimental autoimmune encephalomyelitis in rats and mice, with a higher sensitivity than the conventional method.

The histological evaluations of VSOP localization showed co-localization with macrophages and dispersion within the ECM (Tysiak et al. 2009, Hunger et al. 2014). Additionally, VSOPs associate with early-onset inflammatory alterations in choroid plexus and spinal cord, even though the blood brain barrier was still intact (Millward et al. 2013). Early inflammatory processes can influence changes of the ECM. Indeed, uptake of VSOPs seems to be dependent on negatively charged components of the ECM called glycosaminogylcans (GAGs), since inhibition of GAG synthesis in a human leukemia monocyte cell line (THP-1 cells) *in vitro* dampened VSOP uptake (Ludwig et al. 2013). *In vitro* experiments in brain endothelial cells further underscored impaired uptake upon GAG degradation and synthesis inhibition (Berndt et al. 2017).

Additional to conventional intravenous application of contrast agent, cells can be labeled with nanoparticles and be applied intravenously for subsequent imaging. VSOP-labeled spleen-derived mononuclear cells or multipotent mesenchymal stromal cells successfully engrafted and migrated into the mouse brain *in vivo* (Stroh et al. 2006, Coquery et al. 2012). VSOPs can

further be coupled to proteins in order to specifically target biological processes like apoptosis and protease-activity, which can then be visualized by MRI (Schellenberger et al. 2008b, Schellenberger et al. 2008a). Schellenberger *et al.* developed VSOPs doped with europium for straightforward detection of VSOP distribution in tissues by fluorescence microscopy (de Schellenberger et al. 2017) and laser ablation inductively coupled mass spectrometry (LA-ICP-MS) (Scharlach et al. 2016, Uca et al. 2021). With this modification conventional iron quantification methods can be avoided when aiming specific quantification of VSOPs. This is crucial as conventional iron quantification methods would also quantify intrinsic iron and thus falsify the results. Additional to detection with fluorescent microscopy (de Schellenberger et al. 2017, Berndt et al. 2017) and LA-ICP-MS, a technique called imaging mass cytometry (IMC) can detect VSOPs intercalated with europium within tissue sections. Silva *et al*. applied IMC to visualize VSOPs doped with europium in inflamed brain tissue of mice. With additional staining of tissue by metal isotope-conjugated antibodies, they further characterized co-localization of particles with inflammatory sites (Silva et al. 2021).

So far, VSOPs are mainly used in research but have been tested in phase I and phase II trials for clinical application. Especially, evaluation of toxicity is of importance for further clinical use. *In vitro* VSOP labeling of neural stem cells or adipose tissue derived stromal cells does not influence viability, physiology and stemness of cells (Stroh et al. 2019, Radeloff et al. 2020). Nevertheless, a concentration-dependent genotoxic effect in human adipose tissue-derived stromal cells has been reported (Radeloff et al. 2021). However, this is only true for *in vitro* studies on VSOP-exposed cells. In case of intravenous VSOP application, cells are exposed to a lower concentration of VSOPs. Lethality in mice and rats following administration of an acute single dose occurs within the first 24 hours with doses that exceed the potential clinically administered dosage in patients by a factor of 230 (Wagner et al. 2002). A clinical phase I evaluation of VSOPs revealed a drop in both blood pressure and oxygen saturation in two participants at a VSOP dose of 0.075 mmol Fe/kg. Further, iron metabolism parameters show short-term and dose-related changes (Taupitz et al. 2004).

In summary, VSOP-enhanced MRI is studied in inflammatory diseases like atherosclerosis and various neurological inflammations. However, uptake and long-term influence of the particles, especially in patients has yet to be clarified.

1.3   Mononuclear phagocyte system in intestinal immunity

The mononuclear phagocyte system, originally described by van Furth in 1968, comprises dendritic cells (DC), monocytes and macrophages (Ginhoux and Jung 2014). Their common precursors are the hematopoietic stem cells (HSCs) in the bone marrow (Bassler et al. 2019). HSCs can then differentiate into monocytes, which further give rise to monocyte-derived

macrophages, monocyte-derived dendritic cells, or inflammatory monocyte-like cells. Additionally, tissue-resident macrophages and different classes of dendritic cells that originate from a precursor DC (pre-DC) exist as well (Joeris et al. 2017, Chapuy and Sarfati 2020). Cells of the mononuclear phagocyte system play a pivotal role in tissue homeostasis as well as during inflammation in the intestine. Within the intestine these cells locate in the lamina propria as well as the draining lymph nodes in the mesentery. At the site of the mesenteric lymph nodes (mLN), immune tolerance is promoted by the presentation of antigens to lymphocytes (Randolph et al. 2017, Esterhazy et al. 2019). Within the lamina propria, conventional dendritic cells (cDC), located underneath the intestinal epithelium support tolerance to dietary antigens (Chapuy and Sarfati 2020). Additionally, monocytes are recruited to the lamina propria where they differentiate into macrophages that contribute to tissue homeostasis by production of interleukin 10 (IL-10) that in turn contributes to maintenance of Foxp3$^+$ regulatory T cells (Treg) (Chapuy and Sarfati 2020, Joeris et al. 2017). The following paragraphs describe the classification and function of cells from the mononuclear phagocyte system with regard to intestinal immunity in more detail.

1.3.1 Monocytes

Monocytes represent 10-20 % of mononuclear cells within the blood circulation where different subgroups of monocytes can be found (Haniffa, Bigley and Collin 2015, Ginhoux and Jung 2014). In humans, monocytes can be classified into three subgroups: classical CD14^{++}CD16$^-$, intermediate CD14^{++}CD16$^+$ and non-classical CD14$^+$CD16^{++} monocytes (Ziegler-Heitbrock et al. 2010).

Classical monocytes are pro-inflammatory, highly phagocytic and further express higher levels of chemokine receptor 2 (CCR2) which is important for their migratory function (Kapellos et al. 2019). Intermediate monocytes are anti-inflammatory and participate in antigen presentation and T cell stimulation and the non-classical monocytes patrol the endothelium in homeostasis and are able to clear apoptotic cells (Tahir and Steffens 2021). Expression level of human leucocyte antigen receptor (HLA-DR), CD86 and CD206 can further help for their classification as elevated HLA-DR and CD86 expression is reported in non-classical and intermediate monocytes when compared to classical monocytes (Kapellos et al. 2019). The expression of the mannose receptor CD206 is also associated with differentiation of monocytes towards macrophages, while high expression of CD206 is associated with alternatively activated macrophages (Jaynes et al. 2020).

Expression of different proteins further leads to distinct functions of the monocyte sub-groups. In the context of inflammatory processes, various studies show monocyte differentiation into pro-inflammatory macrophages that can switch to alternatively activated macrophages

depending on environmental context (Atri, Guerfali and Laouini 2018, Italiani et al. 2014, Rackov et al. 2016).

In mice, monocyte subsets can be subdivided by expression level of lymphocyte antigen 6 complex (Ly6C), CCR), C-X3-C motif chemokine receptor 1 (CX$_3$CR1) and integrin lymphocyte function associated antigen-1 (LFA1) on their surface. Consequently, monocytes in mice are subdivided into classical Ly6C^{high}CCR2^{high}CX$_3$CR1^{low} monocytes and patrolling or non-classical Ly6C^{low}CCR2^{low,} CX$_3$CR1^{high}LFA1$^+$ monocytes (Ziegler-Heitbrock et al. 2010, Auffray et al. 2007, Narasimhan et al. 2019). However, it was reported that Ly6C^{low} monocytes might originate from Ly6C^{high} monocytes within the bone marrow and spleen (Tahir and Steffens 2021, Yona et al. 2013). Ly6C^{low} monocytes thus, equivalent to human non-classical CD14$^+$CD16^{++} monocytes, reside in the lumen of the vasculature and patrol endothelial integrity (Ginhoux and Jung 2014). On the other hand, Ly6C^{high} monocytes, as well as their human equivalent classical CD14^{++}CD16$^-$ monocytes, are rapidly recruited to sites of inflammation in various tissues (Ginhoux and Jung 2014). Within these tissues, Ly6C^{high}CCR2^{high}CX$_3$CR1^{low} monocytes can differentiate into monocyte-derived macrophages or monocyte-derived dendritic cells, depending on stimulus and location.

1.3.2 Macrophages

In the intestinal tissue, infiltrating Ly6C^{high} monocytes can be exposed to different stimuli. These stimuli will decide their cell fate and impact on further differentiation and functionality. Monocyte-derived macrophage can contribute to the inflammatory response, triggering further inflammatory processes, but can also resolve inflammation, depending on tissue context. In homeostasis, after entering the lamina propria, Ly6C^{high} monocytes start expressing major histocompatibility complex II (MHCII) and lose their Ly6C expression, followed by an upregulation of CX$_3$CR1, F4/80 and CD64 (Na et al. 2019). Monocyte-derived macrophages expressing these surface receptors can contribute to increased synthesis of anti-inflammatory cytokines like IL-10, present a higher phagocytic activity and acquire scavenger receptors (Na et al. 2019). The constant IL-10 production of intestinal macrophages during homeostasis stimulates differentiation of T cells into Foxp3$^+$ Treg cells (Krause et al. 2015).

Nevertheless, in the presence of tissue damage, recruited Ly6C^{high} monocytes can also be activated by pathogen-associated molecular patterns (PAMPs). Instead of differentiating into mature macrophages Ly6C^{high} monocytes then become Ly6C^{high}CX$_3$CR1^{int}MHCII$^{+/-}$ inflammatory-like monocytes and produce pro-inflammatory cytokines like IL-12, IL-23 and IL-1β (Joeris et al. 2017). These cytokines induce T helper (T$_H$) 1 and T$_H$17 cell responses, which further drive the inflammatory cascade (Na et al. 2019). Studies show that the population of intestinal macrophages in the lamina propria depends on constant replenishment by Ly6C^{high}-infiltrating monocytes (Bain and Mowat 2014, Bain et al. 2013). However, Hashimoto *et al.*

suggest an embryonic population with a capability of self-renewal. This population does not rely on the constant recruitment of Ly6C^{high} monocytes into the tissue and has the ability of local self-maintenance (Hashimoto et al. 2013, Ginhoux et al. 2010). Which of these theories is true needs further validation.

In humans, the macrophage populations in the intestine are less well characterized than in mice. It is thought that during homeostasis the majority of macrophages in the lamina propria are CD14^{low}CD11b$^+$CD163$^+$CD209$^+$ and CD11c$^-$ and produce IL-10. However, during inflammation, equivalent to the above-mentioned process in mice, CD14^{++}CD16$^-$ monocytes that get recruited to the intestine do not fully mature into macrophages as during tissue homeostasis. Recruited immature macrophages are responsible for the production of pro-inflammatory cytokines such as IL-23, TNF-α and IL-1 (Joeris et al. 2017, Kamada et al. 2008).

1.3.3 Dendritic cells

A high number of intestinal DCs are located within Peyer's patches (PP) and mLN but are also distributed through the lamina propria (Joeris et al. 2017). Their main function in the intestine is the presentation of antigens and stimulation of naïve T cells via MHCII or MHCI and co-stimulatory molecules (Rutella and Locatelli 2011). DC are described to be the most potent antigen presenting cells (APC), while they not only reside in the lamina propria but further are capable to migrate to mLN for T cell stimulation (Bernardo, Chaparro and Gisbert 2018). In mice, dendritic cells are subdivided into three major groups: CD11c$^+$CD11b$^-$CD8α$^+$CD103$^+$ conventional dendritic cell type 1 (cDC1), CD11c$^+$CD11b$^+$CD103$^+$CD172a$^+$ cDC2 and plasmacytoid DCs (pDCs) (Sun, Nguyen and Gommerman 2020, Guilliams et al. 2014). pDC mature within the bone marrow before they enter the blood stream and are identified in mice by CD11c^{low}, MHCII^{low}, B220$^+$ and Singlec-H$^+$. Pre-DCs migrate into tissues or lymphoid organs where they finish differentiation (Waisman et al. 2017).
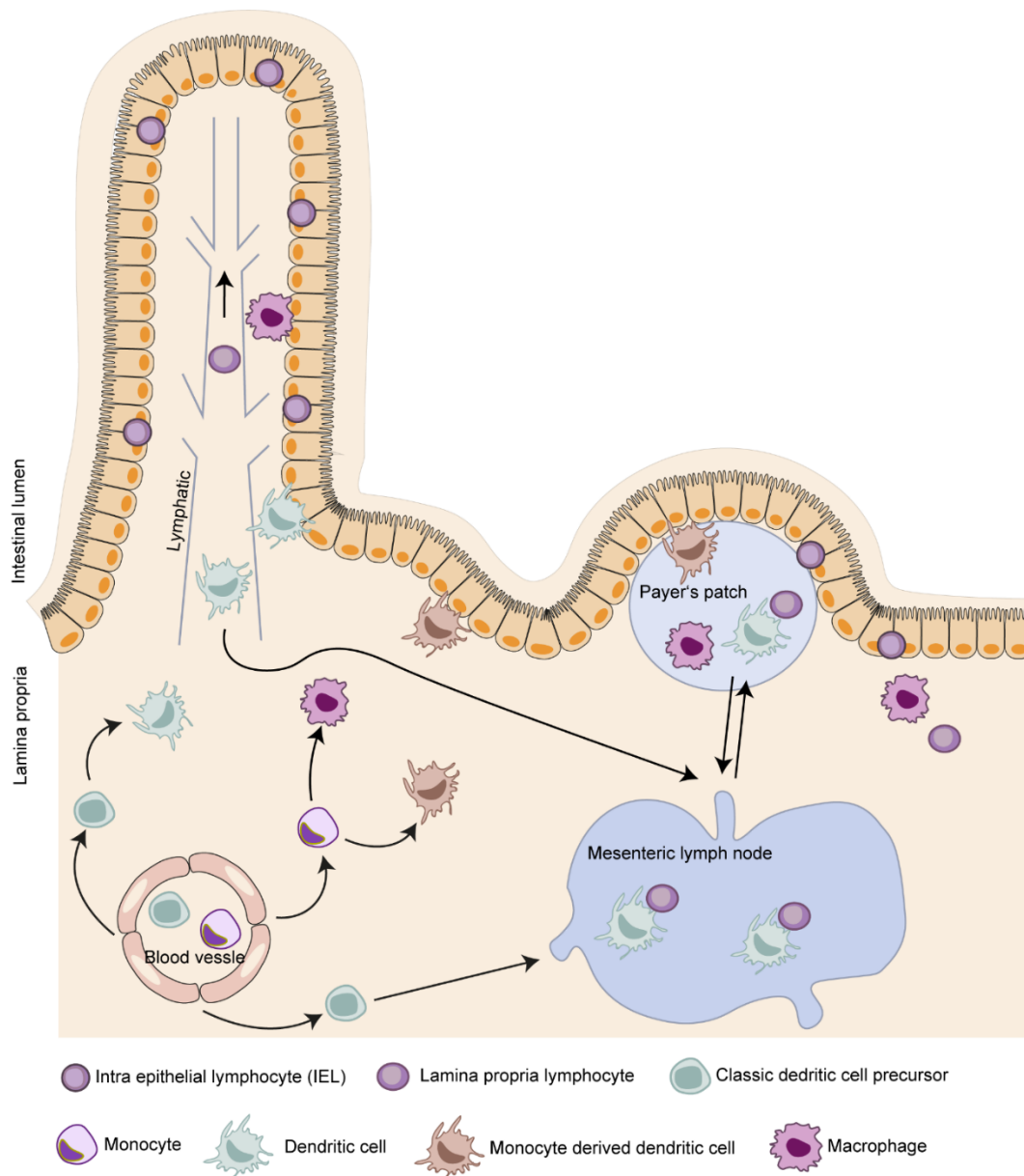
Figure 1-3: <u>Overview of mononuclear phagocyte system in healthy intestinal immune system.</u> The gut-associated lymphoid tissue (Peyer's Patches and mesenteric lymph nodes (mLN)) together with the epithelium and lamina propria compose the intestinal immune system. Cells of the mononuclear phagocyte system are ubiquitously localized within those compartments. Dendritic cell (DC) precursors and monocytes migrate via blood-vessel endothelium into intestinal tissue. Here, monocytes differentiate via various stimuli to either CX_3CR1^+ $F4/80^+$ $CD64^+$ macrophages or CX_3CR1^+ monocyte derived DCs that can penetrate the epithelium. Recruited classical DC precursor differentiate to lamina propria $CD103^+$ DCs. DCs can reside in in the lamina propria or migrate to mLN and activate naïve T cells to promote antigen specific tolerance or protective immunity. Figure was adapted from Varol *et al.* and Wu *et al.* (Wu et al. 2014, Varol, Zigmond and Jung 2010).

1.4 Extracellular matrix in intestinal inflammation

Tissue integrity and support is provided by the extracellular matrix (ECM). It is broadly accepted that the ECM plays a pivotal role in tissue homeostasis, involving cellular processes like proliferation, differentiation, migration, and inflammation. A balance in synthesis and degradation of the ECM is crucial to maintain a healthy intestinal barrier. In mammals, the ECM is defined by the "core matrisome", which includes about 300 proteins including fibrous proteins (collagens, laminins, elastins and integrins) and proteoglycans that are linked to glycosaminoglycans in addition to ECM-associated proteins, enzymes and growth factors (Hynes and Naba 2012). The ECM can be subdivided into the basement membrane and interstitial matrix. In the intestine, the basement membrane is located underneath the epithelial cell layer and the interstitial matrix is based in the lamina propria and submucosa (Mortensen et al. 2019). In healthy conditions, the epithelial cells are organized in an apical to basal manner, while the basal side is in close contact with the basement membrane. The interstitial matrix is a more loose structure underneath the basement membrane. (**Figure 1-4**).
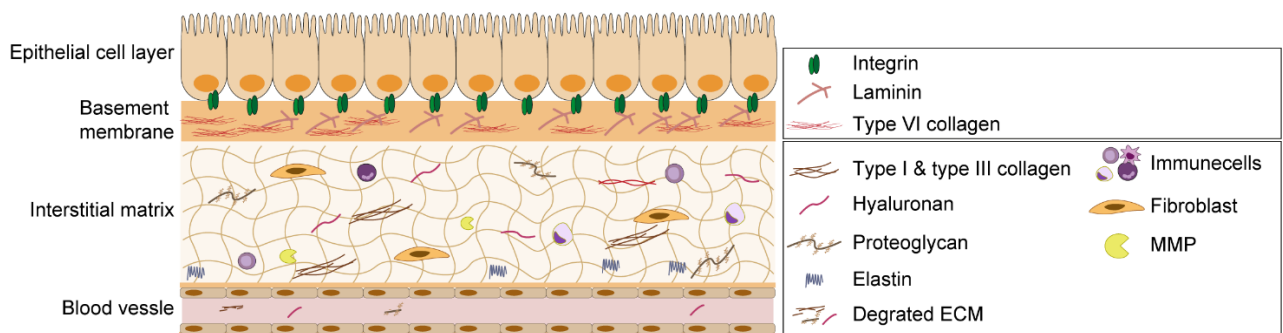
Figure 1-4: <u>Extracellular matrix (ECM) in healthy conditions.</u> Epithelial cell layer with apical side facing the lumen and basal part connected to the basement membrane via integrins followed by interstitial matrix. Blood vessel with endothelial cells lining the vessel. Components of ECM stated within the legend. MMP: matrix metalloproteinases. Figure adapted from Frantz, Stewart and Weaver 2010.

Injury of the epithelial cell layer triggers inflammatory processes and induces epithelial to mesenchymal transition (EMT) of epithelial cells. This leads to tissue infiltration by immune cells, such as macrophages. Infiltrating macrophages release cytokines that can activate fibroblasts, resulting in their differentiation into myofibroblasts (**Figure 1-5, A**). Myofibroblasts in the interstitial matrix produce excessive amounts of ECM components including collagen. (Karsdal et al. 2017, Bonnans, Chou and Werb 2014). Further, these cells produce matrix-degrading enzymes called matrix metalloproteinases (MMPs) which are the main enzymes responsible for matrix degradation. Consequently, these processes culminate in an imbalance in synthesis and degradation of the ECM.

Excessive degradation of matrix components by MMPs at the site of inflammation might result in fistulas, a common complication in IBD (**Figure 1-5, B**). In contrast to this, inflammation can also trigger synthesis of ECM components, leading to excessive ECM accumulation and this can result in fibrosis (**Figure 1-5, C**) (Hu et al. 2007, Derkacz et al. 2021b, Bonnans et al. 2014, Latella et al. 2015). The following paragraphs will focus on components of the ECM and emphasize their roles in IBD pathogenesis.
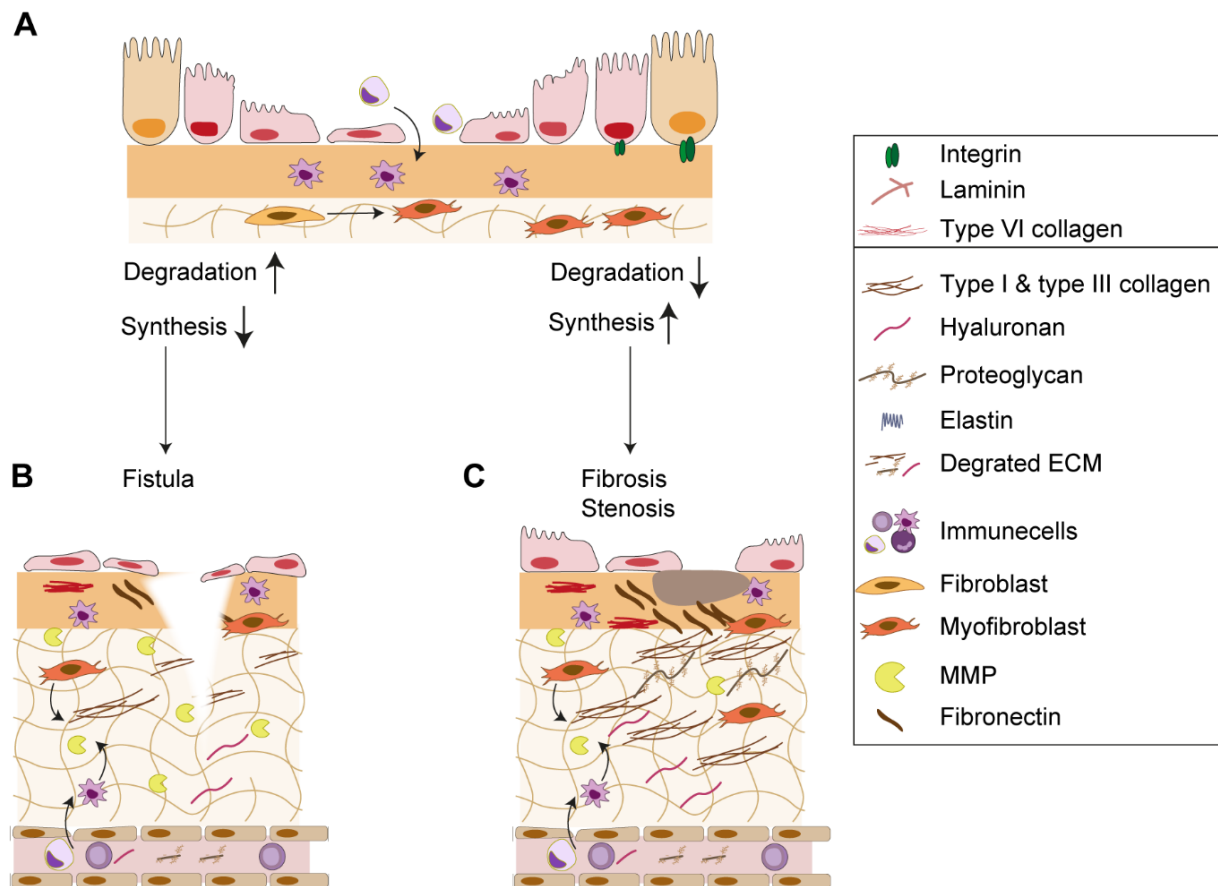
Figure 1-5: Extracellular matrix in disease. **(A)** Rupture of the epithelial cell layer and infiltration of immune cells leads to production of cytokines that induce differentiation of fibroblasts to myofibroblasts and increased numbers of macrophages. This can either induce higher synthesis of degrading enzymes such as MMPs and decreased synthesis of matrix components resulting in the formation of fistulas **(B)** or might lead to excessive synthesis of matrix components and reduced degradation resulting in fibrosis/stenosis **(C)**. Figure adapted from Frantz, Stewart and Weaver 2010.

1.4.1 Fibrous proteins

Fibrous proteins in the ECM are predominantly represented by collagen, elastin, laminins and integrins. With over 30%, the main structural element is collagen providing the ECM with support, stability and elasticity (Frantz et al. 2010). With 28 different collagen types, collagen type I, II and III make up 80-90% of collagen within the body (Karamanos et al. 2021, Sorushanova et al. 2019), whereas collagen type VI is the main component of the basement

membrane (Halfter et al. 2015). Fibroblasts produce collagen fibrils, can further be responsible for excessive formation of collagen type I and III and can give rise to myofibroblasts (Mortensen et al. 2019). Excessive amounts of collagen and alteration in collagen network of ECM can lead to fibrotic diseases (Ricard-Blum, Baffet and Theret 2018, Mak, Png and Lee 2016). Scheibe *et al.* showed higher levels of collagens in mucosal and submucosal tissues of patients with CD and UC (Scheibe et al. 2019). Serological analysis of fragments from type IV collagen in CD and UC patients found a significant increase in CD patients, however not in the serum of UC patients (Lindholm et al. 2021). Collagen fibrils are usually cross-linked with tropoelastin by lysyl oxidase (LOX) and LOX-like (LOXL) proteins (Karamanos et al. 2021).

Elastin provides elasticity to the ECM, especially in tissue that is exposed to high mechanical stress, for example the lung and arteries (Wang, Song and Resnick 2020). Laminins are the most prominent components of the basal membrane (BM) in the extracellular space. In the intestine, the BM is tightly associated with epithelial cells and of importance for cell polarity and integrity of the epithelial cell layer (Spenle et al. 2012, Miner 2008). Dysregulated expression of laminin was found to be associated with CD by Bouatrouss *et al.* who examined small intestinal specimens of CD patients and control tissue and reported upregulation of laminin alpha1 and laminin alpha 3 in crypts of CD patients (Bouatrouss et al. 2000).

An additional fibrous protein found in the ECM is integrin, which links the ECM to the cell cytoskeleton. Further, integrins are responsible for cell-cell interactions (Oxford, Reeck and Hardy 2019). CD patients show a significantly increased expression of integrin subtype αvβ6 and murine *in vivo* experiments validated contribution of integrin αvβ6 to intestinal fibrosis (Koivisto et al. 2018, Xie et al. 2022, Chen et al. 2021).

1.4.2 *Proteoglycans and glycosaminoglycans*

Proteoglycans in the ECM have a structural function and can additionally influence cell behavior and signaling via acting as co-receptors (Karamanos et al. 2021). They consist out of a protein core that is covalently bound to negatively charged glycosaminogylcans (GAGs). The protein cores can either be cell-membrane bound or soluble. Proteoglycans can be classified into families according to location, structure, and function. Here, proteoglycans will be introduced by separating them into groups based on their location: extracellular, cell surface, basement membrane and intracellular (Iozzo and Schaefer 2015). The only intracellular proteoglycan described so far is serglycin. Serglycin is found in endothelial cells and is substituted with heparin and chondroitin sulfate side chains (Iozzo and Schaefer 2015, Kolset and Tveit 2008). Cell surface proteoglycans can be either transmembrane type I proteoglycans which are syndecans, chondroitin sulfate proteoglycan 4 (CSPG4), betaglycan and phosphacan. Their protein cores are linked to chondroitin sulfate and heparan sulfate side chains (Iozzo and Schaefer 2015). Syndecan-1 (Sdc1) is highly concentrated in the intestinal

epithelium of mice and human. In the case of Sdc1 knockout in an experimental mouse model of colitis, animals show higher mortality rates indicating a protective effect of Sdc1 (Floer et al. 2010). Further, for UC and CD patients Sdc1 serum levels were reported to be significantly increased when compared to inactive UC or healthy controls. Additionally, Sdc1 correlated significantly with severity of UC (Floer et al. 2021, Yablecovitch et al. 2015). The other group of membrane-bound proteoglycans are glypicans/GPI-anchored proteoglycans. The pericellular glycoproteins are mostly located in basement membranes and associated with cells via integrins or other receptors (Iozzo and Schaefer 2015). Pericellular proteoglycans are perlecan and arginine, which are dominantly associated with heparin sulfate chains.

The largest group of proteoglycans are found in the extracellular space that can be divided into hyaluronan– and lectin-binding proteoglycans (hyalectans) and small leucine-rich proteoglycan (SLRPs). Hyalectans comprise aggrecan, versican, neurocan and brevican and share the feature of a tridomain structure. The tridomain structure is characterized by hyaluronan binding to the N-terminal domain, a central domain containing GAG side chains and C-terminus binding lectins (Iozzo 1998, Iozzo and Schaefer 2015). Heterogeneity of all the above-mentioned proteoglycans is largely provided by the GAGs attached to their protein core.

GAGs are built out of repeating disaccharide units, in which each building block contains an amino sugar and an uronic acid that can further be sulfated in different positions (Song, Zhang and Linhardt 2021, Afratis et al. 2012). Based on this, GAGs can be separated into the following families: Keratan sulfate, heparin/heparin sulfate, chondroitin/dermatan sulfate (CS/DS) and hyaluronan (HA). Except for HA, GAGs are bound to the core protein and synthesized in the Golgi apparatus or endoplasmic reticulum. However, HA is synthesized by HA synthases (HYAS1, HYAS2 and HYAS3) that are located on cell surfaces and after synthesis is released into the extracellular space without binding to other proteins (Kobayashi, Chanmee and Itano 2020). The HA receptor CD44 is a cell adhesion molecule expressed by various immune cells and endothelial cells with its main function to bind and internalize HA especially in an inflammatory environment (Litwiniuk et al. 2016, Johnson and Ruffell 2009). Degradation of HA is catalyzed by hyaluronidases (HAYLs). An elevated production of HA is associated with several inflammatory disorders including IBD. In IBD, elevated levels of HA are reported when comparing inflamed colon tissue to non-inflamed control tissue (de La Motte et al. 1999, Petrey and de la Motte 2019). Reducing synthesis of HA in murine models of intestinal inflammation by knockout of *Has3* successfully attenuates disease progression (Kessler, Obery and de la Motte 2015). Further, the elevated production of HA in intestinal small vessels of DSS-induced colitis mice supports immune cell infiltration via the HA-CD44 interaction and supports inflammatory processes (Kessler et al. 2008).

1.4.3 ECM-associated proteins and enzymes

ECM is a highly dynamic structure and is subjected to degradation and synthesis of its components. This needs to be orchestrated in a delicate manner. Fibroblasts are not only sources for ECM components like collagen and elastin but further control structural integrity by providing MMPs for ECM degradation (Lynch and Watt 2018, Parsonage et al. 2005, Kalluri and Zeisberg 2006). In total, the human genome encodes for 23 MMPs that are discriminated by substrate, for example collagenases (MMP-1, MMP-8) and gelatinase B (MMP9) (Karamanos et al. 2021, O'Shea and Smith 2014). MMPs are regulated at transcriptional and translational levels and by tissue inhibitors of MMPs (TIMPs) (Hu et al. 2007). Like in IBD pathology, intestinal damage or inflammation can induce excessive degradation of ECM by MMPs in order to support immune cell infiltration, which in turn might increase inflammatory responses due to release of cytokines. MMPs have been reported as driving factors of IBD pathogenesis (Derkacz et al. 2021b). Kirkegaard *et al.* observed strong MMP-3 expression in mononuclear cells and fibroblasts in fistulae of CD patients independent of inflammatory activity. Further, MMP-9 expression was observed in acute inflammation in CD patients, while TIMP-1, -2 and -3 was low in fistulas of CD patients. (Kirkegaard et al. 2004). Additionally, Lakatos *et al.* observed significantly higher MMP-9 expression in UC patient's biopsies with immunohistochemistry and gene expression assay (Lakatos et al. 2012). Apart from that, increased levels of TIMP-1 were shown in fibrosis of CD patients and murine experiments (von Lampe et al. 2000, Lawrance et al. 2017). TIMP-1 synthesis by CCR2^{+} fibrocytes promotes fibrosis in colons of a murine model of chronic colitis (Kuroda et al. 2019). Therefore, TIMP-1 producing cells might be crucial for intestinal fibrosis in IBD (McKaig et al. 2003).

2 AIM OF THE STUDY

Contrast enhanced magnetic resonance imaging (MRI) is an important non-invasive tool in diagnosing various diseases. In inflammatory bowel diseases (IBD) patients exhibiting inflammation in the small intestine, routinely undergo MRI examinations. Gadolinium-based contrast agents are used for this examination in order to enhance inflammatory regions in the MR images. Since safety of gadolinium-based contrast agents was recently questioned, research is anticipated at finding a safe alternative. This study aimed to investigate an iron-oxide based contrast agent, called very small superparamagnetic iron oxide particles (VSOPs), for its efficacy as an alternative in MRI-based examinations of intestinal inflammation.

First, VSOPs were used in MRI examinations of mouse models exhibiting intestinal inflammation. The three mouse models used in this study were dextran sulfate sodium (DSS) induced colitis, transfer colitis and a $TNF^{\Delta ARE}$ model. Within all models different time points were chosen for MRI examinations in order to investigate different disease severities. This was done in order to evaluate sensitivity of VSOP-enhanced MRI during early-onset tissue inflammation and severe tissue inflammation. Mice underwent MRI examinations before VSOP application and 90 minutes after intravenous VSOP injection. The resulting MR images were evaluated visually for VSOP-induced contrast decrease in the inflamed intestine. If visual validation was successful, the contrast–to–noise ratio was calculated for the intestinal wall.

Second, to build on previous studies showing the involvement of the extracellular matrix components in binding of VSOPs, the colon tissue of mice was investigated for hyaluronic acid content and chondroitin sulfate proteoglycan 4 using immunohistochemistry. Moreover, imaging mass cytometry was used to examine localization of VSOPs in the colon tissue of DSS-induced colitis and transfer colitis mice.

Third, to unravel biocompatibility of VSOPs, *in vivo* and *in vitro* set-ups were implemented. Transfer colitis mice received a single dose of VSOPs and isolated mononuclear lymphocytes of mesenteric lymph nodes were evaluated by mass cytometry at different time points post VSOP injection. Furthermore, human primary monocytes were treated with VSOPs *in vitro* and RNA sequencing, flow cytometry and cytometry bead array was used to inspect gene expression changes, phenotypic differences and cytokine expression upon VSOP exposure.

3   MATERIAL AND METHODS

3.1   Materials

3.1.1   Instruments

Table 3-1: Instruments used for this study.

Instrument	Company
1H-RF quadrature volume coil	RAPID Biomedical, Würzburg, Germany
7 T MRI scanner	BioSpec, Bruker, Ettlingen, Germany
Agarose gel electrophoresis chamber	Peqlab, Erlangen, Germany
AxioImager Z1	Zeiss Microscopy GmbH, Jena, Germany
Centrifuge 5810 R	Eppendorf, Hamburg, Germany
CO_2 cell culture incubators	Thermofisher Scientific, Waltham, MA, USA
Cooling plate CP-4D	Kunz Instruments, Stockholm, Sweden
FACS Canto II	BD, Franklin Lakes, NY, USA
FACSJazz™	BD Biosciences, Franklin Lakes, NY, USA
Helios™	Fluidigm, San Francisco CA, USA
Heraeus UT 6060 drying oven	Thermofisher Scientific
HERAsafe Biological Safety Cabinet	Thermofisher Scientific
HLC Heating Thermomixer	Ditabis, Phorzheim, Germany
Infinite® F50 plate reader	Tecan Group, Männedorf, Switzerland
LOGOS one automated tissue processor and embedder	Milestone medical, Sorisole, Italy
MPS/W paraffin embedding station	SLEE medical GmbH, Olm, Germany
MSM Automated tissue stainer	SLEE medical GmbH
Primovert light microscope	Zeiss, Oberkochen, Germany
Rotary microtome HM 325	Thermofisher Scientific
Small animal respiration monitor	Small Animal Instruments Inc., Stony Brook, NY, USA
T 3000 Thermocycler	Biometra, Göttingen, Germany
Trans Therm Pressure cooker	WMF, Geislingen, Germany
Trans-illuminator	Peqlab, Erlangen, Germany
Vectra3 microscopy system	Akoya Biosciences, Marlborough, MA, USA
Waterbath 100	Pfm medical AG, Cologne, Germany

3.1.2 Buffers

Phenanthrolinhydrochlorid-solution

- 4 mM 1,10- Phenanthrolinhydrochlorid-1-H_2O (Carl Roth, Karlsruhe, Germany)
- 200 mM Acedic acid > 98% (Carl Roth)
- 160 mM sodium acetate (Carl Roth)
- In Millipore water

Magnetic-activated cell sorting (MACS) buffer

- 5 g bovine serum albumin (BSA, Fraction V, Sigma-Aldrich, Saint Louis, USA)
- 500 mL phosphate buffered saline 1x (PBS, Gibco, Darmstadt, Germany)

Complete Media

- Rosewell Park Memorial Institute (RPMI) Medium 1640 (Gibco)
- 100 mg/L penicillin-streptomycin
- 10% Fetal Bovine Serum (FBS)

Culture Media

- RPMI Medium 1640 (Gibco)
- 100 mg/L penicillin-streptomycin
- 10% FBS
- 10 µg/mL granulocyte-macrophages colony-stimulating factor (GM-CSF)

Very small superparamagnetic particles (VSOPs) treatment media

- RPMI Medium 1640 (Gibco)
- 100 mg/L penicillin-streptomycin
- 1% FBS
- 10 µg/mL GM-CSF

Erythrocyte lysis buffer

- 8.9 g NH_4Cl (Merck, Darmstadt, Germany)
- 1 g $KHCO_3$ (Merck)
- 0.038 g ethylenediaminetetraacetic acid (EDTA, Sigma Aldrich)
- 1 L distilled water

Antigen retrieval buffer

- 10 mM Citric acid monohydrate (Carl Roth, Karlsruhe, Germany)

- Adjust to pH=6 with 2M sodium hydroxide

3.1.3 Antibodies

Table 3-2: Antibodies for histology.

Antigen	Clone	Source
CSPG4	Polyclonal rabbit	Sigma-Aldrich
HA	Biotinylated binding protein	Millipore Sigma, Burlington, MA, USA
CD44	E7K2Y	Cell Signaling Technologies, Danvers, MA, USA
F4/80	D2S9R	Cell Signaling Technologies

Table 3-3: Antibodies for CyTOF staining of VSOP-stimulated human whole blood.

Antigen	Clone	Isotope	Source
CD45	HI30	141Pr	Fluidigm
CD19	HIB19	142Nd	Fluidigm
CD16	3G8	148Nd	Fluidigm
CD3	UCHT1	154Sm	Fluidigm
CD33	WM53	163Dy	Fluidigm
CD14	M5E2	175Lu	Fluidigm
Cell-ID Intercalator		191Ir	Fluidigm
Cell-ID Intercalator		193Ir	Fluidigm

Table 3-4: Antibodies for imaging mass cytometry (IMC).

Antigen	Clone	Isotope	Source
CD45	MRC OX-1	169Tm	Abcam
CD3ε	D4V8L	170Er	Fluidigm
CD4	D7D2Z	156Gd	CST
CD8α	4SM15	173Yb	ThermoFisher Scientific
CD44	E7K2Y	148Nd	CST
B220	RA3-6B2	166Er	ThermoFisher Scientific
CD138	281-2	168Er	BioLegend
F4/80	EPR22059-270	145Nd	Abcam

CD68	polyclonal	163Dy	Abcam
Ly6G	1A8	150Nd	BioLegend
CD11b	EPR1344	149Sm	Fluidigm
CD11c	polyclonal	154Sm	Fluidigm
CD56	E7X9M	146Nd	CST
Vimentin	EPR3776	172Yb	Abcam
αSMA	polyclonal	174Yb	Abcam
E-Cadherin	4A2	158Gd	Abcam
EpCAM	E6V8Y	143Nd	CST
beta-catenin	6B3	167Er	CST
CD103	BP6	175Lu	Abcam
CD31	D8V9E	164Dy	CST
Ki67	16A8	147Sm	BioLegend
clCasp3	Asp175	176Yb	CST
Cell-ID Intercalator		191Ir	Fluidigm
Cell-ID Intercalator		193Ir	Fluidigm

Table 3-5: <u>Antibodies for CyTOF staining of murine mesenteric lymph nodes</u>

Antigen	Clone	Isotope	Source
CD45	30-F11	89Y	Fluidigm
Ly6G	1A8	141Pr	Fluidigm
CD11c	N418	142Nd	Biolegend
B2M	A16041A	143Nd	Biolegend
B220	RA3-6B2	144Nd	Biolegend
CD25	3C7	145Nd	Biolegend
CD163	S15049I	146Nd	Biolegend
B2M	A16041A	147Sm	Biolegend
CD44	IM7	148Nd	Biolegend
CCR2	QA18A56	149Sm	Biolegend
CD24	M1/69	150Nd	Biolegend
CD3	145-2C11	152Sm	Fluidigm
CD11b	M1/70	154Sm	Biolegend
CD95	SA367H8	155Gd	Biolegend
CD64	X54-5/7.1	156Gd	Biolegend
Foxp3	FJK-16s	158Gd	Fluidigm

RORγt	B2D	159Tb	Fluidigm
CD62L	MEL-14	160Gd	Biolegend
B2M	A16041A	161Dy	Biolegend
Ki67	11F6	162Dy	Biolegend
CD8a	53-6.7	163Dy	Biolegend
CXCR1	SA011F11	164Dy	Fluidigm
I-A/I-E	M5/114.15.2	165Ho	Biolegend
NKp46	29A1.4	167Er	Fluidigm
B2M	A16041A	168Er	Biolegend
Sca-1	D7	169Tm	Biolegend
CD103	2E7	170Er	Biolegend
CD80	16-10A1	171Yb	Biolegend
B2M	A16041A	172Yb	Biolegend
CD127	A7R34	173Yb	Biolegend
Ly6C	RB6-8C5	174Yb	Biolegend
CD38	90	175Lu	Biolegend
LFA-1	H155-78	176Yb	Biolegend
Cell-ID Intercalator		191Ir	Fluidigm
Cell-ID Intercalator		193Ir	Fluidigm

Table 3-6: Antibodies for flow cytometry

Antigen	Clone	Flurochrome	Source
CD14	HCD14	PE/Cyanine7	Biolegend
CD16	3G8	PE	Biolegend
CD163	GHI/61	Alexa Fluor 674	Biolegend
HLA-DR	LN3	PerCP/Cyanine5.5	eBioscience
CD80	2D10.4	FITC	eBioscience
CD86	IT2.2	Brilliant Violet 421	Biolegend
CD71	CY1G4	FITC	Biolegend
CCR2	K036C2	APC	Biolegend
CD206	19.2	eFluor 450	eBioscience

3.1.4 Primer

Table 3-7: <u>Genotyping primer for *TNF^{ΔARE}* mice</u>

Primer name	Primer sequence (5'-3')
Forward	GAG CCA GCC CCC CTC GGA AGG CCG GGG TG
Reverse	AAT TAG GGT TAG GCT CCT GTT TCC

3.2   Mouse strains

Wild-type (WT) inbred C57/Bl6J mice were purchased from Charles River (Sulzburg, Germany). Recombinant activating gene 1-deficient mice (*Rag^{1tm1Mom}*) in a C57/Bl6J background were obtained from Jackson Laboratory (Bar Harbor, USA) and bred under specific pathogen free (SPF) conditions. *TNF^{ΔARE}* mice were obtained from Fabio Cominelli form the department of medicine-gastroenterology, University Hospitals Cleveland Medical Center (Pizarro, Arseneau and Cominelli 2000) and bread under SPF conditions. All mice were housed at the animal facility of the Research Institute for Experimental Medicine (FEM, Charité – Universitätsmedizin Berlin, Germany), kept in polycarbonate cages and had free access to sterile standard chow and drinking water. Animal experiments described within this thesis were performed in accordance with the German legislation on the protection of animals and approved by the local authorities (Landesamt für Gesundheit und Soziales). All the stated experiments are registered under the following registration numbers: G0422/17 and G0117/20.

3.3   Mouse models for intestinal inflammation

In this study, two models exhibiting colitis and one model exhibiting ileitis were used. Animal study design is summarized in **Figure 3-1**. Mouse models of intestinal inflammation were examined by very small superparamagnetic iron oxide nanoparticles (VSOPs) enhanced magnetic resonance imaging (MRI). For this, VSOPs doped with europium were obtained from the Department of experimental Radiology at the Charité – Universitätsmedizin Berlin, which were synthesized as stated in de Schellenberger *et al.* 2017. Further, the influence of VSOPs on the intestinal immune system was evaluated in one mouse model for colitis. For this, VSOPs without europium were used, also obtained from the Department of experimental Radiology at the Charité – Universitätsmedizin Berlin (de Schellenberger et al. 2017).

3.3.1 Dextran sulfate sodium–induced colitis

In this mouse model, colitis was induced in >10 weeks of age female WT inbred C57/Bl6J mice by supplementation of 3% dextran sodium sulfate (DSS; MW 36,000-50,000, MP Biomedicals,

Santa Ana, CA, USA) in the drinking water. For acute colitis, animals were exposed to DSS via the drinking water for six days followed by pure drinking water for an additional 4 days. Mice were sacrificed and analyzed at four different time points in the course of DSS treatment: day 2, 4, 6 and 10. Controls received pure drinking water throughout the whole experiment. Weight was monitored regularly, animals were checked for clinical symptoms, stool samples were scored, monitored and animals were electively sacrificed when meeting humane endpoints.

3.3.2 Transfer colitis

Colitis was induced in 8 week-old female and male $Rag^{1tm1Mom}$ mice by intraperitoneal (i.p.) injection of 4 x 10^5 CD4$^+$CD45RB^{hi} T cells isolated from spleens of WT inbred C57/Bl6J mice. Isolation of CD4$^+$CD45RB^{hi} T cells was done according to Maschmeyer et al. (Maschmeyer, Zimmermann and Kuhl 2021). Shortly, splenocytes were isolated and CD4$^+$ T cells were enriched by using CD4-APC MultiSort Kit (Miltenyi Biotec, Bergisch Gladbach, Germany). Afterwards, the CD4$^+$ T cells were stained with CD45RB-PE antibody (Miltenyi) and approximately 40% of the cell population highly expressing CD45RB (CD45RB^{hi}) was sorted with FACSJazz^{TM} (BD Biosciences, Franklin Lakes, NY, USA). Depending on the experimental purpose, animals were sacrificed and analyzed at different time points. For magnetic resonance imaging (MRI), mice were sacrificed on day 14, 21, 28 or 40 after T-cell transfer. For studying the long-term influence of VSOPs on intestinal immune system, animals were intravenously (i.v.) injected with VSOPs 14 days after T-cell transfer. Mice were sacrificed either 7, 10 or 18 days after VSOP injection. Weight was monitored regularly, animals were checked for clinical symptoms, stool samples were scored, monitored and animals were electively sacrificed when meeting humane endpoints.

3.3.3 Ileitis in TNF$^{\Delta ARE}$ mice

$TNF^{\Delta ARE}$ mice harbor a mutation in the adenosine-uracil rich elements (ARE) untranslated region located at the 3'-region in transcripts encoding for cytokines. This in turn stabilizes tumor necrosis factor (TNF) expression and induces spontaneous development of inflammation in the terminal ileum of these animals. In addition, these mice suffer from uveitis, arthritis, and dermatitis. Heterozygous $TNF^{\Delta ARE/+}$ female and male mice were used in this study. For MRI experiments, mice were analyzed and sacrificed either at 10, 12 or 14 weeks of age. Weight was monitored regularly, animals were checked for clinical symptoms, stool samples were scored, monitored and animals were electively sacrificed when meeting humane endpoints.
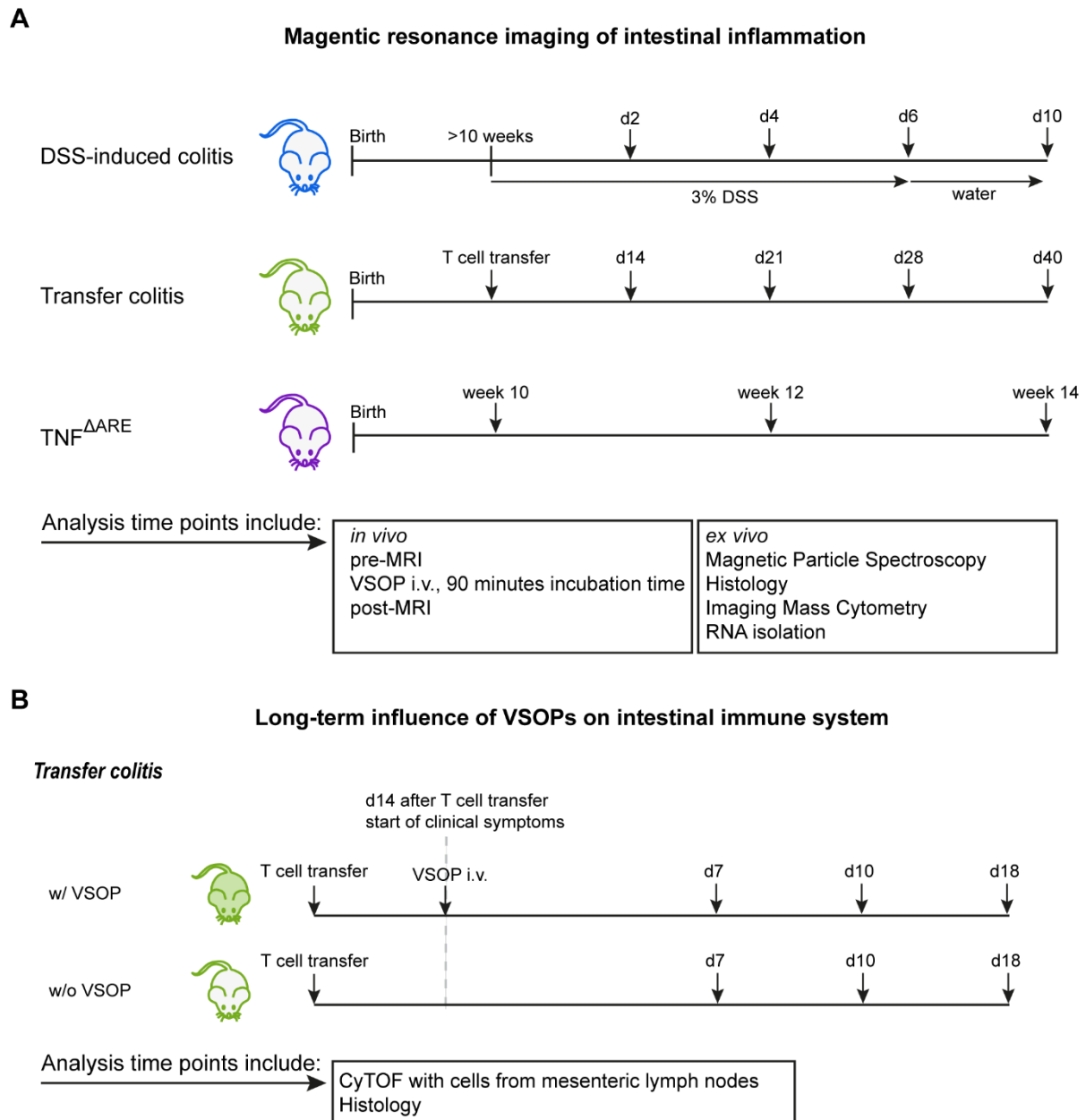
Figure 3-1: Experimental design of mouse experiments for magnetic resonance imaging (MRI) of intestinal inflammation **(A)** and long-term influence of VSOPs on intestinal immune system **(B)**. For MRI of intestinal inflammation, the DSS-induced colitis model, transfer colitis model and *TNF^{ΔARE}* mouse model were applied. For each model specific time points were evaluated as indicated. For DSS-induced colitis, mice underwent MRI at days 2, 4, 6 and 10 (d2, d4, 6 and d10) after DSS treatment, d10 refers to 6 days of DSS treatment with additional 4 days of drinking water. Control animals received drinking water throughout the whole experiment. In transfer colitis mice MRI was performed at day 14, 21, 28 and 40 (d14, d21, d28 and d40) after colitis induction and control animals were injected with PBS. *TNF^{ΔARE}* mice were analyzed at week 10, 12 and 14 after birth. For control, WT littermates were used. All animals underwent MRI before VSOP application and 90 minutes after intravenous VSOP injection. After *in vivo* MRI, animals were sacrificed, and tissue samples were taken for different *ex vivo* analysis **(A)**. Long-term influence of VSOPs on the intestinal immune system was investigated in the transfer colitis model. In this model, VSOPs were injected 14 days (d14) after colitis induction (w/ VSOP). As

controls served transfer colitis animals not injected with VSOPs (w/o VSOP). Animals were sacrificed 7, 10 and 18 days after VSOP injection. Cells from mesenteric lymph nodes (mLN) were isolated and analyzed with mass cytometry by time-of-flight (CyTOF). Further, tissue samples were taken for histopathological analysis. VSOPs used for long-term exposure experiments were not doped with europium **(B)**.

3.4 Genotyping

Genotyping of mouse ear biopsies was done according to the user manual of Nucleo Type Mouse PCR (MARCHEREY-NAGEL, Düren, Germany). Shortly, ear biopsies were lysed in Lysis Reagent M (MARCHEREY-NAGEL) containing proteinase K (MARCHEREY-NAGEL). Samples were incubated for 10 minutes at room temperature while shaking at 300 rpm, followed by heat inactivation at 96°C for 3 minutes. Samples were directly used for polymerase chain reaction (PCR). For this, the HotStart PCR Master Mix (MARCHEREY-NAGEL) was used. Primers were purchased from TibMolBiol and are listed in **Table 3-7**.

3.5 Magnetic resonance imaging

MRI was performed in a preclinical 7 Tesla MRI scanner (BioSpec, Bruker, Ettlingen, Germany) running with Paravision 6.0.1 software as described in Golusda *et al.* 2022. Shortly, all scans were acquired with a 35 mm diameter 1H-RF quadrature volume coil (RAPID Biomedical, Würzburg, Germany). The protocol consisted of a T2*-weighted (T2*w) 2D FLASH scan with field of view of 33x33 mm^2, 60 contiguous 0.75 mm thick axial slices, matrix dimension of 120x148 zerofilled to 220x220, effective echo time of 3 ms (achieved using 1.49 partial fourier acceleration), echo train length of 8, echo spacing of 8 ms, repetition time of 605ms, readout bandwidth equaled 44643 Hz and a total acquisition time of 2:59 min.

All MRI protocols worked with fat suppression and flipback.

VSOPs were used as a contrast agent. VSOPs were provided by the Department of experimental Radiology at the Charité – Universitätsmedizin Berlin, Germany. The contrast agent was synthesized as described in the paper of de Schellenberger *et al.* 2017. Anesthesia in mice was induced with 2% isoflurane in a mixture of 70% oxygen and 30% nitrous oxide. Mice were then placed in and fixed to an animal holder, which included a warming pad that was set to a temperature of 50°C. Respiration was continuously monitored (Small Animal Instruments Inc., Stony Brook, NY, USA). MRI sequences were acquired as stated above. After first acquisition (pre-MRI) mice were injected i.v. with 0.03 mmol europium doped VSOPs per kg of bodyweight via the tail vein. 90 minutes post VSOPs injection a second set of MRI scans was acquired (post-MRI).

3.6 Analysis of colon and ileum MRI

Analysis T2*w axial colon MRI images was done with ImageJ (Java version 1.6.0_20). Six contiguous axial MR images were evaluated by calculation of the contrast to noise ratio (CNR) (**Figure 3-2**). CNR was calculated as followed: A region of interest (ROI) was drawn around the whole colon wall of a respective image slice. When the respective slice showed colon lumen, an outer and an inner circle was fitted around the wall. In case the colon area did not show any identifiable lumen, only one circle was drawn around the colon wall. Further, a ROI was set in the area of the muscle, which was chosen as a reference tissue. Additionally, the background signal was measured by drawing a rectangular ROI outside of the body (**Figure 3-2, C**). First, the signal to noise ratio (SNR) was calculated for colon wall and muscle, by dividing the signal of the respective tissue by the standard deviation (SD) of the background signal: $SNR = Signal_{Tissue\ of\ interest} / SD_{Noise}$. Then CNR was calculated by subtracting SNR of the colon (SNR_{Colon}) from the SNR of the muscle (SNR_{Muscle}): $CNR = SNR_{Colon} - SNR_{Muscle}$. This was done for six sub-sequential slices of T2*w MRI.
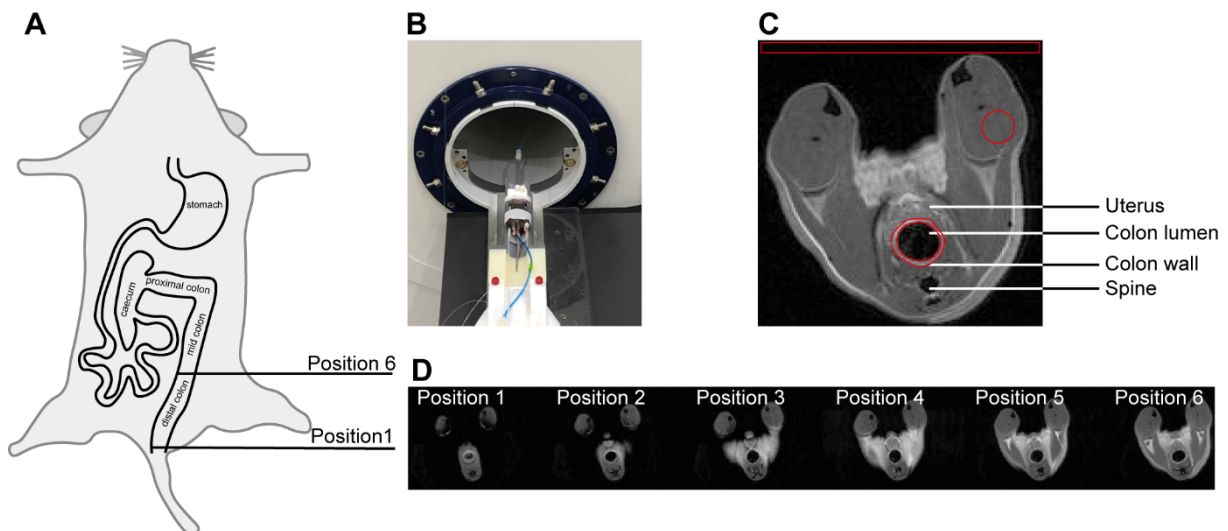
Figure 3-2: Positioning and orientation of animals for analysis of T2*w MR images from mouse colon. Graphical orientation of slice position in mouse body **(A)**, positioning of mouse in MRI scanner **(B)**, description of axial MR image of mouse with the regions of interest (ROI) highlighted in red that were used for contrast to noise ratio (CNR) calculation **(C)**. Representative six sub-sequential positions for further analysis **(D)**.

3.7 Iron quantification

3.7.1 Magnetic particle spectroscopy

Magnetic particle spectroscopy (MPS) was used to specifically quantify VSOPs in cells and tissues as described in Poller *et al.* 2016. Shortly, due to the specific non-linear response of

the VSOPs to the strong oscillating magnetic field, a specific MPS signal is generated. Intrinsic iron does not interfere with this measurement as it responds with a linear magnetization signal. The sample was placed in a PCR tube (Thermo Fisher Scientific, Waltham, Massachusetts, USA) and the tube was placed into the pick-up coil of the MPS. For measurement, the sample was exposed to a sinusoidally oscillating magnetic field (excitation amplitude of B_{ex}=25 mT, fixed frequency f_{ex} of 25 kHz) and the nonlinear magnetization response was detected (sensitivity: 5 pAm^2). The resulting amplitudes A_n of the MPS spectrum are proportional to the amount of iron and decrease monotonically with the harmonic number n. Therefore, the strongest amplitude A_3 was used for VSOP quantification in the sample.

3.7.2 1,10-phenanthroline spectrophotometry

The 1,10-phenanthroline method was used to determine iron concentration in cells. Monocytes were harvested from 12-well plate by scratching and transferred to a 1.5 mL Eppendorf tube. For cell lysis, the pellet was re-suspended in 20 μL of 35% hydrochloric acid. Afterwards, 1 mL Millipore water was added to dilute the hydrochloric acid. Cell debris was eliminated by centrifugation at 12.000 x g for 3 minutes. The supernatant was transferred to a fresh tube. Afterwards, 50 μL of sample was added to a flat bottom 96-well plate. To determine concentration, an iron standard solution (Merck, Darmstadt, Germany) was used with a concentration range between 0.3215 – 40 μg. As a blank measurement, 20 μL of 35% hydrochloric acid diluted in 1 mL of Millipore water were used. To each well 50 μL of 10% hydroxylaminhydrochlorid solution and 150 μL of phenanthrolinhydrochlorid solution were added. Samples were incubated for 15 minutes at room temperature in the dark. Absorbance of samples was measured at 492 nm with an Infinite$^®$ F50 plate reader (Tecan Group AG, Männedorf, Switzerland).

3.8 Histology

All tissues used for histopathological staining were removed from animals and directly fixed in 10% formalin (SAV Liquid Production GmbH, Flintsbach am Inn, Germany). After overnight incubation at room temperature, the fixed tissue was embedded in paraffin (Histosec, Merck Group, Darmstadt, Germany). Paraffin blocks were prepared and tissue sections with a thickness of 1-2 μm were cut from paraffin blocks and used for histochemistry, immunohistochemistry and immunofluorescence staining. Antibodies used for immunohistochemistry and immunofluorescence are listed in **Table 3-2**. Tissue sections for imaging mass cytometry were cut with a slice thickness of 4 μm.

For histomorphological evaluation (scoring) of tissue sections, the paraffin sections were transferred to a glass slide and dewaxed with 100% Xylol (Carl Roth, Karlsruhe, Germany). Then, sections were hydrated with decreasing concentrations of ethanol (Carl Roth). Tissue

sections were histochemically stained with hematoxylin (Merck Group, Munich, Germany) and eosin (Merck Group, H&E) and coverslipped with Histokitt (Carl Roth). Tissue sections were scored in a blinded manner according to Erben *et al.* 2014 and Zimmermann *et al.* 2016 by using an AxioImager Z1 microscope (Zeiss Microscopy GmbH).

For immunohistochemistry, the paraffin sections were dewaxed in 100% Xylol (Carl Roth) and hydrated in a descending concentrations of ethanol (Carl Roth. Afterwards, sections were subjected to heat-induced epitope retrieval and incubated with anti-CSPG4 at 4°C overnight. The EnVision+ System-HRP Labelled Polymer Anti-Rabbit (Agilent) was used for detection of anti-CSPG4. HRP was visualized with diaminobenzidine (Agilent) as chromogen. After inactivation of proteins and enzymes, sections were incubated with biotinylated HA binding protein (HABP2) for 30 minutes at room temperature followed by incubation with alkaline phosphatase-labelled streptavidin and RED as chromogen (Agilent). Nuclei were counterstained with hematoxylin (Merck) and slides coverslipped with glycerol gelatine (Merck Group). Controls were performed by omitting the primary antibodies. Using the Vectra3 microscopy system (Akoya Biosciences, Marlborough, MA, USA), multispectral images (5 high power fields (HPFs) per colon section) were acquired. HPFs were chosen manually in a blinded manner. The inform software (Version 2.4.7174.15475) allows for spectral unmixing of the images. Unmixed images showing CSPG4, HA, and nuclear staining were analyzed separately in ImageJ (Java version 1.6.0_20). For this, the plugin "IHC Toolbox" was used. The positively stained area was measured in an arbitrary unit and the mean of 5 HPFs was calculated per colon.

For immunofluorescence staining, paraffin sections were dewaxed in 100% Xylol (Carl Roth) and hydrated in a descending concentrations of ethanol (Carl Roth). Prior to blocking of endogenous peroxidase, heat-induced epitope retrieval was performed. Sections were then incubated with anti-CD44 for 30 minutes at room temperature at 1:800 dilution. For detection, the EnVision+ System-HRP Labelled Polymer Anti-Rabbit (Agilent) and Opal520 (Akoya Biosciences) was used. After inactivation of proteins and enzymes, sections were incubated with anti-F4/80 (1:3,000) for 30 minutes at room temperature. For detection, the EnVision+ System-HRP Labelled Polymer Anti-Rabbit (Agilent) and Opal670 (Akoya Biosciences) was used. Nuclei were stained with 4',6-Diamidino-2-Phenylindole (DAPI, 1:1,000) for 5 minutes at room temperature. Controls were performed by omitting the primary antibodies. Using the Vectra3 microscopy system (Akoya Biosciences), multispectral images (5 high power fields (HPFs) per colon section) were acquired. HPFs were chosen manually in a blinded manner. The inform software (Version 2.4.7174.15475) allows for spectral unmixing of the images and analysis of cell numbers.

3.9　High pressure liquid chromatography (HPLC)

HPLC measurement and analysis was done in cooperation with Véronique Blanchard and Katarina Biskup form Charité – Universitätsmedizin Berlin, Institute of Laboratory Medicine, Clinical Chemistry and Pathobiochemistry.

Shortly, colon tissue was proteolytically digested as stated in Volpi *et al.* 2014. Chondroitin sulfate (CS) and hyaluronic acid (HA) were cleaved into disaccharides and labeled with 2-animobenzamide. Samples were then analyzed with HPLC equipped with fluorescence detection as described in Biskup et al., 2021 (Biskup et al. 2021).

3.10　Imaging Mass Cytometry (IMC)

Imaging mass cytometry (IMC) experiments were established by and done in cooperation with Malte Lehmann from Charité – Universitätsmedizin Berlin, medical Clinic for Gastroenterology, Infectiology and Rheumatology. Paraffin tissue sections on a glass slide were dewaxed in 100% Xylol and hydrated in a descending alcohol series. Antigen retrieval was performed in citrate buffer at pH 6.0 followed by washing with Tris-buffered saline with Tween 20 (TBST). Blocking was achieved using 3% BSA (Serva, Heidelberg, Germany) diluted in antibody diluent (Agilent, Santa Clara, USA) for 45 minutes. Without washing, the tissue section was then incubated overnight with antibody mixture, diluted in antibody diluent (Agilent) containing 0.5 % BSA (Serva) at 4°C. After incubation, slides were washed with TBST and nuclei were stained with CELL-ID Intercalator-Ir (Fluidigm) with a dilution of 1:400 in antibody diluent (Agilent) for 30 minutes. Then, tissue sections were rinsed and air-dried. Slides were stored dust-free at room temperature until further use. Data acquisition was done in the Flow Cytometry Core Facility at the Charité – Universitätsmedizin Berlin. Briefly, a CyTOF2/upgraded to Helios specifications coupled to a Hyperion Tissue Imager (version 6.5.236) was used. Acquisition and analysis were performed according to Lehmann *et al.* 2021. In short, CellProfiler software (version 3.1.9) was used to prepare image for further analysis. Illastic software (version 1.3.3rc2) was implemented for pixel classification and probability maps. Probability maps were then loaded into cell CellProfiler to create single cells masks. Finally, the data was loaded into the HistoCAT software (version 1.7.1) and an arcsinh transformation (cofactor = 5) was applied. Using the same software, a dimensionality reduction tSNE algorithm was used followed by a Phenograph clustering algorithm, both times excluding the 151Eu and 153Eu channels.

3.11 Isolation of mesenteric lymph node cells

Mesenteric lymph nodes (mLN) were dissected from mice and put into ice cold PBS. The tissue was then smashed through a 100 μm cell strainer (Sigma-Aldrich) and washed twice with PBS. The suspension was centrifuged at 400 x g for 7 minutes at 4°C and the pellet resuspended in complete media and again filtered through a 100 μm gaze filter. The resulting cell suspension was centrifuged and cells were frozen according to the protocol for CyTOF staining.

3.12 Cell fixation and freezing for CyTOF staining

Isolated cells from mLN were resuspended in 700 μL complete RPMI media containing 50% FBS. The cell suspension was transferred to a cryo tube (Sarstedt, Nümbrecht, Germany) containing 500 μL Proteomic Stabilizer PROT1 (Smart Tube Inc. Las Vegas, NV, USA). After a 12 minute incubation at room temperature and then samples were stored at -80°C until further use.

3.13 Antibody labeling for CyTOF and imaging mass cytometry

Conjugation of antibodies to metal isotopes was done with Maxpar® X8 antibody labeling kit (Fluidigm) with slight adaptations to the user manual. 100 μg of antibody were labeled with metal isotope. For this, Maxpar Polymer was dissolved in L-Buffer provided within the kit. The respective metal isotope was added to the solution and incubated for 40 minutes at 37°C. After incubation, metal-loaded polymer was transferred to an Amicon® 3 kDa filter unit (Millipore Sigma, Burlington, MA, USA) and washed multiple times with L-Buffer and once with C-Buffer. In parallel, antibody was retrieved by loading it onto Amicon® 50 kDa filter unit (Millipore Sigma) and washed with provided L-Buffer. After washing, Tris (2-carboxyethyl) phosphine hydrochloride (TCEP, Millipore Sigma) was added and incubated for 30 minutes at 37°C. The filter unit was washed two times with C-Buffer afterwards. For conjugation, metal-loaded polymer was transferred to 50 kDa filter unit containing purified antibody and mixture was incubated for 2 hours at 37°C. The filter unit was washed multiple times with provided W-Buffer and conjugated antibody was transferred from the filter unit to an Eppendorf tube (Eppendorf, Hamburg, Germany). The concentration was measured using a NanoDrop™ spectrophotometer and diluted with Antibody Stabilizer PBS (Candor Bioscience, Wangen, Germany). Antibodies were stored at 4°C for further use.

3.14 CyTOF with VSOP treated whole blood

Fresh whole blood (5 mL) was taken from healthy human donor in heparinized tubes. The sample was streated with 0.75 mM VSOPs for 30 minutes under gentle rotation. For fixation,

the sample was mixed with Proteomic Stabilizer PROT1 (Smart Tube Inc. Las Vegas, NV, USA) in a 1:2.5 ratio, incubated for 12 minutes at room temperature and stored at -80°C for further use. After thawing, the sample was incubated in Smart Tube Buffer two times for 10 minutes to lyse erythrocytes. Then, the sample was stained according to **Table 3-3** and measured in Flow Cytometry Core Facility with a Hyperion Tissue Imager (Fluidigm) coupled to a Helios with the CyTOF software (version 6.5.236). Flow cytometry standard (FCS) files were analyzed using FlowJo. Software (Version 10.1)

3.15 CyTOF of mouse mesenteric lymph nodes

Cells isolated from mLN were stained for CyTOF measurement. For each CyTOF run an anchor sample was added, containing cells from mLN and lamina propria mononuclear cells of wild type mice. The anchor sample in each run originated form the same pool of cells. Cells were transferred from -80°C to dry ice and then gently thawed at 10-15°C. When thawed, cells were treated with benzonase (1:10,000, 25KU Universal Nuclease, Thermo Fisher Scientific) at 37°C for 5 minutes. Afterwards, each sample was barcoded with a specific metal-labeled B2M antibody combination. After barcoding of individual samples, up to 9 samples were pooled together, additional to an anchor sample, followed by surface staining of pooled cells for 30 minutes at 4°C in Maxpar Cell Staining Buffer (Fluidigm) using antibodies listed in **Table 3-5**. For intranuclear staining, cells were permeabilized (Foxp3/Transcription Factor Fixation/Permeabilization Kit, eBioscience^{TM}) for 60 minutes at room temperature. The permeabilized sample was then stained for transcription factors (**Table 3-5**) in Foxp3-Perm Buffer (eBioscience^{TM}) for 30 minutes at room temperature. Next, the sample was fixed in 4% PFA (Thermo Fisher Scientific) at 4°C overnight. On the next day, the sample was treated with CELL-ID Intercalator-Ir (Fluidigm) for 25 minutes at room temperature. Afterwards, the sample was washed twice with Maxpar Cell Staining Buffer (Fluidigm) and once with MaxPar water (Fluidigm) right before acquisition. Measurement was done at the Flow Cytometry Core Facility at the Charité with a CyTOF2/Helios (Fluidigm) mass cytometer with the CyTOF software (version 6.5.236). For measurement, EQ four element calibration beads (Fluidigm) were added during sample acquirement to check signal changes during time of measurement.

3.16 CyTOF data analysis

For each run, the FCS files were first uploaded into Cytobank (www.cytobank.com). Here, files were manually gated on living, single cells (**Supplementary Figure 2, A-C**) and samples were de-barcoded according to their barcoding scheme. Then, de-barcoded FCS files were exported and normalized with the *CytofBatchAdjust* function in R software (version 4.0.5). Normalized FCS files were uploaded into Cytobank for pre-gating on CD45$^+$ cells (**Supplementary Figure**

2, D). Pre-gated FCS files were uploaded into R environment and *CATALYST* package (version 1.14.1) was used for *FlowSOME/ConcensusClusterPlus* and cluster identification, UMAP generation (Nowicka et al. 2017). The statistical significance of differential abundant clusters in different groups was evaluated with generalized linear mixed-effects model by using the *diffcyt* (version 1.10.0) package in R software.

3.17 Peripheral blood mononuclear cell isolation from whole blood

Human peripheral blood mononuclear cells (PBMCs) were isolated from female and male healthy donors. Blood was collected in Vacuette® K3 EDTA coated tubes (Greiner Bio-One, Kremsmünster, Austria). PBMCs were isolated with SepMate technique (Stemcell, Vancouver Canada). Shortly, blood was diluted in PBS (Gibco, Waltham, Massachusetts, USA) with 2% FBS and transferred to a SepMate tube containing LymphoPrep (Stemcell). After centrifugation, the cell suspension was washed twice with PBS (Gibco) with 2% FBS.

3.18 Peripheral blood mononuclear cell isolation from buffy coats

Peripheral blood mononuclear cells (PBMCs) were isolated from buffy coats of healthy donors with unknown sex. Buffy coat was diluted 1:3 with PBS (Gibco). 25 mL of diluted buffy coat was slowly layered on 15 mL LymphoPrep (Stemcell). The resulting gradient was centrifuged at 12,000 x g for 25 minutes with an acceleration of 1 and break of 0. The resulting PBMC layer was taken off using a Pasteur pipette and transferred to a fresh 50 mL falcon (Thermo Fisher Scientific). Depending on experiment and further steps, the cells were washed in complete media or MACS buffer and centrifuged at 400 x g for 7 minutes. This wash step was repeated once before cells were counted in a Neubauer counting chamber to estimate cell count.

3.19 CD14 monocyte enrichment

CD14$^+$ monocytes were enriched using the MACS® cell separation technique from Miltenyi with the human CD14 MicroBeads (Miltenyi Biotec). CD14$^+$ monocytes were enriched from freshly isolated PBMCs. Per 10^7 PBMCs 80 µL of MACS buffer were used to dilute cells. Diluted cells were attached to CD14 MicroBeads with 20 µL of beads per 10^7 cells. Mixture was incubated for 15 minutes at 4°C in the dark. After incubation, cells were washed. During centrifugation, an LS MACS® column, composed out of superparamagnetic spheres, was placed to a MACS separator to create a strong magnetic field within the column. Further, the MACS® column was equilibrated with 5 mL of MACS buffer. Additionally, a cell pre-separation filter was put onto the column to prevent cell clots. After centrifugation, the cell pellet was re-suspended in 500 µL of MACS buffer and the cell suspension was added to the column. After that, the MACS®

column was washed three times with MACS buffer. After washing, 5 mL of MACS buffer was added to the column. The column was removed from the magnet and a plunger was inserted to the column and pushed down to remove cells from the column. Eluted cells were washed in the desired media or buffer and counted in a Neubauer counting chamber. To evaluate purity of cells, cells were stained with a fluorochrome-labeled antibody against the cells surface protein CD14 (APC conjugated α-CD14) and measured by fluorescent activated cell sorting (FACS).

3.20 Cell culture and VSOP treatment for flow cytometry

Monocytes were cultured in RPMI media (Gibco) supplemented with 1% Penicillin/Streptomycin, 10% FBS and GM-CSF. After isolation (see **3.18** and **3.19**), monocytes were seeded in a 24-well plate (Thermo Fisher Scientific) at a density of 4.5 x 10^5 cells per well in the above-described complete media. Afterwards, cells rested overnight at 37°C with 5% CO_2. On the next day, monocytes were stimulated with VSOPs. For VSOP treatment, the complete media was removed and VSOP treatment media was added at different concentrations (0.5 mM, 0.75 mM or 1 mM per well). Cells were stimulated with VSOPs for either 30 or 90 minutes. After stimulation, the VSOP-containing media was removed, and wells were washed once with plain RPMI. Then, complete media was added, and cells were incubated at 37°C with 5% CO_2. After 24 h, first aliquots of cell culture supernatants were taken and stored at -80°C for further analysis. Second, for harvesting the cells were washed once with PBS and followed by addition of 5 mM of EDTA in PBS to each well. Plates were incubated for 15 minutes on ice to detach monocytes from plastic. Next, 1 mL of PBS was added to neutralize the EDTA and cells were harvested for further analysis.

3.21 Cell culture and VSOP treatment for RNA sequencing

Monocytes were seeded at a density of 1 x 10^6 cells per well in a 6-well plate (Thermo Fisher). On the next day cells, were treated with 0.75 mM VSOPs as described in **3.20** for 30 minutes. After stimulation, media was removed, and cells were washed carefully with PBS (Gibco). Complete media was added to each well after washing. Cells rested overnight at 37°C with 5% CO_2 before RNA isolation.

3.22 RNA isolation from VSOP-treated monocytes

The RNeasy Mini Kit from Qiagen (Hilden, Germany) was used to isolate RNA from VSOP-treated monocytes. For cell harvest, media was removed and PBS was added to each well to wash cells. PBS was removed and RTL buffer with β-mercaptoethanol was added directly to cell culture plate for cell lysis. Then, cells were detached and lysed by softly scraping the cells

with a pipette tip and repeated re-suspension. The cell suspension was transferred to a 1.5 mL Eppendorf tube containing 70% ethanol (Carl Roth) and mixed. The sample was then transferred to a RNeasy mini spin column. The spin column was centrifuged at 12,000 x g for 15 seconds and the flow-through was discarded. Afterwards, the spin column was washed with 700 µL of RW1 buffer (Qiagen) and two times with RPE buffer (Qiagen), with centrifugation of the column between every washing step. Membrane was then dried by placing the spin column into a fresh collection tube and a centrifugation at 12,000 x g for 1 minute. To collect RNA, the spin column was placed in a RNase free collection tube (Eppendorf). And 50 µL of RNase free water was directly added to the spin column to elute RNA. Next, the RNA Clean and Concentrator Kit from Zymo (Zymo Research, Freiburg, Germany) was used to obtain highly concentrated and pure RNA for sequencing. First, DNA binding buffer was added to the RNA sample. Additionally, an equal volume of 100 % ethanol (Carl Roth) was added, and the sample was transferred to a Zymo spin IC column. The column was centrifuged at 12,000 x g for 30 seconds for RNA binding. The column was washed with RNA wash buffer. After washing, DNase digestion was done directly on the column for 15 minutes at room temperature. After incubation, RNA Prep buffer (Zymo Research) was added, and the column was centrifuged as stated above. Next, the column was washed twice with RNA wash buffer. Then, spin column was transferred to a 1.5 mL RNase-free tube for RNA elution with 16 µL of RNase-free water. RNA concentration and quality was checked by the Agilent 4200 TapeStation System. (Agilent Technologies, Santa Clara, California, US) and the high sensitivity RNA ScreenTape Assay (Agilent Technologies). The RNA sample was mixed with 1 µL of RNA sample buffer (Agilent Technologies) and spun down briefly to collect sample at the bottom of the tube. Afterwards, the sample was vortexed for 1 minute at 2,000 rpm and then heated at 72°C for 3 minutes. Next, the sample was placed on ice for 2 minutes. After incubation the sample was spun down again and loaded into the TapeStation instrument (Agilent Technologies) to assess RNA concentration and RNA integrity number.

3.23 RNA Sequencing

Sequencing of bulk RNA from VSOP-stimulated monocytes was done by the Genomics core facility at the Berlin Institute of Health. Shortly, quality of samples was checked using TapeStation and Qubit. The library was prepared using the NEBNext Ultra II RNA Kit (New England Biolabs, Frankfurt am Main, Germany) and Poly-(A)-Selection and assessed for quality afterwards. Sequencing of total RNA isolates was done on NextSeq 500 (Ilumina, San Diego, CA, USA). Analysis of the data was done in cooperation with Gregor Sturm (Medical University Innsbruck, Trajanoski Lab). Briefly, raw FASTQ files were processed using the nf-core RNA-seq pipeline (Ewels et al. 2020) (Version 3.1.). Here, files were trimmed using trimgalore v0.6.6 and reads were aligned to the GRCh38 reference genome with GENCODE

v33 annotations using STAR v2.7.6a (Dobin et al. 2013). Differential gene expression analysis was performed with DESeq2 v1.30.0 (Love, Huber and Anders 2014). Volcano plots were visualized with the *EnhancedVolcano* package in R software (version 2.4.2) and GO-term enrichment analysis was done using the *topGO* package (version 2.42.0).

3.24 Flow Cytometry

Cell suspensions obtained from cultured monocytes (see **3.20**) were washed in PBS (Gibco) and stained with the live/dead marker Zombi NIR (Biolegend) according to manufacturer's instructions. For surface marker staining, the cell suspension was washed in MACS buffer and antibody mixture prepared in MACS buffer was added to the sample afterwards. For antibody specifications, see **Table 3-6**. After incubation for 15 minutes at 4°C cells were washed again and stained cells were measured by FACSCanto II (BD) and analyzed with FlowJo V10.1 (FlowJo, LLC, Ashalnd, USA).

3.25 Cytometric bead array

Cytokines and chemokines in cell culture supernatant obtained from *in vitro* VSOP-treated monocytes (see **3.20**) were analyzed with the LEGENDplex macrophage and microglia cytometric bead array (CBA, Biolegend) according to manufacturer's instructions. The pre-mixed bead panel targeted following cytokines: CXCL1, TGF-β1, IL-18, IL-23, CCL22, IL-10, IL-12p70, IL-6, TNF-α, G-CSF, CCL17 (TARC), IL-12p40 and IL-1β. Briefly, cell culture supernatant was thawed on ice and diluted in assay buffer. Pre-mixed bead panel was added to each well and incubated at room temperature for 2 h while shaking. Samples were washed, incubated with provided detection antibody and incubated for 1 h at room temperature. Afterwards, streptavidin-PE was added to each well and incubated for 30 minutes at room temperature. Then, samples were washed and dispensed in buffer for data acquisition with FACSCanto II (BD). Data was analyzed with LEGENDplex cloud software (Biolegend).

4 RESULTS

4.1 VSOP tissue distribution after intravenous injection

To determine the most suitable time point for magnetic resonance imaging (MRI) examination after intravenous (i.v.) injection of contrast agent into mice, concentrations of VSOPs in blood and tissue samples were quantified at different time points after injection. It was desired to determine a time point at which the VSOPs clear out of the blood and only remain in the tissue, which should allow better visualization of inflamed tissues in this study. For this, healthy wild-type (WT) mice were injected with 0.03 mmol VSOPs per kg of bodyweight and underwent MRI examination either directly after VSOPs injection (30 minutes) or at 90 minutes, 6 h or 24 h after VSOP injection. Quantification of VSOP concentration in blood, liver, spleen and kidney with magnetic particle spectroscopy (MPS) showed almost no VSOPs remaining in the blood 90 minutes after injection, whereas after 30 minutes, VSOPs were still detectable in the blood sample of respective mice (**Figure 4-1, A**). However, the contrast agent was traceable in liver, spleen, and kidney up to 24 h after injection (**Figure 4-1, B-D**). No VSOPs were quantified in controls not receiving any contrast agent (**Figure 4-1, A-D**).
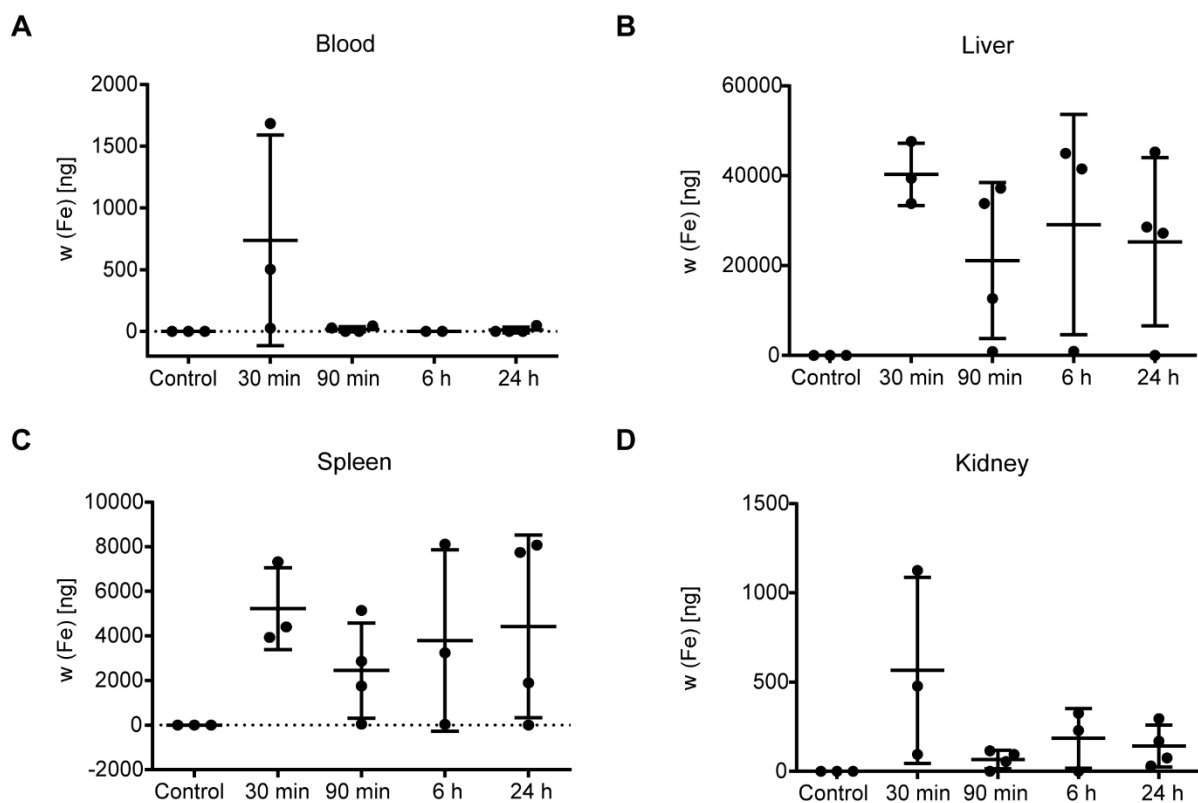
Figure 4-1: <u>Quantification of VSOPs in blood and different tissues.</u> VSOPs are not detectable in blood after 90 minutes with magnetic particle spectroscopy (MPS), while liver and spleen still show high accumulation up until 24 h post application. Quantification of iron content using MPS in blood **(A)**, liver

(B), spleen **(C)** and kidney **(D)** collected after either 30 minutes, 90 minutes 6 h or 24 h after i.v. VSOP injection. Each dot represents an individual mouse. Data is represented as mean ± SD.

Even though MPS is a sensitive quantification method, a successful quantification in isolated organs cannot guarantee a visible contrast change in MR images. Therefore, the presence of VSOPs within the body of the animal was further validated with T2* weighted (T2*w) MRI. Given the imaging modalities, the accumulation of VSOPs was monitored in kidneys and bone marrow. The intestine was not monitored as healthy animals were used for this experiment.

Representative T2*w axial MRI scans of each time point are shown in **Figure 4-2**. In a T2*w MRI sequence accumulation of VSOPs induces a T2 contrast which leads to signal decrease in the image. Thirty minutes after VSOP-injection animals showed accumulation of VSOPs in bone marrow and kidneys (**Figure 4-2, A**). A signal decrease in the bone marrow was visible at each time point, whereas signal decrease in the kidney was not as strong at later time points (**Figure 4-2, B-D**). In the scan of the control animals the bone marrow and kidneys showed no signal decrease (**Figure 4-2, E**). Based on those experiments, animals were further examined with MRI 90 minutes after VSOP application.
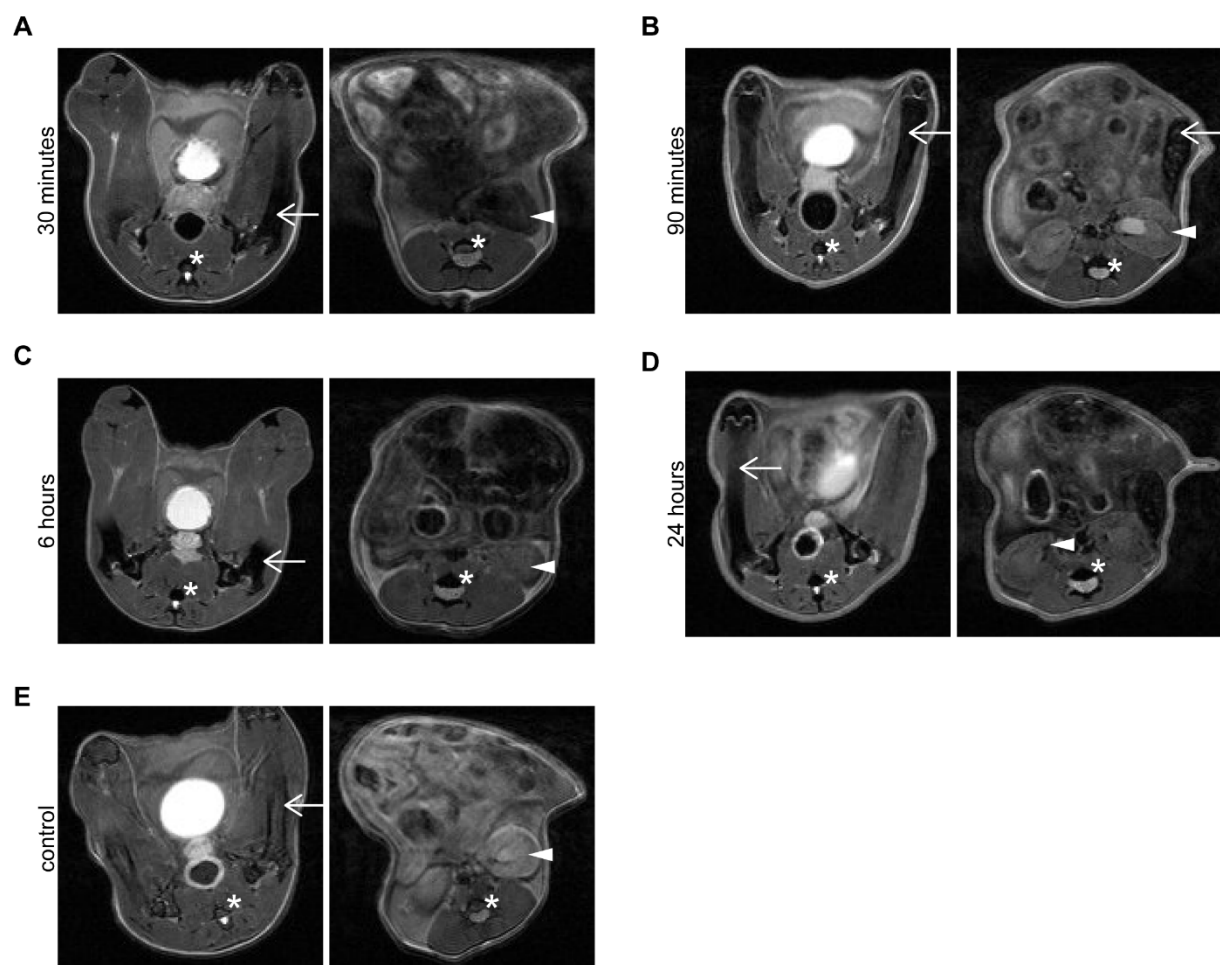
Figure 4-2: In T2*w MRI scans, VSOPs induce a detectable signal decrease in bone marrow and

kidneys at different time points after injection. For each time point representative images of an axial T2*w MRI are shown at two different positions to show bone marrow and kidney. Scans of healthy wild type mice injected with VSOPs showed clear signal decrease in bone marrow in the legs (white arrow) and spine (white asterisk) and kidneys (white arrowhead) 30 minutes after injection **(A)**. After 90 minutes **(B)**, 6 hours **(C)** and 24 hours **(D)** of injection, VSOPs still induced strong signal decrease in bone marrow while signal increased again in the kidneys. In control animal not injected with VSOPs, no signal decrease was observed in bone marrow of legs (white arrow) and spine (asterisk) nor in kidneys (white arrowhead) **(E)**.

4.2 T2*w MRI detects inflammation in the colon of mice with DSS-induced colitis

To investigate successful detection of intestinal inflammation by VSOP-enhanced MRI, dextran sulfate sodium (DSS)-induced colitis mice were injected with contrast agent and examined by MRI after 90 minutes (further referred to as post-MRI). Prior to VSOP injection, an MRI was done as well (further referred to as pre-MRI). Mice had different severities of inflammation as they were treated for different time periods with DSS: 2 days (d2), 4 days (d4), 6 days (d6) and 10 day (d10). D10 animals were treated for 6 days with DSS followed by 4 days of water. The switch to drinking water induced a remission of inflammation in the colon of the animals. For orientation of the animals in the scanner see **Material and Methods section 3.6**. The first position (position 1) refers to the most distal position and the last position (position 6) to the most proximal (**Figure 3-2, A, D**).

First, MRI examinations of each mouse was visually validated for VSOP-induced T2 contrast in MR images. Exemplary pre-MRI and post-MRI images of position 2 summarize successful accumulation of VSOPs around the colon wall of DSS-treated animals for all time points (**Figure 4-3**). In pre-MRI images of position 2 the colon wall appeared in the same brightness or even brighter than the control. After VSOP injection, the signal decreased visually in the colon wall of all DSS-induced colitis mice, while the contrast of the colon wall in the post-MRI image of the control animal appeared unchanged **(Figure 4-3)**.
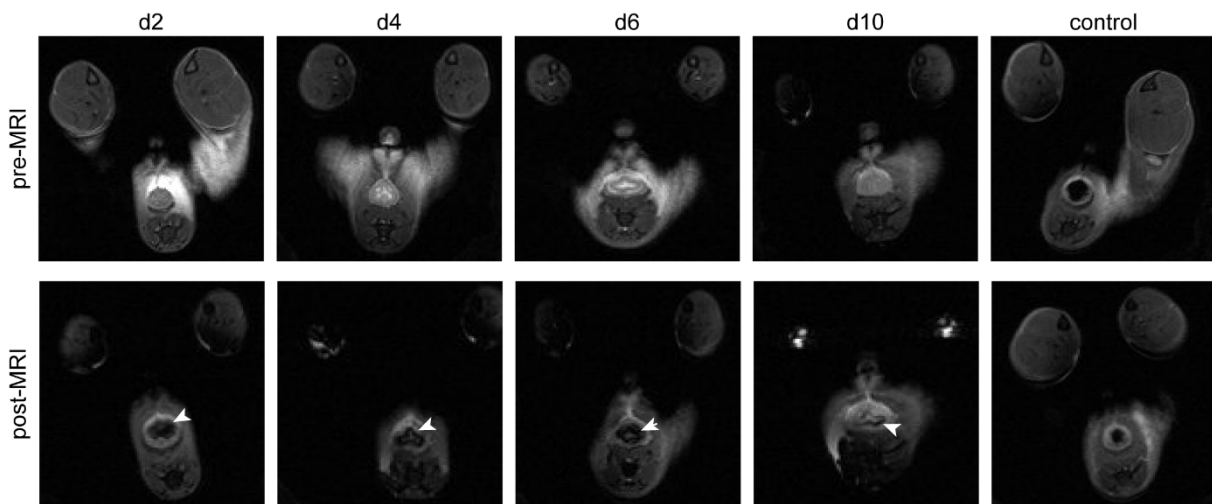
Figure 4-3: <u>Following VSOP injection, the contrast in T2*w MRI decreased visibly in the colon area of DSS-induced colitis mice.</u> Representative images of position 2 in T2*w MRI of DSS-induced colitis mice at different time points before (pre-MRI) and 90 minutes after (post-MRI) VSOP application. In pre-MRI images (upper row), the colon wall appeared brighter when compared to post-MRI images. Here, VSOP accumulation induced a strong signal decrease around the area of the colon. The signal decrease is indicated by white arrowheads. No signal decrease was induced by VSOPs in the colon wall of healthy control mouse.

To support the observed visual finding, the contrast to noise ratio (CNR) in the colon wall was calculated in six contiguous positions of post-MRI images. A decrease of CNR in the colon wall should indicate VSOP induced T2 contrast, while CNR values that are comparable to CNR values in control animals, indicates lack of VSOP accumulation. Additionally, an increase of CNR in colon wall might indicate fluid accumulation that is commonly found at inflamed areas in intestinal tissue.

The most distal part of the colon (position 1) showed a decrease in CNR for all time points, while at d2 and d6 the CNR showed a statistically significant decrease when compared to control (**Figure 4-4, A**). Position 2 showed a tendency of lower CNR for all time points, with CNR at d2 being statistically significant lower when compared to CNR of control (**Figure 4-4 B**). Further, the decrease in CNR was not significantly lower in the following positions (**Figure 4-4, C-F**). While in control animals the CNR was very constant with a low standard deviation, the DSS-treated animals showed a high standard deviation within each group in some positions. Representative MR images of all six positions for each time point (**Figure 4-4, G**) revealed accumulation of VSOP around the colon wall and within the colon lumen. Furthermore, in animals exposed to longer DSS-treatment (d6 and d10) a signal decrease was also observed in more proximal positions. For shorter DSS-treatment, (d2 and d4) a signal decrease was limited to the distal colon. In control mice, no signal decrease was visible around the colon wall in all six positions.

A — Position 1
B — Position 2
C — Position 3
D — Position 4
E — Position 5
F — Position 6
G
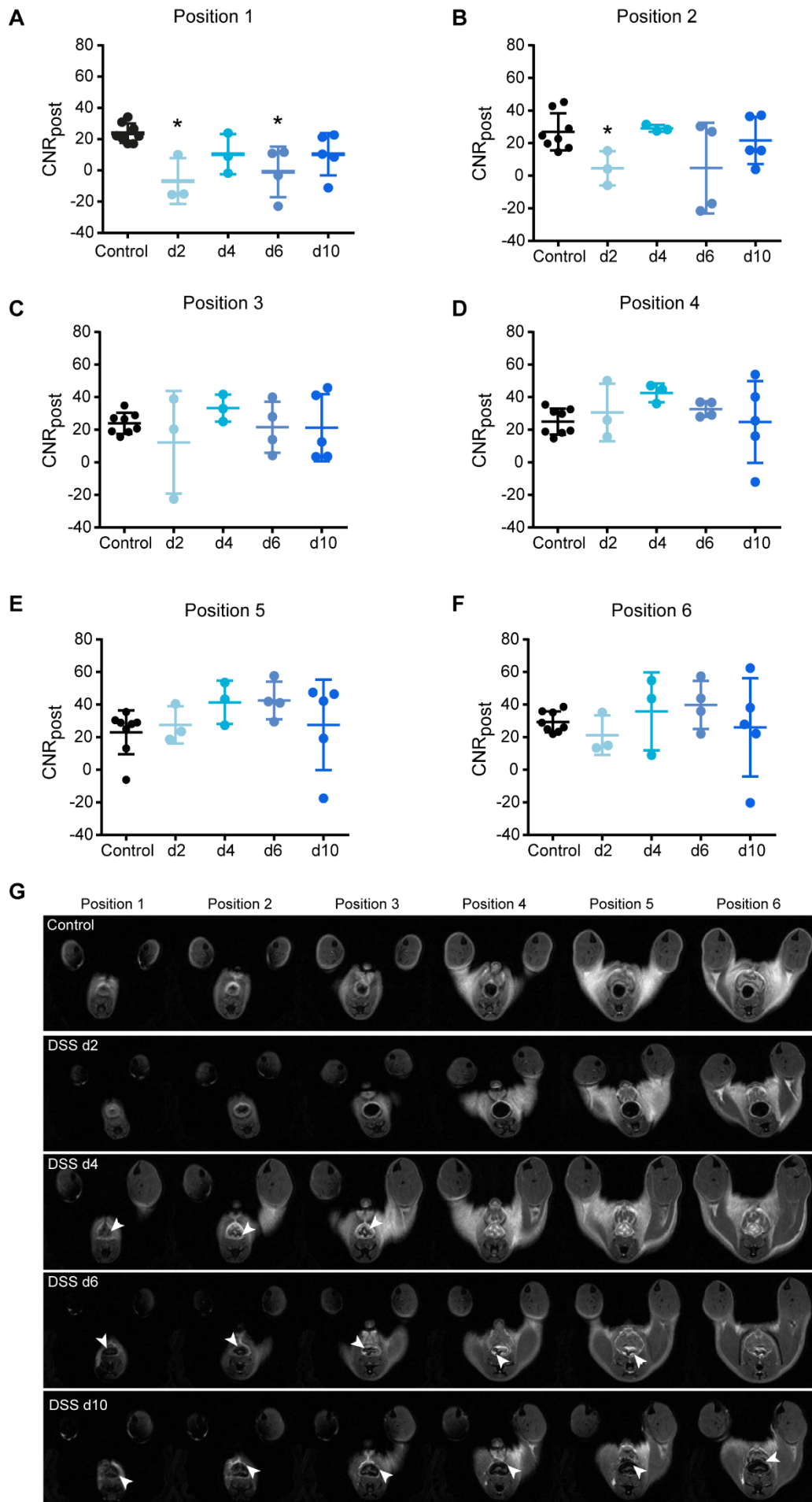
Figure 4-4: <u>Contrast to noise ratio (CNR) decreased in distal colon tissue of DSS-induced colitis animals at early onset inflammation.</u> The CNR in position 1, the most distal part of the colon, showed decrease in CNR when compared to CNR of control animals (n = 8), where the CNR values of d2 (n = 3, *p* = 0.0121) and d6 animals (n = 4, *p* = 0.004) were significantly decreased and non-significantly reduced in d4 (n = 3) and d10 animals (n = 5) **(A)**. The CNR of colon wall in position 2 was significantly lower for d2 animals (*p* = 0.0242) and showed a decreasing trend for d4, d6 and d10 mice when compared to control animals **(B)**. The more proximal position 3 **(C)**, 4 **(D)**, 5 **(E)** and 6 **(F)** showed a decrease in some of the animals but an elevated CNR in others. VSOP accumulation in six representative sub-sequential positions for each time point during DSS treatment is indicated with white arrowheads, while no accumulation was detected in control animal **(G).** Statistical significance was tested with Mann-Whitney test (non-parametric *U*-test) and marked with * if *p* ≤ 0.05. Data is represented as mean ± SD. Figure is adapted from Golusda *et al.* 2022.

4.3 Intestinal inflammation is not detectable with T2*w MRI of transfer colitis and *TNF$^{\Delta ARE}$* mouse models

Additional mouse models of intestinal inflammation were investigated to validate accumulation of VSOPs in inflamed regions of the intestine. First, the transfer colitis model was chosen. In this model mice develop an inflammation in the colon after transfer of CD4$^+$CD45RB^{hi} cells into immune deficient *Rag^{1tm1Mom}* mice. Second, the *TNF$^{\Delta ARE}$* mouse model was used. Here, animals develop inflammation in the terminal ileum due to a systemic overexpression of tumor necrosis factor (TNF).

After pre-MRI, VSOPs were injected into transfer colitis animals and respective controls. Mice were then examined 90 minutes after VSOP injection (post-MRI). Again, in T2*w MRI the VSOPs were expected to induce signal decrease in the inflamed colon wall as seen in the DSS-induced colitis model. However, in transfer colitis animals no accumulation of VSOPs was visually detected (**Figure 4-5**). As expected, in post-MRI images of control mouse the colon wall appeared in same contrast as in pre-MRI images (**Figure 4-5, A**). Strikingly, this was equally observed in MRI examinations of the colon wall from transfer colitis mice at every time point (**Figure-4-6, B-E**). As signal decrease was not visually detectable, no further calculation of the CNR in colon wall was done.
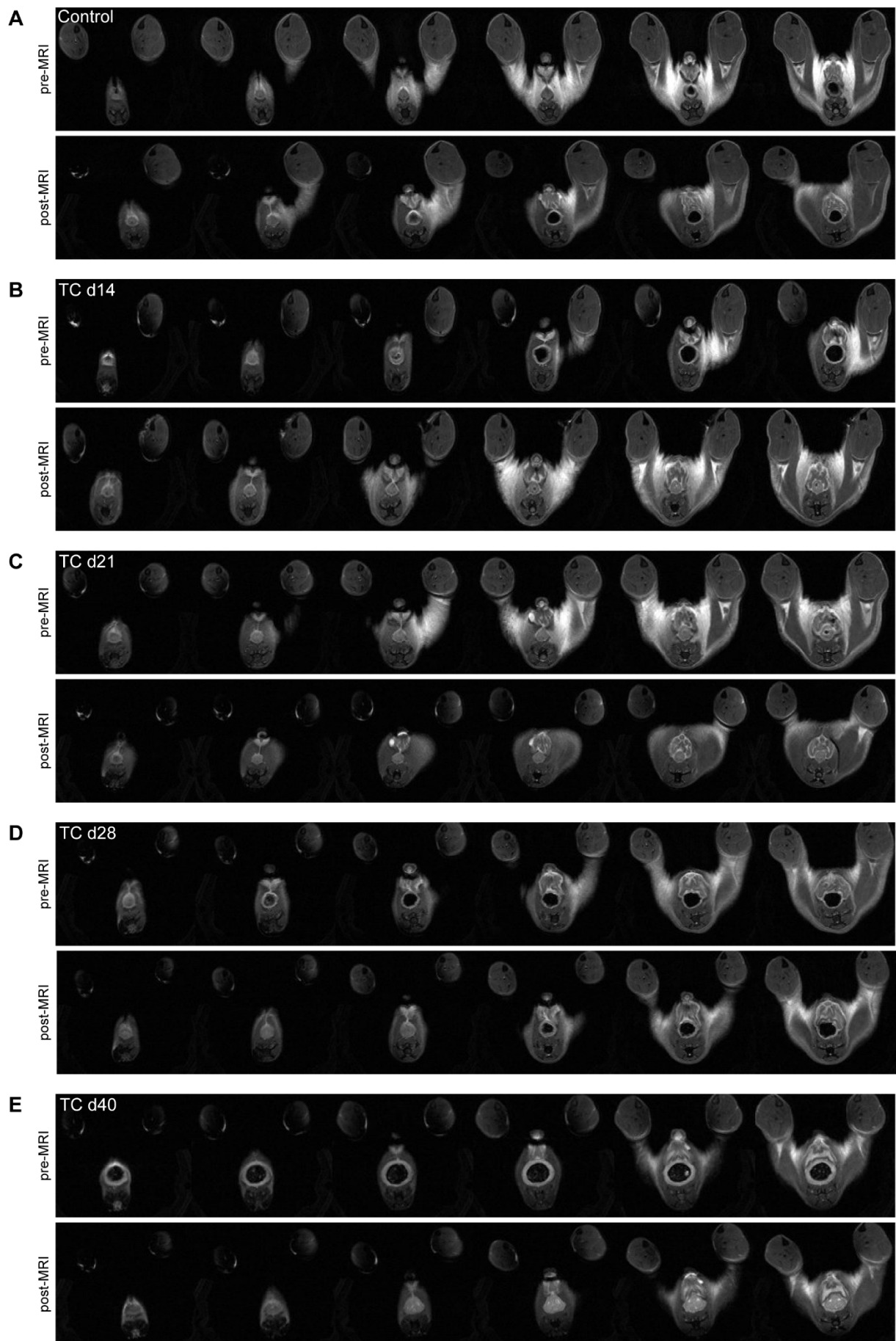
Figure 4-5: VSOPs do not accumulate in inflamed colons of transfer colitis mice. Representative axial

images of T2*w pre- and post-MRI of control animals (n=7) **(A)**, transfer colitis mice at day 14 (d14, n=2) **(B)**, transfer colitis mice at day 21 (d21, n=4) **(C)**, transfer colitis mice at day 28 (d28, n=3) **(D)** and transfer colitis mice at day 40 (d40, n=4) **(E)**. No VSOP-induced T2 contrast was detectable in inflamed colon.

In the $TNF^{\Delta ARE}$ mouse model, inflammation is induced predominantly in the terminal ileum. Therefore, accumulation of VSOPs was expected in this area. The ileum was localized by searching axial MRI sequences and identifying slices containing the cecum. Within the same plane the ileum was localized. However, no accumulation of VSOPs was visually detectable in T2*w MRI of $TNF^{\Delta ARE}$ mice. Representative images from the latest time point assessed (w14, which is expected to show the highest rate of inflammation) were chosen to underline these results (**Figure 4-6**). In $TNF^{\Delta ARE}$ mice, the localization of the ileum was easier than in control mice due to a thicker ileal wall owing to the inflammation (**Figure 4-6, B** white arrows).
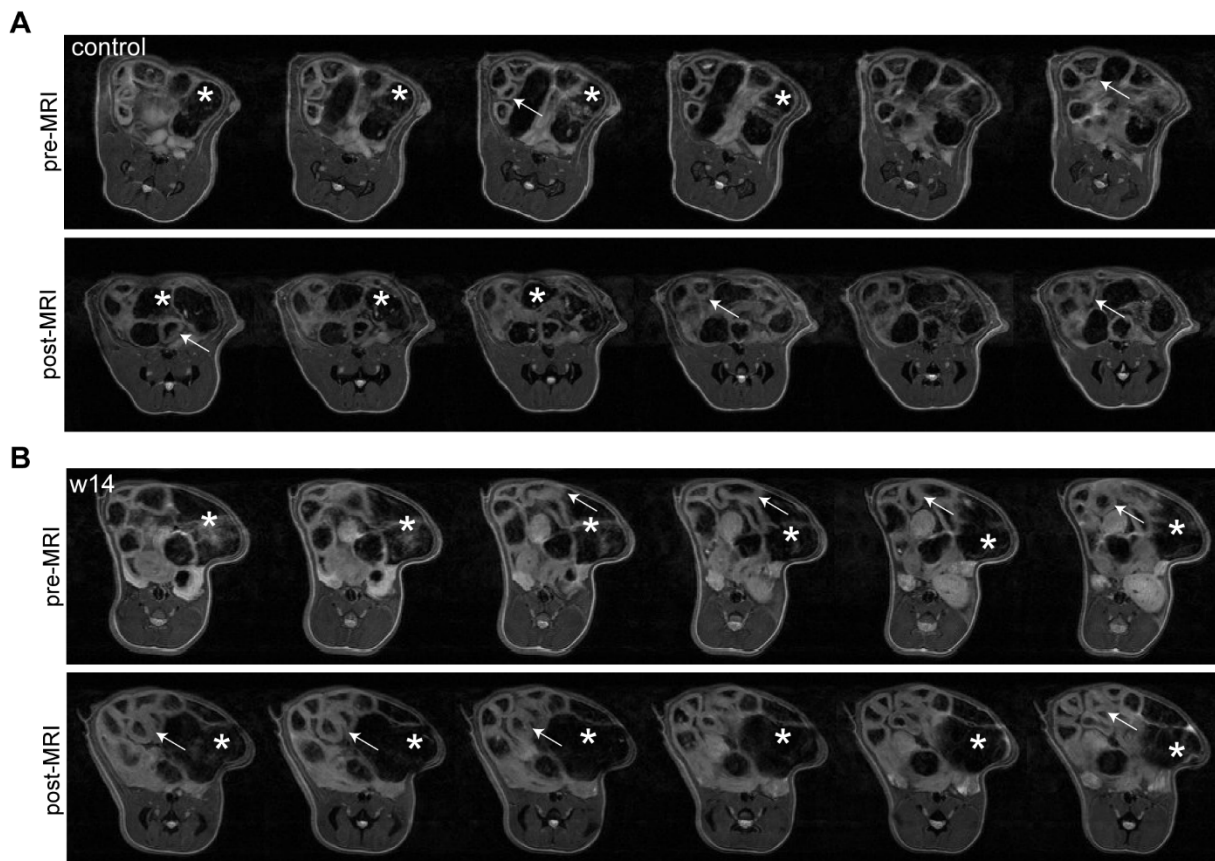
Figure 4-6: <u>VSOPs do not accumulate in inflamed ilea of $TNF^{\Delta ARE}$ mice.</u> Representative six subsequential axial images of T2*w pre-MRI (upper row) and post-MRI (lower row) of healthy WT control (n=4) **(A)** and latest time point w14 of $TNF^{\Delta ARE}$ mice (n=6) **(B).** Asterisks in each image refer to the location of the cecum and arrow points to wall of the ileum, which was thickened in $TNF^{\Delta ARE}$ mice compared to control animals.

4.4   VSOPs detect early onset changes in inflamed colon tissue

Inflammation of the colon and ileum of the mouse models was evaluated histologically by H&E staining, respectively. Tissue for histological evaluation was taken in the same position each time: For DSS-induced colitis and transfer colitis models, a colon tissue sample was taken 1cm apical from anus and for $TNF^{\Delta ARE}$ model an ileum tissue sample was taken 1 cm apical of cecum, to ensure consistency in analysis as tissue composition and severity of inflammation might change with location in the intestine.

In DSS-induced colitis, the histological scoring of inflammation showed an increase in inflammation score after day 6 of DSS-treatment (**Figure 4-7, A**). Early time points of DSS-treatment did not induce histological tissue changes (**Figure 4-7, C**). During severe inflammation (later time points of DSS-treatment), severe ulcerations and epithelial damage was detectable in colon tissue (**Figure 4-7, D**).

In the histological scoring of transfer colitis colon tissue sections, the inflammation score significantly increased at day 28 in experimental time course (**Figure 4-7, E**). During early disease stages (day 14) no severe tissue changes were detectable in H&E staining of colon tissue sections (**Figure 4-7, G**). Here, colon tissue represented immune cell infiltration and severe crypt hyperplasia (**Figure 4-7, H**).

Remarkably, the ileum tissue of $TNF^{\Delta ARE}$ mice showed an increased inflammation score already at early time points and inflammation remained high throughout all time points (**Figure 4-7, I**). During early time point inflammatory cell infiltrations and villous blunting was observed (**Figure 4-7, K**) which is also true for later time points (**Figure 4-7, L**).
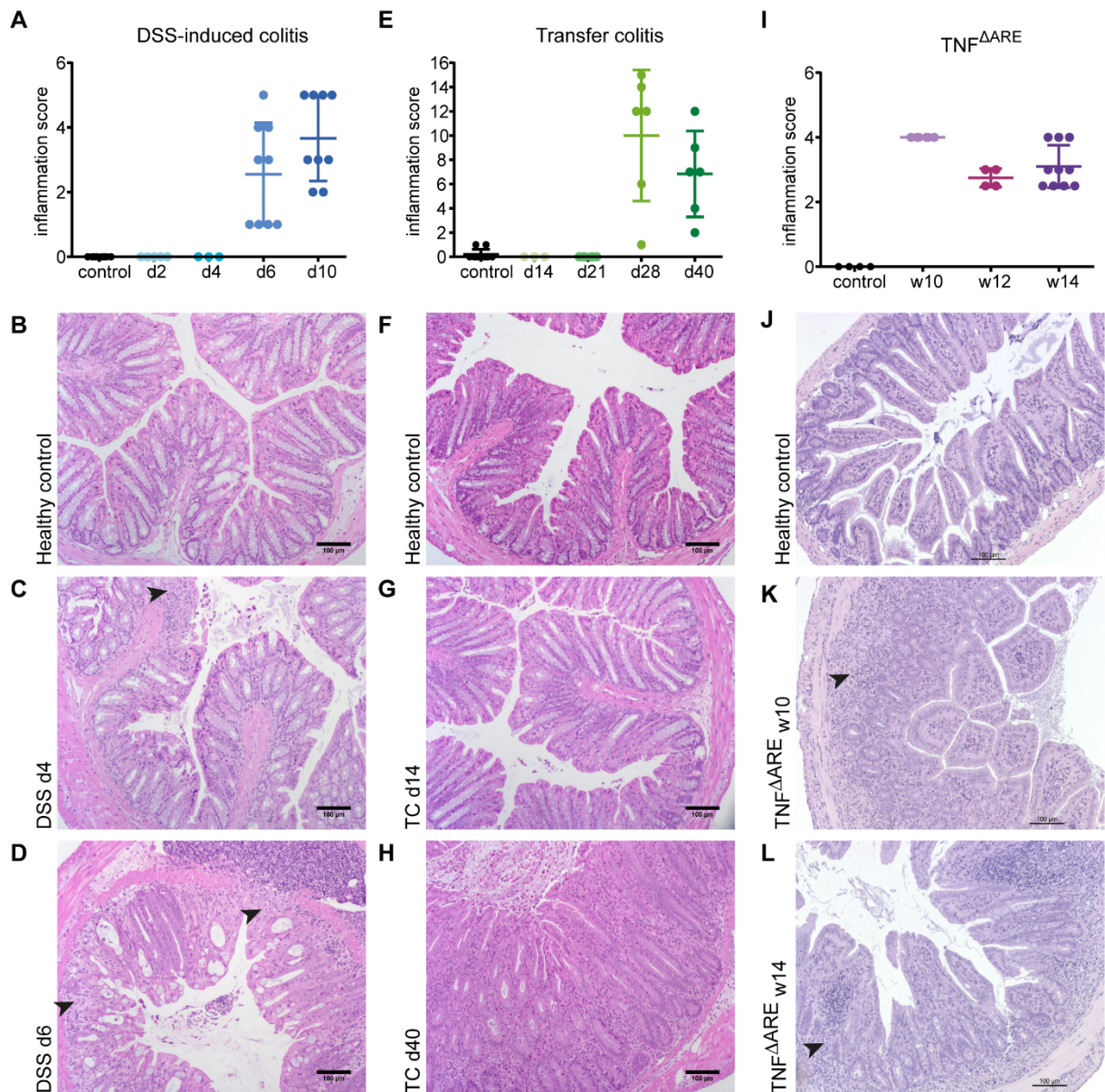
Figure 4-7: <u>All models successfully develop inflammation in the colon or ileum.</u> DSS-induced colitis colon tissues showed no major pathological changes at d2 (n=5) and d4 (n=3) in inflammation score while inflammation score increased at d6 (n=9) and d10 (n=9) when compared to control (n=8) **(A)**. Representative H&E staining of tissue sections of healthy control **(B)**, early time point of DSS-treatment at d4 **(C)** and severely inflamed colon tissue at d6 with major cell infiltrations in mucosa (arrow heads) **(D)**. In transfer colitis, no major pathological changes appeared at d14 (n=3) and d21 (n=6) but inflammation score increased at d28 (n=6) and d40 (n=6) when compared to control (n=10) **(E)**. Representative H&E staining of tissue sections of healthy control **(F)**, d14 for early disease stage **(G)** and d40 for late disease stage **(H)** with major characteristic of crypt hyperplasia presented at late disease stage. In the ileum of $TNF^{\Delta ARE}$ mouse model, inflammation scores are high in each time point indicating equal inflammation severity at w10 (n=6), w12 (n=4) and w14 (n=10) when compared to control (n=4) **(I)**. Representative H&E staining of tissue sections of healthy wild type control **(J)**, at w10 **(K)** and at w14 **(L)** with arrow heads pointing to inflammatory cell infiltration. Data represented in mean ± SD and each dot represents one mouse. Scale bar equals 100 µm. Figure and data were partially

adapted from Golusda *et al.* 2022.

In the DSS-induced colitis model, VSOP accumulated in the very distal part of the colon during early onset inflammation (**Figure 4-8, B**) as well as during severe inflammation (**Figure 4-8, C**). However, colon tissue from mice at early onset inflammation (d2 and d4) obtained a histological inflammation score of 0 (**Figure 4-7, A**).

When all animals in DSS-induced colitis model were grouped based on their histological inflammation score of 0, the CNR in position 1 of those animals was significantly lower when compared to CNR in position 1 of healthy control animals (**Figure 4-8, D**). Further, all animals that were histologically scored with 3 were grouped and showed an equally significant decrease in CNR of position 1. Therefore, accumulation of VSOPs might be driven by changes within early onset inflamed tissue which cannot be visualized by histopathology and characterized by regular scoring system. For further investigation of tissue changes during inflammation, components of the extracellular matrix (ECM) in colon and ileum of the used mouse models were investigated.
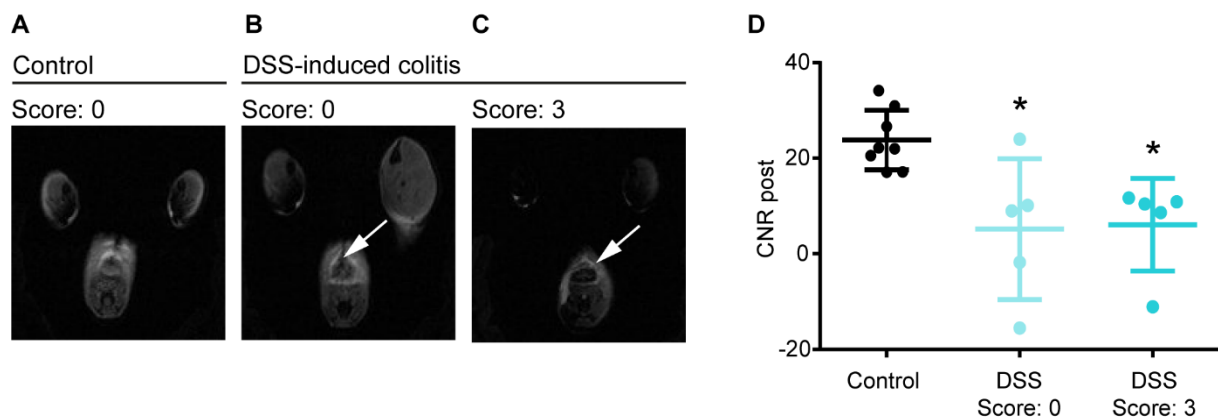
Figure 4-8: <u>In DSS-induced colitis, VSOP accumulation in position 1 of T2*w MRI is detectable in histologically unscored colon tissue.</u> In healthy control animals, no VSOP-induced signal decrease is detectable in position 1 of T2*w MRI **(A)**. In DSS-induced colitis mouse, histologically scored with a 0, VSOP-induced signal decrease is detected around colon **(B)** as well as in DSS-induced colitis mouse, scored with a 3 **(C)**. DSS-induced colitis mice grouped by inflammation score showed a significant decrease in CNR in position 1 when scored with 0 (n = 6, *p* = 0.0295) and 3 (n = 5, *p* = 0.0016) when compared to control CNR (n = 8). Statistical significance was tested with Mann-Whitney test (non-parametric *U*-test) and marked with * if *p* ≤ 0.05. Data represented in mean ± SD. Figure and data were adapted from Golusda *et al.* 2022.

4.5   ECM composition differs in mouse models of intestinal inflammation

In histopathological non-inflamed colon tissue of DSS-induced colitis mice, VSOP successfully induced a signal decrease. Therefore, the accumulation of the contrast agent seemed to be

facilitated by tissue changes, which were not considered using histopathological scores as infiltrations are too inconspicuous. As changes within the ECM are early indicators of tissue damage its composition was further investigated.

To this end, glycosaminoglycans in the ECM of colon tissue of healthy control mice and animals with severe inflammation owing to DSS-induced colitis or transfer colitis were quantified by high-pressure liquid chromatography (HPLC).

The content of hyaluronic acid (HA) and chondroitin sulfate (CS) 4S (CS-4S) was measured in each model. Surprisingly, the amount of HA and CS-4S differed between the two models (**Figure 4-9**). In DSS-induced colitis, HA was found to be increased in inflamed tissue and the amount of CS-4S was decreased (**Figure 4-9, A**), whereas in transfer colitis mice, HA decreased and CS-4S increased in inflamed colon tissue, compared to control tissue (**Figure 4-9, B**).
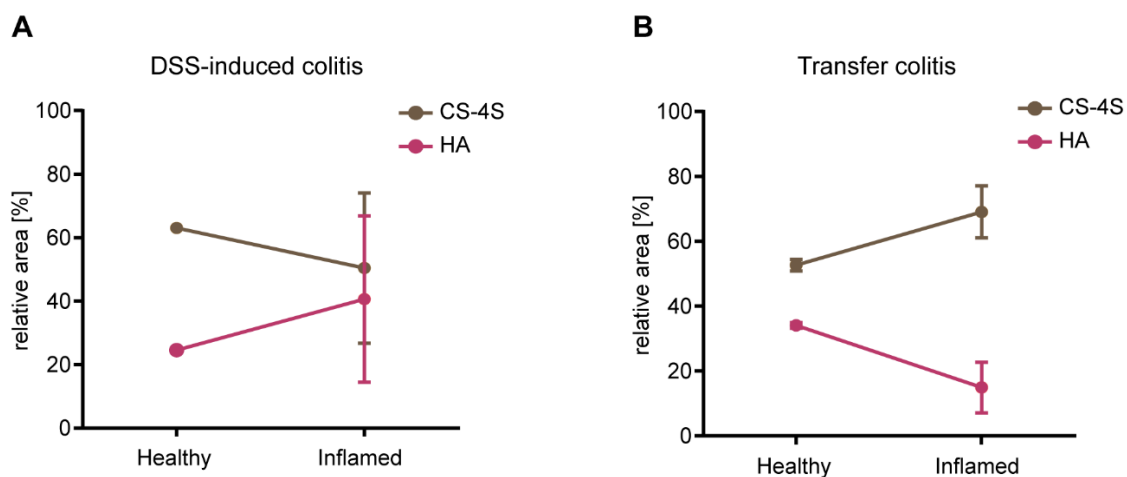
Figure 4-9: <u>Hyaluronic acid (HA) and chondroitin sulfate 4S (CS-4S) content changes in inflamed colon tissue of DSS-induced colitis and transfer colitis model.</u> In inflamed colon tissue of DSS-induced colitis (n = 4), HPLC analysis showed an increase in HA and a decrease in CS-4S compared to colon tissue from a healthy control animal (n = 1) **(A)**. In inflamed colon tissue of transfer colitis mice (n = 4), HPLC analysis showed a decrease in HA and an increase in CS-4S content compared to colon tissue from healthy control animals (n = 3) **(B)**. Data represented in mean ± SD. Figure and data were adapted from Golusda *et al.* 2022.

Further, immunohistochemistry of tissue sections for each model was done for deeper insights into distribution and content of HA and CS. With the HPLC method the sulfation pattern of CS disaccharides can be determined. However, such precise analysis is not possible with immunohistochemistry, therefore tissue sections were stained for CS proteoglycan 4 (CSPG4). So, colon and ileum paraffin sections were stained with anti-CSPG4 and HA-binding protein (HABP2) to approximate HA and CS content.

Quantification of stained areas confirmed the HPLC results: In DSS-induced colitis, HA content increased and CSPG4 content decreased during the disease course (**Figure 4-10, A**). In colon of healthy controls, HA is expressed in a thin layer in the submucosa and mucosa and CSPG4 is localized in epithelial cells and goblet cells (**Figure 4-10, B**). During mild inflammation, tissue showed small cell infiltrations and was slightly edematous. This was accompanied by a slight increase in HA expression, represented by a marginally thicker band of HA expression in the submucosa and between crypts (**Figure 4-10, C**). In severely inflamed colon tissue of DSS-induced colitis, mucosa and submucosa showed very high levels of HA and remarkably lower expression of CSPG4 in the epithelial area (**Figure 4-10, D**). In transfer colitis, the area stained for HA did not change during the disease course whereas CSPG4 expression significantly increased at day 28 (**Figure 4-10, E**). In colons of healthy control mice, HA and CSPG4 expression was comparable to controls in DSS-induced colitis (**Figure 4-10, F**). In early disease stages, the expression patterns did not change. At the latest time point (day 40), a high amount of CSPG4 was present in the mucosa due to crypt hyperplasia whereas HA did not change within tissue (**Figure 4-10, G**). In colon tissue sections of $TNF^{\Delta ARE}$ mice, the HA content showed a trend to increase during disease course and dropped at latest time point (week 14). Furthermore, the CSPG4 content showed a higher trend compared to control but did not significantly increase (**Figure 4-10, I**). In healthy ileum, HA was observed in mucosa between villi and CSPG4 located around epithelial cells in villi (**Figure 4-10, J**). In 10 weeks old $TNF^{\Delta ARE}$ mice the HA and CSPG4 localization was more diffuse in the mucosa (**Figure 4-10, K**). At week 14 the HA content in villi was significantly less and CSPG4 was still located between epithelial cells (**Figure 4-10, L**).
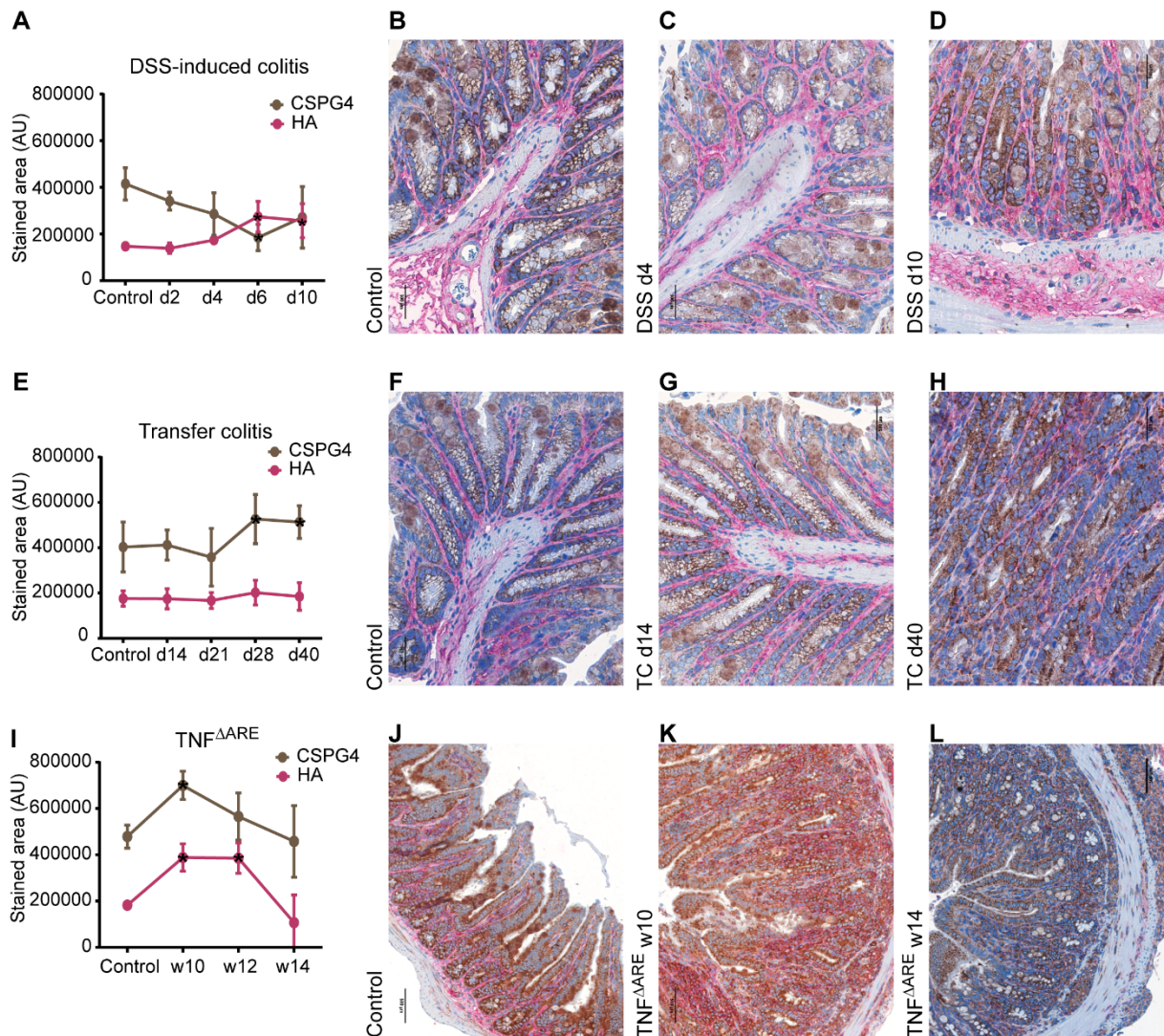
Figure 4-10: <u>Models of intestinal inflammation show different expression of HA and CSPG4 during inflammation.</u> Quantification of the stained area in colon tissue of DSS-induced colitis at d2 (n = 5), d4 (n = 4), d6 (n = 9) and d10 (n = 12) showed a significant increase in HA (red) expression at d6 (p = 0.0101) and d10 (p = 0.0240) when compared to healthy controls (n = 3). Further, a significant decrease in CSPG4 at d6 (p = 0.0043) could be detected **(A)**. In colons of healthy controls, HA expression is present in submucosa and mucosa, while CSPG4 is expressed by epithelial and goblet cells **(B)**. At an early time point of DSS-treatment (d4), HA expression is increased in the mucosa between the crypts **(C)**. In severely inflamed tissue (d10), many edema were present and HA expression increased in mucosa and submucosa, whereas CSPG4 content appeared to be reduced in mucosa **(D)**. Quantification of positively stained tissue in transfer colitis mice at d14 (n = 3), d21 (n = 5), d28 (n = 6) and d40 (n = 9) showed no changes in HA expression and a significant increase in CSPG4 expression at d28 (p = 0.0431) and d40 (p = 0.0331) compared to healthy control tissue (n = 24) **(E)**. Image of stained control tissue showed HA expression in mucosa and submucosa and CSPG4 expression in epithelial and goblet cells in mucosa **(F)**. At an early time point of transfer colitis (d14), expression pattern of HA and CSPG4 **(G)** is comparable to control tissue while in more inflamed tissue (d40), CSPG4 expression is more prominent in the mucosa and HA expression remained the same **(H)**. Quantification of stained area in colon tissue sections of TFN$^{\Delta ARE}$ mouse model at w10 (n = 14), w12 (n = 5) and w14

(n = 14) showed a trend of increase in CSPG4 content with a drop at w12 and HA content showed a trend to increase of disease course and dropped at w14 when compared to control (n = 3). Representative image of stained ileum section shows HA in mucosa between villi and CSPG4 located around epithelial cells **(J)**. At 10 weeks of age HA and CSPG4 expression patterns are more diffuse in the ileum **(K)**, which is still observed at 14 weeks of age with a lower HA expression in the mucosa between villi **(L)** Statistical significance was tested with ordinary one-way ANOVA and marked with * if $p \leq 0.05$. Data represents mean ± SD. Figure and data were partially adapted from (Golusda et al. 2022).

## 4.6 VSOPs cluster with CD44^{+} macrophages in tissues of mice with DSS-induced colitis but remain in endothelial cells in transfer colitis

The contrast decrease in MRI indicated that VSOPs accumulate in colon tissue. Nevertheless, it was of interest to define the location of VSOPs within colon tissue more precisely. Since VSOPs are doped with the metal europium the technique of imaging mass cytometry (IMC) which is a combination of tissue laser ablation and mass cytometry based metal detection, is suitable for particle detection within colon tissue sections. For IMC, the tissue sections were stained with antibodies conjugated to metal isotopes which are then detected by mass cytometry. Sections of a tissue micro array (TMA) of colon tissue of DSS-induced colitis (healthy control, d4, d6 and d10) and transfer colitis mice (healthy control, d21, d28, d40) were stained with various antibodies against proteins expressed by immune cells or specific cell types in colon tissue according to **Table 3-4**.

Images of IMC measurement showed successful detection of VSOPs (**Figure 4-11, A-C**) in colon tissue sections of DSS-induced colitis. In colon tissue sections of healthy controls, VSOPs were rarely detectable which is in agreement with the MRI data (**Figure 4-11, A**). VSOPs were already visible in the mucosa of mildly inflamed colon tissue of a d4 DSS-treated mouse (**Figure 4-11, B**) in the severely inflamed colon tissue of d6 DSS-treated mice (**Figure 4-11, C**). An unsupervised Phenograph clustering (Levine et al. 2015, Lehmann et al. 2021) of DSS-induced colitis colon tissue sections with showed clustering of VSOPs with CD68^{+}F4/80^{+} macrophages expressing CD44 (cluster 7, cluster 9 and cluster 10). Further, VSOPs cluster with CD31^{+} endothelial cells (cluster 37) (**Figure 4-11, D**).

Additionally, time points of DSS-treatment were investigated separately. For this, the data of colon tissue sections of healthy control, d4 and d6 were displayed in t-distributed stochastic neighbor embedded (tSNE) plots (**Figure 4-11, E-G**). Each group showed different abundance of clusters, depending on the treatment. Especially VSOPs clusters were profoundly more abundant at d6 of DSS-treatment (**Figure 4-11, G**) underlining higher accumulation of VSOPs in case of present inflammation.
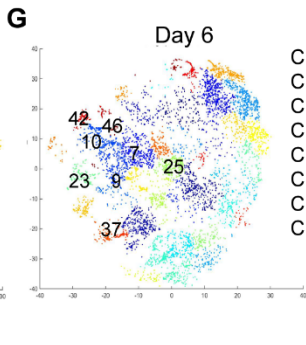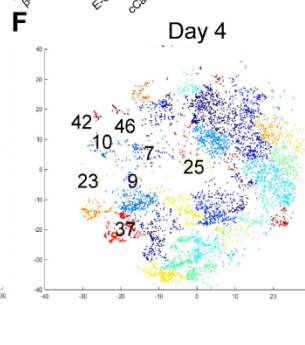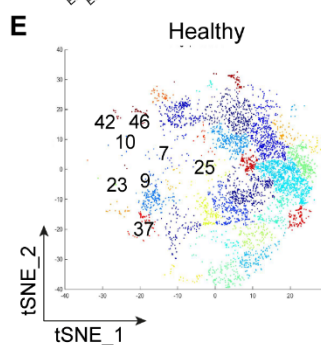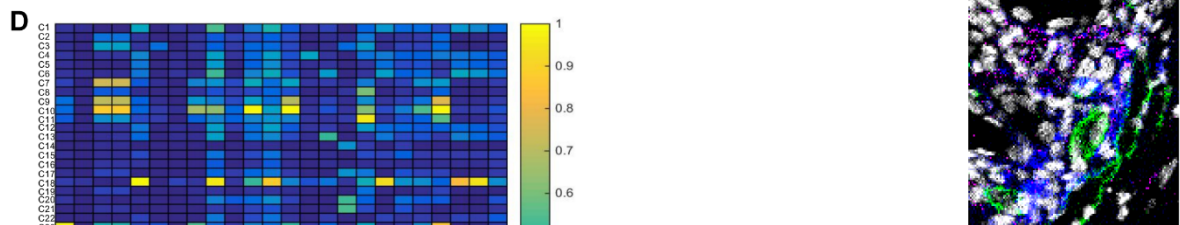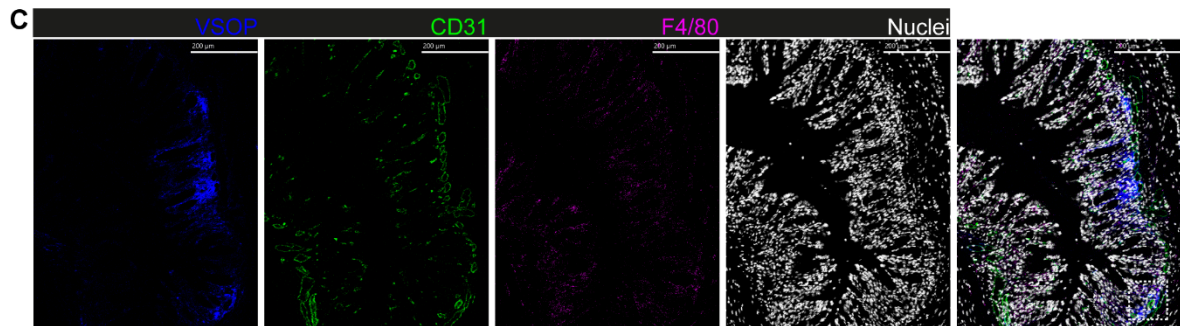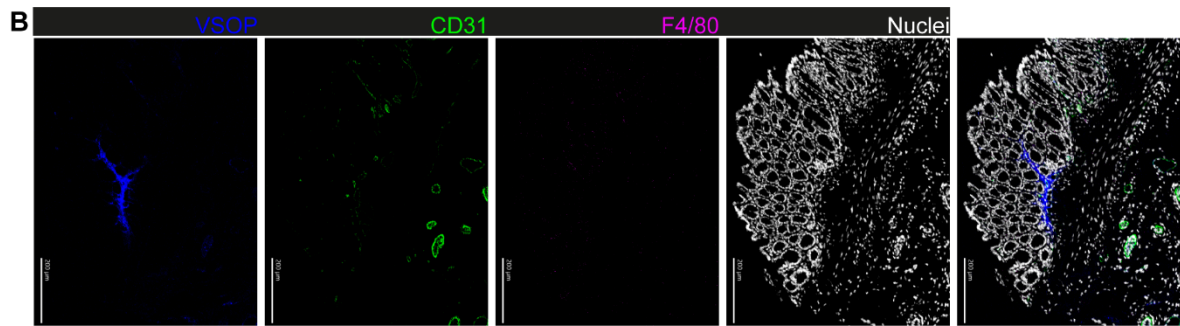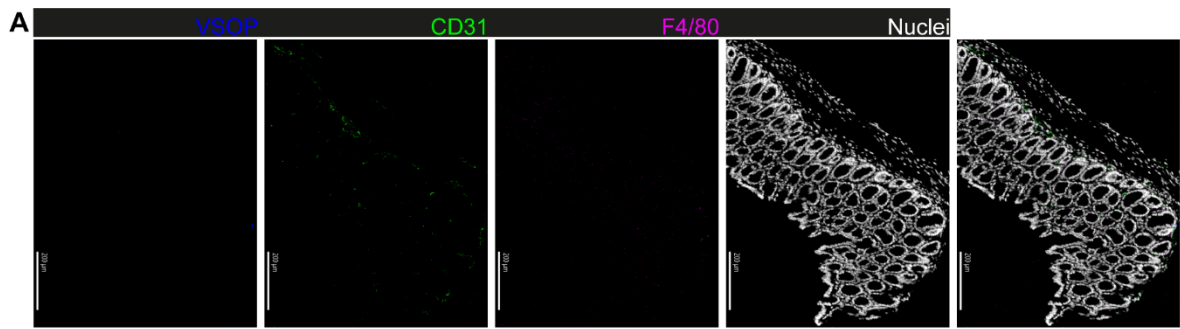
Cluster 7: CD68, F4/80, CD44
Cluster 9: CD68, F4/80, CD44
Cluster 10: CD68, F4/80, CD44
Cluster 23: CD11b, F4/80, CD44
Cluster 25: F4/80, CD44
Cluster 37: CD31, CD44
Cluster 42: CD103, CD3
Cluster 46: F4/80, Caspase-3

Figure 4-11: <u>In DSS-induced colitis mice VSOPs cluster with CD68⁺F4/80⁺CD44⁺ macrophages and CD31⁺ endothelial cells.</u> In the representative image of a colon tissue section of a healthy control mouse with VSOP (blue), CD31 (green), F4/80 (magenta) and nuclei (white) including a merged image (right), no VSOPs are present in colon tissue **(A)**. Representative IMC image of VSOPs, CD31, F4/80 and nuclei channel from d4 DSS-treatment with accumulation of VSOPs (blue) in mucosa **(B)**. Representative IMC image of VSOPs, CD31, F4/80 and nuclei channel from d6 DSS-treatment with more prominent VSOP accumulation in mucosa and VSOPs co-localized with CD31 and F4/80, including a blow-up of the marked area **(C)**. Unsupervised Phenograph analysis of DSS-induced colitis at d2 (n = 2), d4 (n = 3), d6 (n = 3) and d10 (n = 3) resulted in a segmentation of 47 clusters and was summarized in a heatmap with the mean expression of each marker (dark blue refers low expression and yellow refers to high expression), showing clustering of VSOPs with CD31⁺ endothelial cells (Cluster 37), CD68⁺F4/80⁺ macrophages expressing CD44 (Cluster 7, 9 and 10), CD3⁺ T cells expressing CD103⁺ (Cluster 42) and F4/80⁺ CD11b⁺ macrophages expressing CD44 (Cluster 23) **(D)**. Additional a data for healthy control (n = 2), d4 (n = 2) and d6 (n = 2) DSS-induced colitis mice was displayed separately in tSNE plots, showing higher abundance of VSOP-containing clusters at d4 of DSS-treatment **(F)** and an even more prevalent abundance at d6 **(G)**. Clusters are indicated by their numbers within tSNE graphs and their most prominent marker are stated in the legend on the right. Scale bar in images refers to 200 µm. Figure and data were partially adapted from Golusda *et al.* 2022.

Sections of a TMA of colon tissue from transfer colitis mice underwent the same staining and analysis. In representative IMC images of healthy control mouse, VSOPs (blue) were visually not detectable (**Figure 4-12, A**) as well as in early time point of disease course (**Figure 4-12, B**). In case of severe inflammation during later time point (d40), VSOPs were present in mucosa (**Figure 4-12, C**). Here, VSOPs co-localized with CD31⁺ endothelial cells. Nevertheless, the accumulation of VSOPs within severely inflamed colon tissue was not sufficient to induce a signal decrease in T2*w MRI images for visual detection. Unsupervised Phenograph analysis of transfer colitis IMC data showed a lower amount of VSOP-positive clusters. Here, VSOPs clustered mainly with CD31⁺ endothelial cells (cluster 20). Further, VSOPs clustered to a lesser extent with F4/80⁺ macrophages (cluster 25) and CD11b⁺, CD11c⁺, Ly6C⁺ macrophages expressing CD44 (cluster 24) (**Figure 4-12, D**).
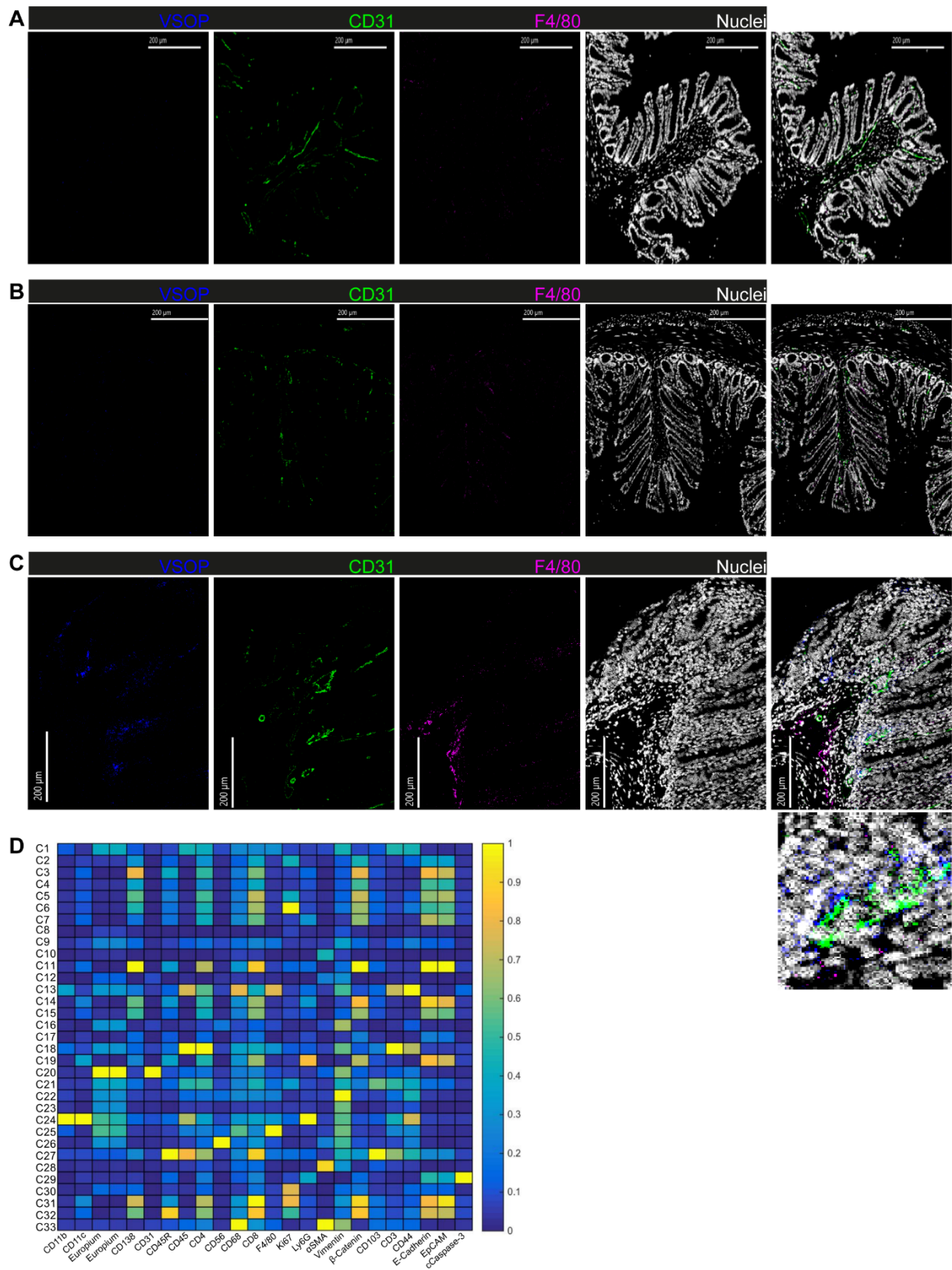
Figure 4-12: <u>In transfer colitis mice VSOPs cluster with CD31+ endothelial cells.</u> Colon tissue of healthy controls showed no signal in the VSOP channel (blue) **(A)**. Mildly inflamed colon tissue of d14 transfer colitis mouse did not show accumulation of VSOPs **(B)** while severely inflamed colon tissue of d40 transfer colitis mouse showed accumulation of VSOPs (blue) in the mucosa and co-localization with CD31+ endothelial cells (green) **(C)**. Unsupervised Phenograph analysis of IMC data resulted in a

segmentation of 33 clusters and was summarized in a heatmap with the mean expression of each marker (dark blue refers low expression and yellow refers to high expression). Further the heatmap underlined co-localization of VSOPs with $CD31^+$ endothelial cells (cluster 20) and to lesser extent with $CD11b^+$, $CD11c^+$, $Ly6C^+$ macrophages expressing CD44 (cluster 24) and with $F4/80^+$ macrophages (cluster 25) **(D)**. Scale bar in images refers to 200 µm. Figure and data were partially adapted from Golusda *et al.* 2022.

To compare the abundance of VSOP-positive cell types within the different mouse models, a new unsupervised Phenograph clustering of IMC data was performed. For this, DSS-induced colitis and transfer colitis colon tissue samples underwent unsupervised Phenograph clustering together and results were summarized in a heat map (**Figure 4-13, A**) and tSNE plot (**Figure 4-13, B**). The heat map showed that the main cluster containing VSOPs is cluster 20 with $F4/80^+CD68^+$ macrophages expressing CD44. The overlaid tSNE plot further underlined the presence of different clusters in the two mouse models and therefore different cell types. Further, quantification of cells within cluster 20 resulted in a significant lower abundance of VSOP containing $F4/80^+CD68^+$ macrophages expressing CD44 in transfer colitis (0.44±0.35 %) when compared to DSS-induced colitis model (3.55±1.97 %) (**Figure 4-13,C**).
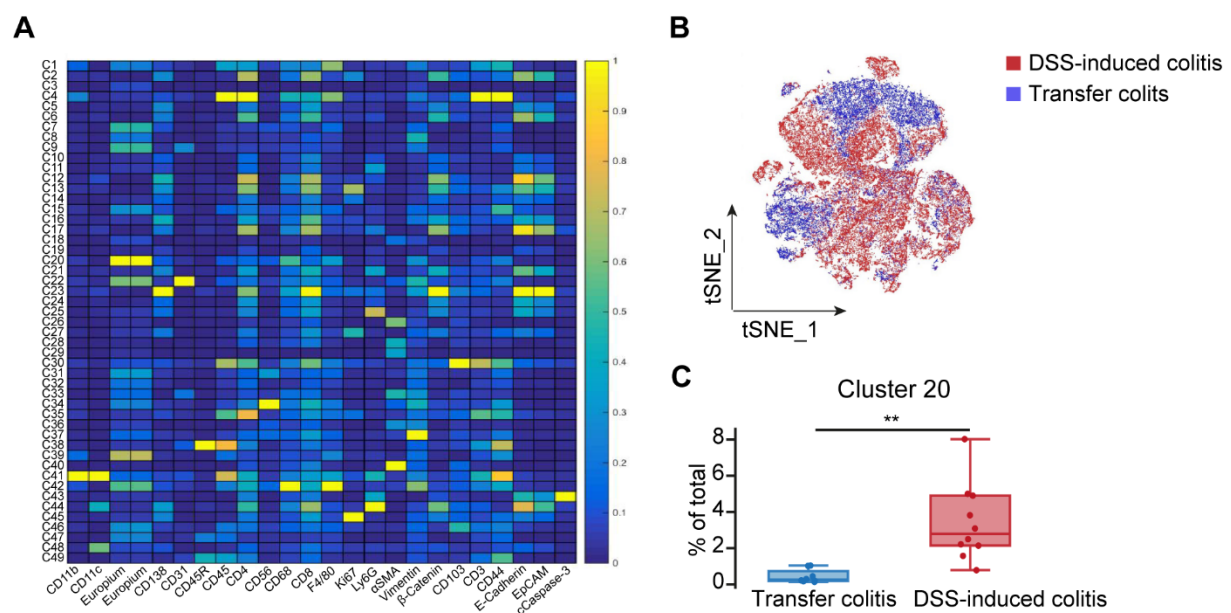
Figure 4-13: DSS-induced colitis incurs significantly higher numbers VSOP-positive $CD44^+$ macrophages. Heat map summarizes unsupervised Phenograph analysis which resulted in a total of 49 clusters with mean marker expression (dark blue refers to low expression and yellow refers to high expression) of DSS-induced colitis and transfer colitis IMC data **(A)**. The overlaid tSNE plot of DSS-induced colitis samples (red) and transfer colitis (blue) visualizes different cluster distribution depending on mouse model **(B)**. In cluster 20, the cell cluster that showed the most prominent VSOP accumulation, the frequency of cells (relative to total number of cells) was significantly higher (*p* = 0.0005) in the DSS-induced colitis group (n = 11) when compared to the transfer colitis group (n = 8) **(C)**. Statistical significance was tested with Student's *t*-test and marked with * if *p* ≤ 0.05. Data is represented as mean

± SD. Figure and data were adapted from Golusda *et al.* 2022.

Immunofluorescence staining of colon tissue sections from DSS-induced colitis and transfer colitis mice was used to validate the above presented results. For this, colon tissue sections were stained with anti-CD44 and anti-F4/80 and analyzed with the Vectra 3 automated quantitative pathology imaging system (Akoya Bioscience). However, no difference in quantity of F4/80$^+$ macrophages expressing CD44 was detectable in DSS-induced colitis compared to uninflamed tissue from healthy control animals (**Figure 4-14, A**). The same was true for colon tissue from transfer colitis mice (**Figure 4-14, B**). Furthermore, the amount of F4/80$^+$ macrophages expressing CD44 did not differ between models.
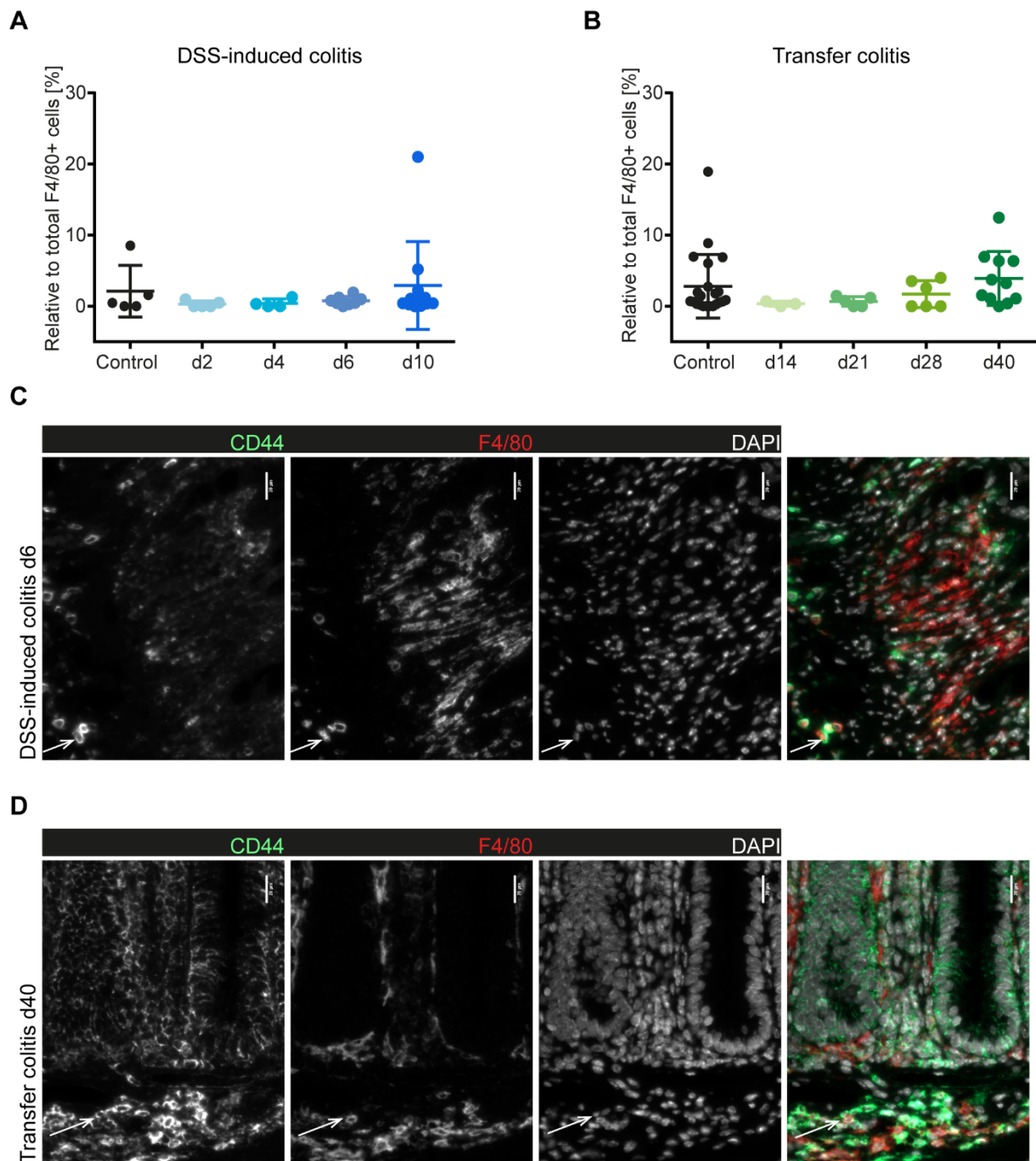
Figure 4-14: <u>Proportion of CD44⁺ macrophages analyzed with immunofluorescence is similar in colon tissue of DSS-induced colitis and transfer colitis.</u> Quantification of F4/80⁺ and CD44⁺ double positive relative to total amount of F4/80⁺ cells summarized for each time point with mean ± SD in DSS-induced colitis **(A)** and transfer colitis **(B)** mice whereby each dot represents one mouse. Level of CD44⁺ macrophages in colon tissue sections is comparable between both models. No statistical significant difference compared to healthy control animals was observed with Mann-Whitney test (non-parametric *U*-test). Representative immunofluorescence images of severe inflammation in DSS-induced colitis **(C)** and transfer colitis **(D)** animals with white arrows indicating a F4/80⁺ macrophage expressing CD44. CD44 in green, F/80 in red, DAPI in white in merged image. Scale bar equals 20 µm.

4.7 Long-term effects of VSOPs on the intestinal immune system

To assess the influence of VSOPs on the intestinal immune system, transfer colitis mice were injected with VSOPs, and mesenteric lymph nodes (mLN) were isolated 7 (d7), 10 (d10) and 18 days (d18) after VSOP injection. **Figure 3-1,B** summarizes the experimental design. Cells were characterized by single cell mass cytometry time of flight (CyTOF) and compared to transfer colitis mice that did not receive VSOPs (w/o VSOP). For clean analysis, cells were pre-gated on CD45$^+$ cells in Cytobank. With a set of 16 markers used to define cell types, samples underwent unsupervised clustering with *FlowSome* clustering and *ConsensusClusterPlus* metaclustering as described in Nowicka *et al.* 2017.

Using this algorithm, 10 sub clusters were identified based on their marker profile (**Figure 4-15, A-B**). Dimensional reduction of all 36 samples is represented in Uniform Manifold Approximation and Projection (UMAP) format **(Figure 4-15, A)**. Mean expression of the 16 markers used for clustering is summarized in a heat map to underline cluster assignment. The most important clusters for this study were the following: Cluster 1 (red) with Ly6C$^+$CD11b$^+$CD163$^+$ monocytes, Cluster 6 (light purple) CD11b$^+$CCR2$^+$CX$_3$CR1$^+$CD64$^+$ macrophages, Cluster 7 (orange) CD11c$^+$CD11b^{low}CD64^{low}MHCII$^+$CCR2$^+$CX$_3$CR1$^+$ monocyte-derived DCs, Cluster 8 (light orange) CD11b$^+$CD103$^+$MHCII^{++} DCs and Cluster 2 (salmon) CD3$^+$CX$_3$CR1$^+$ T cells (**Figure 4-15, B**). A UMAP representing expression of CD45 highlights the presence of lymphoid cells in the described analysis (**Figure 4-15, C**), while expression (dark blue refers to low expression and yellow to high expression) of cell type markers allows cluster annotation of monocytes (Ly6C, CD11b), macrophages (CD11b), DCs (CD11c) and T cells (CD3, CD8a) (**Figure 4-15, D-H**).

The influence of VSOP injection on these cell populations within the mLN was evaluated for each time point comparing animals injected with VSOPs (w/ VSOP) with the control group not receiving VSOPs (w/o VSOP). Each cell population of 10 sub clusters was analyzed for their abundance and no difference for all 10 sub clusters was found. Since cells from the mononuclear phagocyte system have a high phagocytic activity, they are most likely to interact with VSOPs. Therefore, the monocyte, macrophage and two DCs cluster abundances are shown (**Figure 4-16**). Additionally, the CD3$^+$ T cell cluster is shown as this cluster represents up to 60 % of all analyzed events (**Figure 4-16**). UMAPs of samples from animals sacrificed at d7 after injection were comparable in appearance (**Figure 4-16, A & B**). Further, cluster abundance for the represented clusters of animals w/ VOSP was not significantly different when compared to animals w/o VSOP (**Figure 4-16, C**). The same is true for d10 (**Figure 4-16, D-F**) and d18 (**Figure 4-16, G-I**) animals. This indicates no significant influence of VSOPs on cell population abundance in mesenteric lymph nodes.
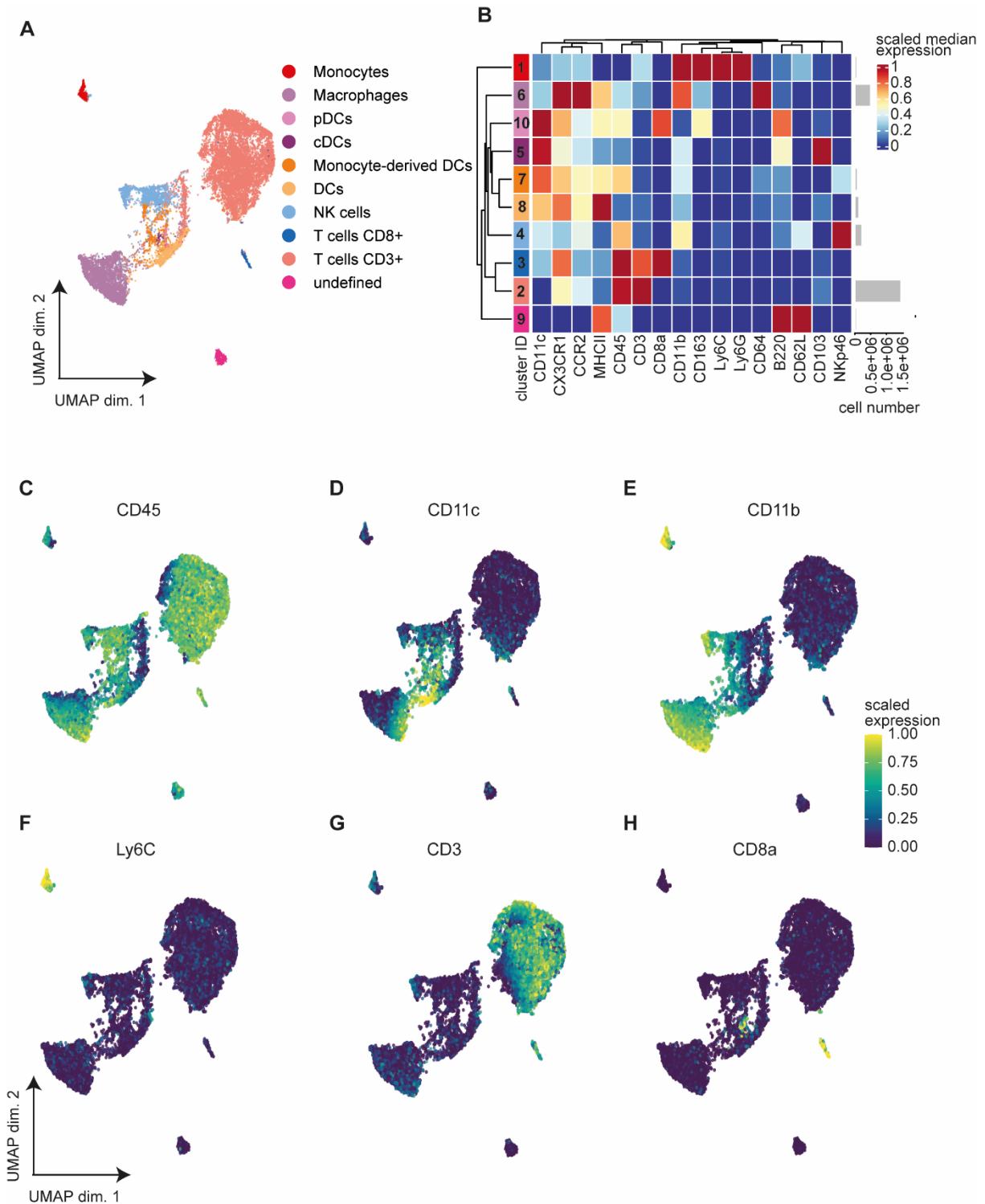
Figure 4-15: <u>Cluster identification of cells from mesenteric lymph nodes.</u> Unsupervised clustering and dimensional reduction of pre-gated CD45⁺ cells visualized in Uniform Manifold Approximation and Projection (UMAP) with colors referring to 10 sub clusters **(A)**. Sub clusters were identified using a marker set of 16 markers and their expression summarized in a heat map (red = high expression, blue = low expression) **(B)**. UMAPs representing marker expression with dark blue referring to low expression and yellow to high expression for CD45 **(C)**, DC11c **(D)**, CD11b **(E)**, Ly6C **(F)**, CD3 **(G)** and CD8a **(H).**
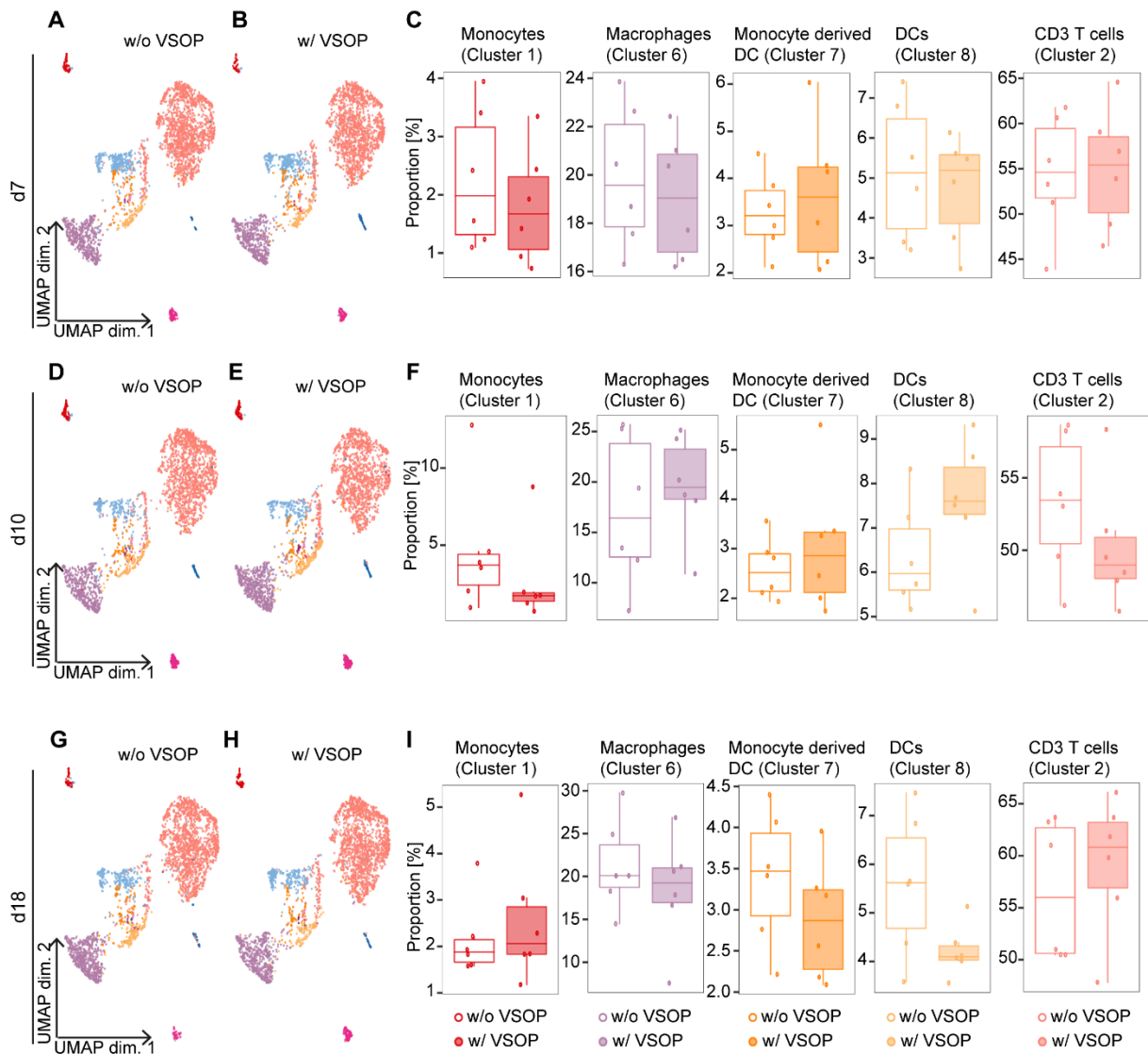
Figure 4-16: <u>VSOP injection did not influence cell cluster abundance in mesenteric lymph nodes following long-term exposure.</u> UMAP at d7 post VSOP injection w/o VSOP **(A)** and w/ VSOP **(B)** appear identical and cluster abundance for chosen clusters shows no significant difference **(C)**. UMAPs at d10 post-VSOP injection w/o VOSP **(D)** or w/ VSOP **(E)** appear identical and cluster abundance for chosen cluster shows no significant difference **(F)**. UMAP at d18 post VSOP injection for control **(G)** and injected **(H)** animals appear identical and cluster abundance for chosen cluster show no significant difference **(I)**. Statistical significance was tested with R package *diffcyt* for differential abundance (DA) with $p_{adjust} \leq$ 0.05 defining statistical significance. Data is represented as mean ± SD. DCs = dendritic cells

Further liver, colon, cecum, and small intestinal tissue sections of animals exposed to VSOPs were pathologically evaluated for inflammation and compared to control animals. No difference in inflammation levels was observed between VSOP-exposed animals and controls (**Figure 4-17, A-C**).
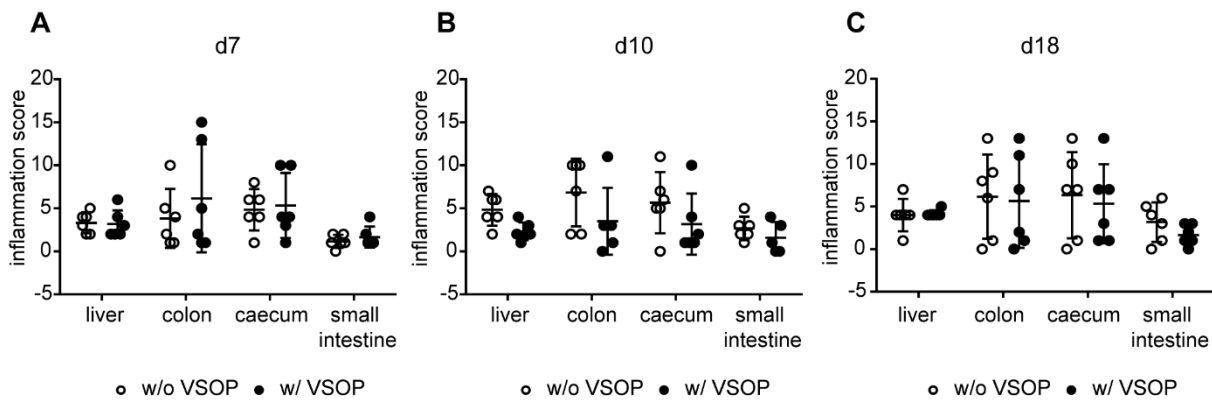
Figure 4-17: <u>Injection of VSOPs does not enhance tissue inflammation.</u> Scoring of liver, colon, cecum and small intestinal tissue sections of transfer colitis mice injected with VSOPs (w/ VSOP) and transfer colitis animals not injected with VSOP (w/o VSOP) at 7 days (d7, **A**), 10 days (d10, **B**) and 18 days (d18, **C**) after VSOP-injection. No difference was detected in inflammation score of all tissues when compared to control group. Statistical significance was tested Mann-Whitney test (non-parametric *U*-test), no significance was determined. Data is represented as mean ± SD.

4.8 Monocytes are the main cell type responsible for VSOP uptake and do not change their phenotype upon uptake

As the overall goal is to use VSOPs as a contrast agent in human, *in vitro* experiments were done to further investigate the effect of VSOPs on immune cell phenotype. In a preliminary CyTOF experiment, VSOPs were incubated with human whole blood from healthy donors in order to measure which immune cell types preferentially take up VSOPs in the periphery. Here, human whole blood was incubated with VSOPs for 30 minutes and then analyzed with CyTOF.

This showed successful uptake of VSOPs by 2.56% of CD45$^+$ cells (**Figure 4-18, A**). Basic characterization of cell types within the sample showed uptake by CD16$^+$, CD45^{low} granulocytes (1.69%) (**Figure 4-18, B**), CD45$^+$CD19$^+$ B cells (1.53%) (**Figure 4-18, C**), CD45$^+$CD3$^+$ T cells (1.96%) (**Figure 4-18, D**) and CD45$^+$CD19$^-$CD3$^-$CD16$^+$ natural killer (NK) cells (4.04%) (**Figure 4-18, E**). Nevertheless, CD45$^+$, CD3$^-$, CD19$^-$, CD14$^+$ monocytes were the main cells taking up VSOPs (15.6%) (**Figure 4-18, F**).
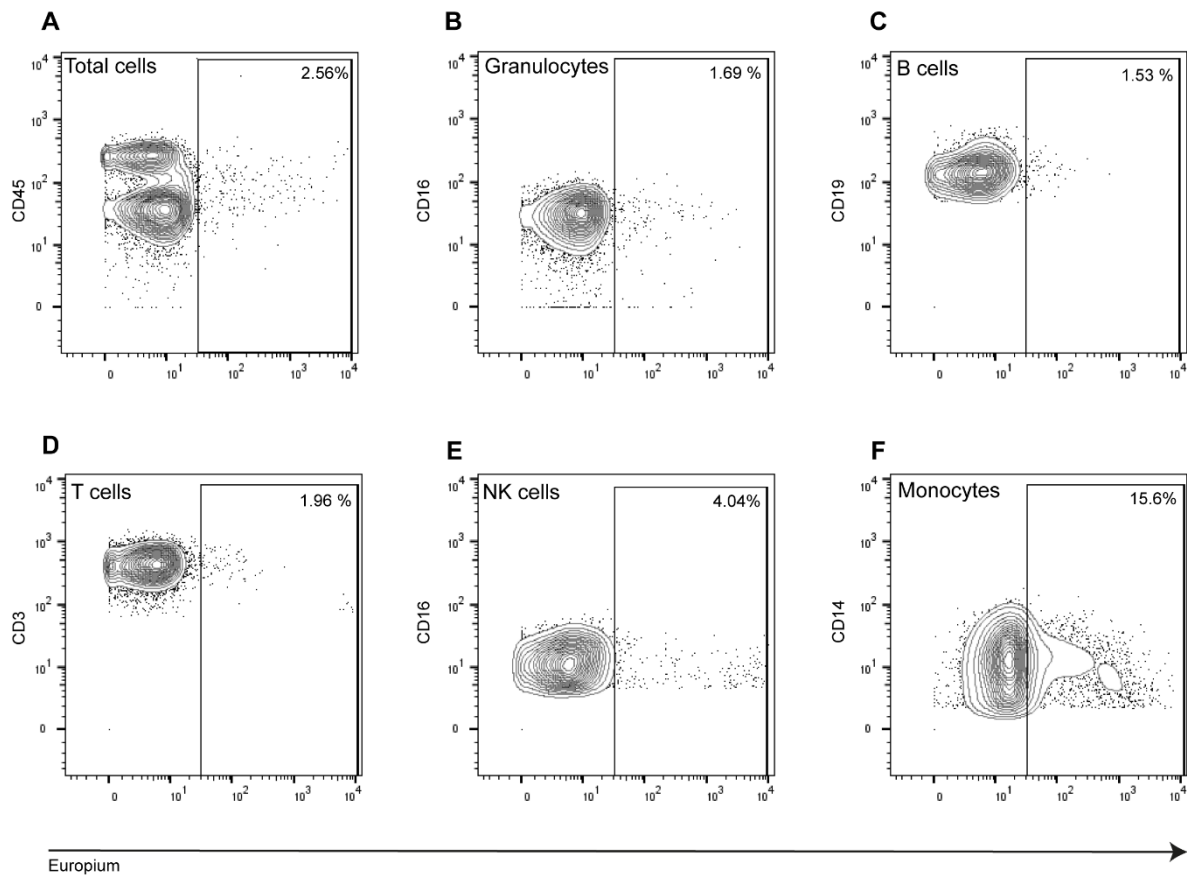
Figure 4-18: <u>VSOPs are taken up mainly by monocytes following *in-vitro* incubation in whole blood samples.</u> Analysis of CyTOF measurement of VSOP incubated human whole blood, revealed that 2.43% of total single $CD45^+$ cells were positive for VSOPs **(A)**. 1.69% of granulocytes ($CD45^{low}$, $CD16^+$) **(B)**, 1.53% of B cells ($CD45^+$, $CD19^+$) **(C)**, 1.96% of T cells ($CD45^+$, $CD3^+$) **(D)**, 4.04% of NK cells ($CD45^+$, $CD3^-$, $CD19^-$) **(E)** and 15.6% of monocytes ($CD45^+$, $CD3^-$, $CD19^-$. $CD14^+$) were positive for VSOPs **(F)**. Cells were gated on DNA^+ cells, then single cells.

Since monocytes were the main cell type which internalized VSOPs, RNA sequencing of human $CD14^+$ monocytes was done to investigate whether VSOP uptake affects gene expression. Measurements of *in vitro* cultured and VSOP treated monocytes showed successful uptake of VSOPs after 30 minutes whereby the concentration within cells increased with incubation time (**Figure 4-19**). As measurable levels of VSOPs were successfully taken up after 30 minutes, this time point was chosen for first RNA-sequencing experiments.
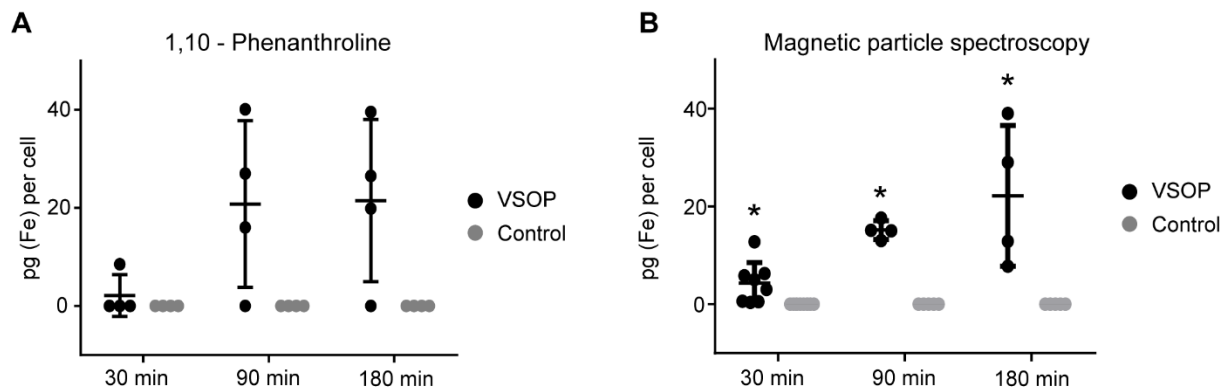
Figure 4-19: <u>Monocytes take up VSOPs within 30 minutes.</u> Monocytes were treated with VSOPs (black) *in vitro* for 30, 90 and 180 minutes. Control samples were not treated with VSOPs (grey). Iron content was measured using 1,10-phenanthroline **(A)** and magnetic particle spectroscopy (MPS) **(B)**. 1,10-phenanthroline measurement varied strongly between samples and iron content per cell was not significantly different compared to control. Iron quantification with MPS showed significant uptake after 30 minutes ($p \leq 0.0001$), 90 minutes ($p = 0.0079$) and 180 minutes ($p = 0.0079$) treatment when compared to untreated controls and an exposure time dependent increase in VSOP concentration. Statistical significance was tested with Mann-Whitney test (non-parametric *U*-test) and marked with * if $p \leq 0.05$.

Monocytes isolated from whole blood from three healthy donors were stimulated with VSOPs for 30 minutes *in vitro*. Validation of bulk RNA-sequencing data revealed no major up- or downregulation of genes (**Figure 4-20, A**). Most significantly, the gene encoding for cell surface transferrin receptor (*Tfrc*) was downregulated upon VSOP treatment indicating increased levels of cellular iron and cells respond by restricting further iron uptake (**Figure 4-20, A & C**). Principal component analysis of RNA showed higher variation between donors. Here, VSOP-incubated versus untreated cells did not cluster together, further indicating no major gene-expression changes upon VSOP treatment (**Figure 4-20, B**). Deeper insight into genes listed in the gene ontology terms showed repetitive appearance of specific genes. All those genes of interest that were up-regulated or down-regulated by at least one-fold were filtered out of RNA-sequencing data and are summarized in **Figure 4-20, C**.
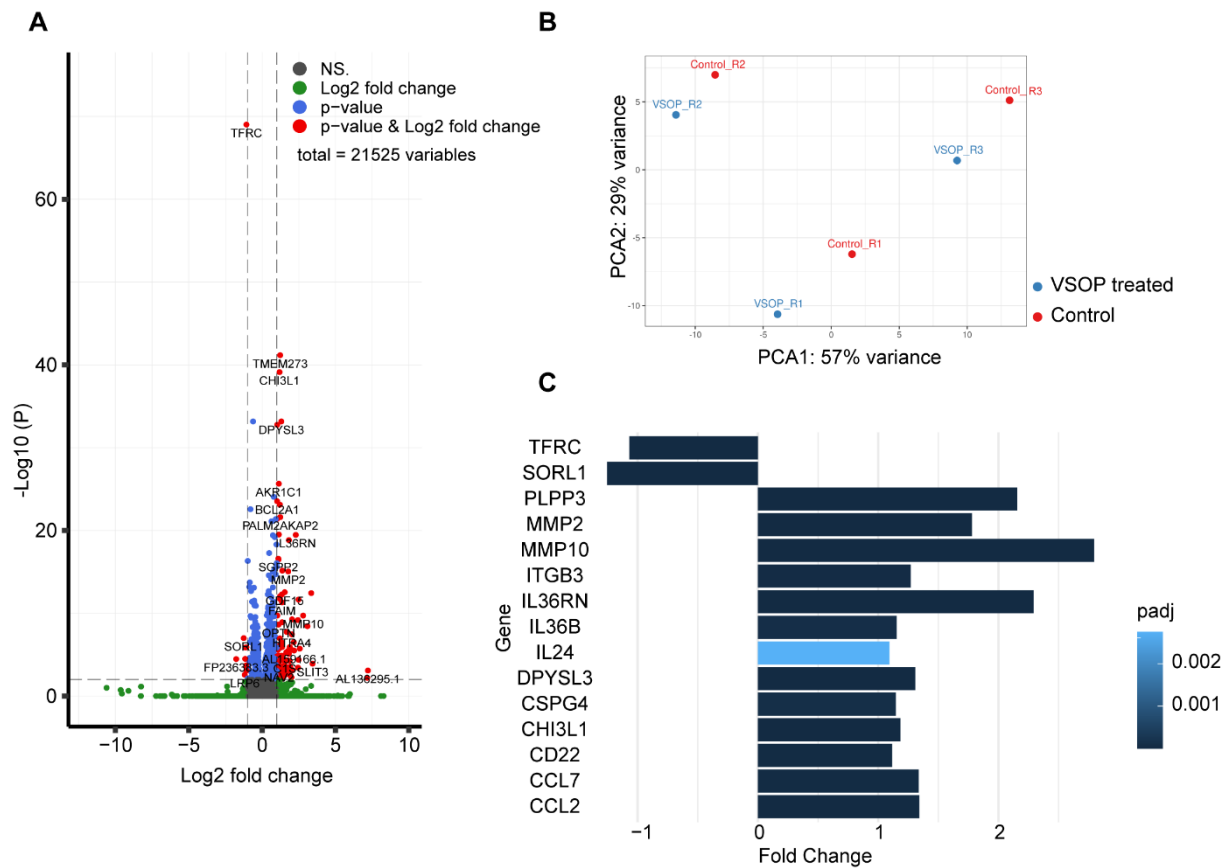
Figure 4-20: <u>VSOPs do not induce major changes in gene expression profile of monocytes.</u> Bulk RNA-sequencing of *in vitro* VSOP-treated CD14$^+$ monocytes and unstimulated control samples found no significantly up- or down-regulated genes in enhanced volcano plot **(A)**. Principal component analysis underlined no major differences between VSOP incubated and untreated controls as samples clustered by donor instead of treatment **(B)**. Summarized genes of interest that were most prominently up- or down-regulated upon VSOP-treatment. Color scale refers to p_{adjust} value, while dark blue represents $p_{adjust} < 0.001$ and light blue represents $p_{adjust} > 0.002$ **(C)**.

For better insight into the influence of VSOP concentration and incubation time on monocyte phenotype, monocytes were stimulated *in vitro* with either 0.5, 0.75 or 1 mM of VSOPs for 30 or 90 minutes and analyzed by flow cytometry 24h and 48h after VSOP treatment. In flow cytometry analysis, the gates were set to macrophages, single and living cells. In addition, the relative amount of CD14^{++}CD16$^-$ classical monocytes (cMon) and CD14^{++}CD16$^+$ intermediate (iMon) together with CD14$^+$CD16$^+$ non-classical monocytes (ncMon) was determined (**Figure 4-21, A**).

Treatment of monocytes for 30 minutes did not affect survival of cells within the following 24h or 48h when compared to controls (**Figure 4-21, B**). Further, the abundance of cMon and iMon/ncMon was not influenced by 30 minutes of VSOP treatment (**Figure 4-21; C, D**). Treatment of cells for 90 minutes also did not affect cell survival (**Figure 4-21, E**). The abundance of cMon slightly increased with higher concentration of VSOPs 24h after treatment,

but returned to control levels after 48h. Consequently, the abundance of iMon/ncMon was slightly lower with higher VSOP concentrations. Nevertheless, relative proportions returned to control levels 48h after 90 minutes of VSOP treatment. Both cell populations were evaluated for chemokine receptor type 2 (CCR2), CD206, human leucocyte antigen receptor (HLA-DR) and CD86 expression for deeper insight into cell phenotype. The only prominent effect was seen in the significantly higher proportion of CCR2$^-$CD206$^+$ cells in cMon after 48h with 90 minutes of VSOP treatment (**Figure 4-21, H**). Additionally, a significantly higher presence of HLA-DR$^+$CD86$^+$ cells was detected in cMon population when treated for 90 minutes with 0.75 mM and 1 mM VSOPs, respectively (**Figure 4-21, I**).
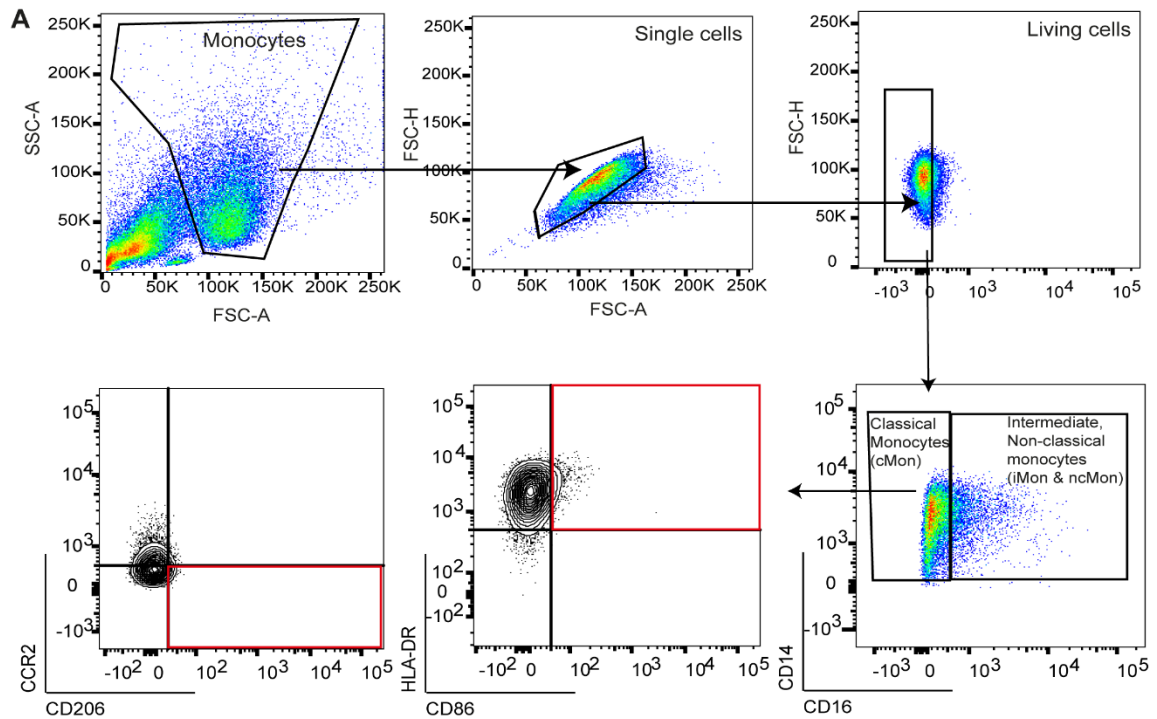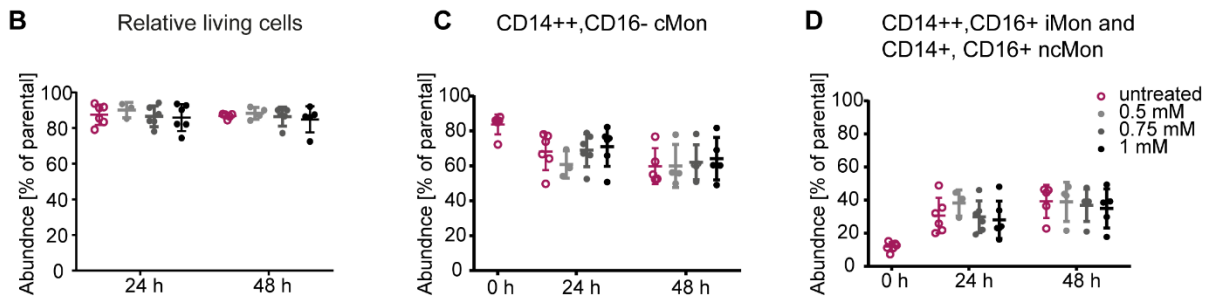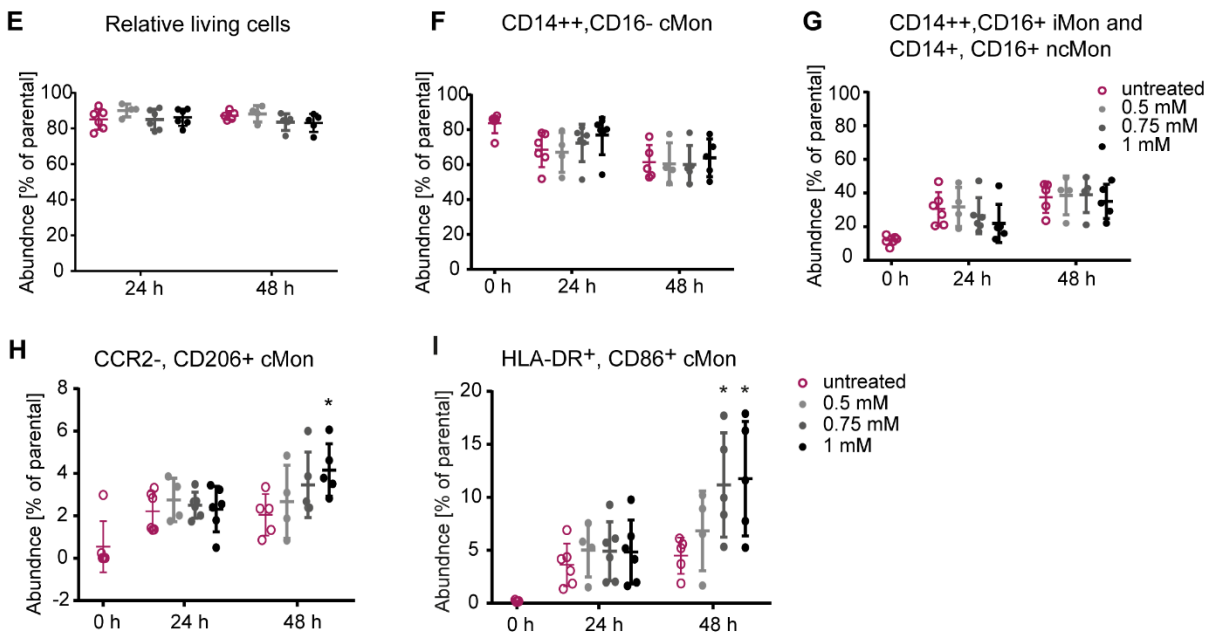
Figure 4-21: VSOP treatment does not influence cell viability and has minor effects on protein expression of CD14++CD16- classical monocytes. Gating was done to restrict the analysis to living,

single monocytes and differentiate between CD14^{++}CD16$^-$ classical monocytes (cMon) and CD14^{++}CD16$^+$ intermediate (iMon) / CD14$^+$CD16$^+$ non-classical monocytes (ncMon), whereby cMon were further analyzed for HLA-DR$^+$CD86$^+$ and CCR2$^-$CD206$^+$ expression **(A)**. 30 minutes stimulation of monocytes with 0.5 mM, 0.75 mM and 1 mM of VSOPs has no effect on cell survival **(B)**. Abundance of CD14$^+$CD16$^-$ cMon **(C)** and CD14^{++}CD16$^+$ iMon / CD14$^+$CD16$^+$ ncMon **(D)** 24h and 48h after 30 minutes of VSOP treatment did not change. 90 minutes stimulation of monocytes with VSOPs has no effect on cell survival **(E)**. The abundance of CD14$^+$CD16$^-$ cMon is slightly increased after 24h of stimulation with 1 mM of VSOPs when compared to control but back to control level after 48h **(F)**. The abundance of CD14^{++}CD16$^+$ iMon and CD14$^+$CD16$^+$ ncMon tends to be lower 24h after VSOP treatment and is back to control levels 48h after stimulation **(G)**. Within cMon a significant increase in CCR2$^-$, CD206$^+$ expression with 90 minutes of 1 mM (p=0.0176) VSOP treatment **(H)** and significant increase in HLA-DR+, CD86+ expression 90 minutes of 0.75 mM (p = 0.0119) and 1 mM (p = 0.0059) VSOP treatment **(I)**. Significance was tested in reference to untreated group with one-way ANOVA and marked with * if $p \leq 0.05$. Data is represented as mean ± SD.

From the same culture, the cytokine concentration in cell culture supernatant was evaluated by a cytometric bead array (CBA) at 24h after a 30 or 90 minute VSOP treatment. The most relevant changes are displayed in **Figure 4-17**. All cytokine concentrations are represented relative to the respective concentration in samples of untreated monocytes since high interindividual differences between donors were detected. TNFα decreased slightly but non-significantly in the supernatant of cells that were treated for 90 minutes with VSOPs, independent of concentration. Whereas, 30 minutes treatment did not influence TNFα production (**Figure 4-22, A**). Interleukin 1 receptor antagonist (IL-1 RA) concentration showed a statistically significant increase after 90 minutes treatment with either 0.75 mM or 1 mM VSOPs (**Figure 4-22, B**). Interleukin 1 β (IL-1β) significantly decreased after 30 minutes treatment with all VSOP concentrations. However, with 1 mM VSOP IL-1 β was slightly higher. Treatment for 90 minutes did not have any effect on IL-1β concentration (**Figure 4-22, C**). IL-10 content slightly increased with longer treatment time and concentration but was not statistically significant when compared to control (**Figure 4-22, D**).
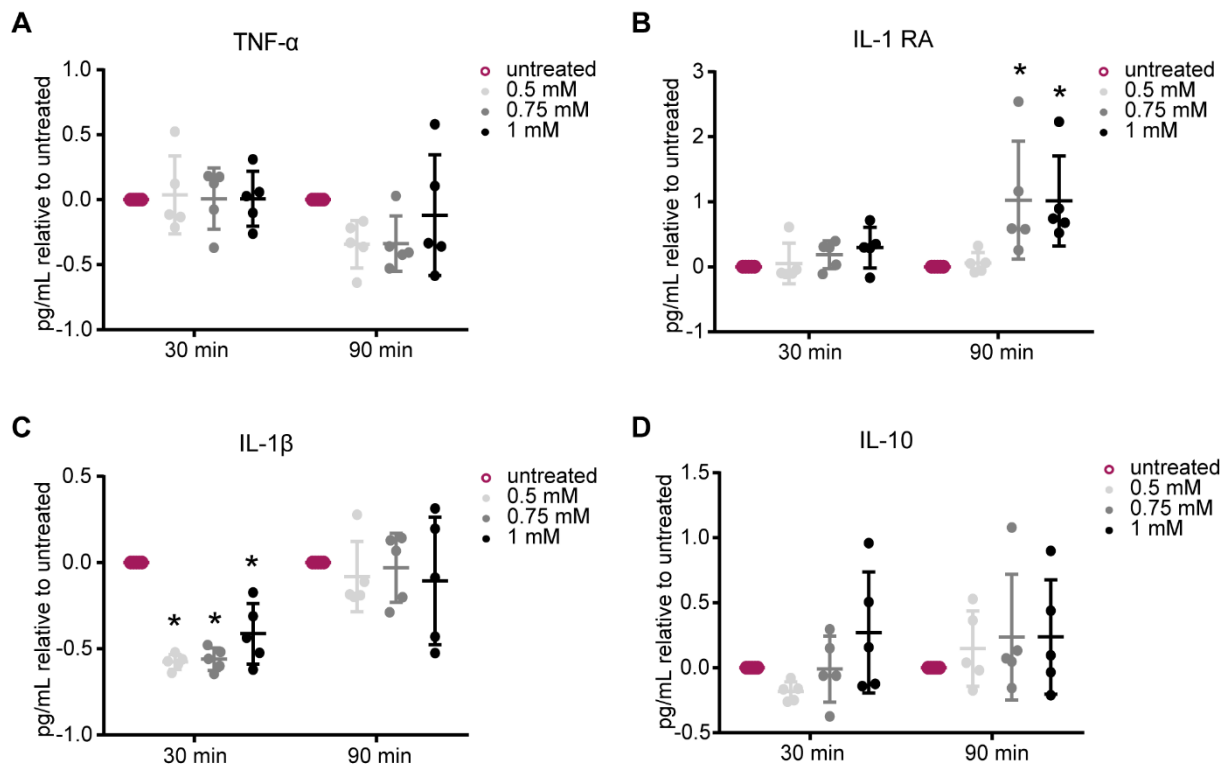
Figure 4-22 VSOP treatment partially influences cytokine production of monocytes *in vitro.* Supernatant of macrophages stimulated with VSOP for 30 minutes or 90 minutes and at different concentrations was collected 24h after stimulation and different cytokines were quantified in the cell culture supernatant with a cytometric bead array. TNFα showed a non-significant tendency to decrease following 90 minutes stimulation **(A)**. IL-1RA increased significantly with 0.75 mM ($p = 0.0026$) and 1 mM ($p = 0.0029$) when stimulated for 90 minutes **(B)**. IL-1β significantly decreased with 0.5 mM ($p < 0.0001$), 0.75 mM ($p < 0.0001$) and 1 mM ($p = 0.0026$) stimulation for 30 minutes **(C)**. IL-10 showed a slight but not significant increase **(D)**. Significance was tested relative to untreated groups with one-way ANOVA and with $p \leq 0.05$ defining the statistical significance that is marked with *. Data is represented with mean ± SD.

5   DISCUSSION

In IBD, the initial diagnosis and surveillance during disease course and treatment is done by a combination of endoscopy, colonoscopy, pathology, ultrasound, and magnetic resonance imaging (MRI), whereby endoscopy and colonoscopy are still considered the gold standard in the clinic (Gomollon et al. 2017, Magro et al. 2017). Despite its prevalent use, this procedure is very invasive and often requires anesthesia, which carries additional risks to the patients. MRI, however, is a non-invasive technique and may thus be a good alternative to endoscopy and colonoscopy. Furthermore, MRI provides additional advantages including circumventing the need for anesthesia and, if desired, providing information about surrounding tissues and organs (Deepak et al. 2019). However, most MRI examinations of intestinal tissue require the administration of a contrast agent. Up to today, gadolinium-based contrast agents (GBCAs) are most commonly used for these examinations, but recent findings question the safety of GBCAs (Pasquini et al. 2018, Kanda et al. 2014, Flood et al. 2017, Wang et al. 2019, White et al. 2006).

Thus, there is a need for a less invasive alternative to endoscopy and colonoscopy requiring a safer contrast agent. This study investigated an iron oxide-based contrast agent as an alternative to GBCAs. Here, the very small superparamagnetic iron oxide nanoparticles (VSOPs) were used to detect intestinal inflammation in various mouse models of intestinal inflammation. These results indicate that VSOPs accumulate in the inflamed colon of DSS-induced colitis mice and induced an iron oxide-dependent signal decrease in T2*w MR images, thus allowing visualization of tissue inflammation in MRI. Interestingly, MRI examinations of colons from transfer colitis mice and ileum from $TNF^{\Delta ARE}$ mice did not detect the inflammation in the intestinal tissue of those models. Further results suggest that accumulation of VSOPs might be dependent on the hyaluronic acid (HA) content in the inflamed intestinal tissue as HA was strongly upregulated in DSS-induced colitis, but not in the other two models of intestinal inflammation. Moreover, CD44-expressing macrophages containing VSOPs might contribute to accumulation of VSOPs into colon tissue due to their CD44-HA interaction in the inflamed tissue.

Additional experiments investigating the safety and biocompatibility of VSOPs in mice as well as *in vitro* with primary human monocytes showed no major effect of VSOPs on immune cell signatures. Given this, VSOPs might serve as an alternative to GBCAs in detecting specific tissue changes in early-onset intestinal inflammation. In the following sections the results presented above will be discussed and future directions will be presented.

5.1 VSOP-enhanced magnetic resonance imaging in mouse models of intestinal inflammation

Intestinal inflammation was aimed to be detected with MRI 90 minutes after intravenous (i.v.) VSOP injection in three models of intestinal inflammation. On the one hand, VSOP-induced signal decrease in T2*w MRI examinations of colons in DSS-induced colitis mice was successful (**Figure 4-4**). On the other hand, the examination of colons in transfer colitis mice and ilea of $TNF^{\Delta ARE}$ mice was not able to detect inflammation (**Figure 4-5, Figure 4-6**). In the DSS-induced colitis mouse model the DSS is added to the drinking water. DSS is highly aggressive to the epithelial barrier, consequently inducing a barrier breach. As a consequence, bacteria are able to infiltrate the intestinal mucosa and induce inflammation. First, this occurs distally due to a higher bacterial burden in the distal colon. With longer exposure to DSS, the inflammatory process appears more proximal as well (Dieleman et al. 1998). The MRI examinations in this study underlined this effect. Here, VSOP accumulated in the distal colon at early time points, while VSOP additionally accumulated in the proximal colon only at later time points (**Figure 4-4, G**). Nevertheless, the observed VSOP accumulation might represent the effect of a leaky barrier induced by DSS. Apart from rupturing the epithelial barrier, DSS further has the property to act as an anticoagulant and provoke intestinal bleeding (Chassaing et al. 2014). Therefore, the VSOPs might not only reside in the intestinal vasculature, like they most probably did in transfer colitis and $TNF^{\Delta ARE}$ mice, but further flood the lumen of the colon. That could have led to the higher amount of VSOPs in the colon area that induced a detectable signal decrease in MR images of DSS-induced colitis mice. Nevertheless, this DSS-induced pathological effect mirrors those seen in IBD patients, especially in UC patients, where defects within the epithelial barrier and consecutive hematochezia are well-described symptoms in the pathogenesis of IBD (Eichele and Kharbanda 2017). Given these similarities of human IBD phenotypes with DSS-induced colitis mice, the applicability of VSOPs in patients with defects in epithelial barrier is promising.

Several studies applied MRI examinations to small animal models of colitis to investigate epithelial leakage, colon wall thickness and edema (Frericks et al. 2011, Michael et al. 2013, Breynaert et al. 2013, Melgar et al. 2007, Larsson et al. 2006, Mustafi et al. 2010, Pohlmann et al. 2009). Michael *et al*. were able to successfully correlate various *in vivo* MRI parameters to *ex vivo* parameters. For example, colon wall thickness significantly correlated with the histological inflammation score and spleen and mesenteric lymph node volume correlated significantly with the *ex vivo* measured weight of organs. Thus, they suggested MRI as a valid tool to grade inflammation in IL-10-deficient mice exposed to DSS (Michael et al. 2013). Furthermore, some studies applied Gd-diethyltriaminepentaacetic acid or M-Gadofluorine

enhancement in MRI that allows distinction between normal and inflamed colon tissue (Frericks et al. 2011, Mustafi et al. 2010).

Despite these advances, most of the mentioned studies focus on MRI as a monitoring tool during experimental colitis and lack the translation to a patient and clinical set-up. Further, all of the above-mentioned studies only use the DSS-induced colitis as a model system and did not test their findings in any additional model of intestinal inflammation. In addition, limiting the assessment of intestinal inflammation to the measurement of bowel wall thickness might not be sufficient in a clinical set-up as a thickening in bowel wall is more likely to be overlooked than contrast changes in MR images. Therefore, the additional use of an adequate contrast agent is crucial to ensure accurate examination.

VSOPs showed sufficient detection of inflammation in the colon in T2*w MRI already after only 2 and 4 days of DSS exposure (**Figure 4-4**), underlining the sensitivity of VSOP-enhanced MRI in detecting early-onset inflammatory changes in colon tissues where pathological scoring of H&E-stained sections was inconspicuous for both time points (**Figure 4-7, A-D**). This emphasizes the sensitivity of VSOPs to early-onset intestinal tissue changes prior to the detection of classically defined pathological changes like inflammatory cell infiltrations, erosions, and ulcerations (Erben et al. 2014). Importantly, VSOP accumulation is not visually detectable or quantifiable in any of the healthy controls (**Figure 4-4**).

The lack of a T2 effect in transfer colitis colon tissue (**Figure 4-5**) and $TNF^{\Delta ARE}$ ileal tissue (**Figure 4-6**) requires further validation as both models presented with pronounced histopathological inflammation (**Figure 4-7; E-L**). A longer incubation time of VSOPs might improve MRI examination as 90 minutes after i.v. injection is relatively short compared to other studies where MRI examination were performed up to 24h after VSOP administration (Millward et al. 2013, Silva et al. 2021, Wagner et al. 2013, Millward et al. 2019).

5.2 Hyaluronic acid supports accumulation of VSOPs

Colon tissue at early time points in DSS-induced colitis and transfer colitis mouse models were histopathologically evaluated as uninflamed (score 0). Thus, no remarkable tissue changes such as increased inflammatory cell infiltration, erosions or ulcerations and crypt hyperplasia were observed (**Figure 4-4, A, C, E, G**). At later time points all three mouse models showed an increase in their pathological inflammation score (**Figure 4-4, A, E, I**). As suggested in paragraph **5.1** the VSOP-induced T2 contrast throughout the whole disease course of DSS-induced colitis might occur independent of standard pathological indications. In an *in vitro* study done by Ludwig *et al*. cells from a human acute monocyte leukemia cell line (THP-1), that are known to produce high amounts of proteoglycans, were exposed to VSOPs for either 4h or 24h. Transmission electron micrographs revealed that apart from incorporation into

intracellular vesicles, VSOPs further aggregated on the cell surface. By inhibiting glycosaminoglycan synthesis or enzymatic digestion of chondroitin sulfate (CS) of THP-1 cells *in vitro*, a significant lower uptake of VSOPs was reported, concluding the pivotal role of GAGs in the binding of VSOPs to cells (Ludwig et al. 2013). Additionally, during inflammation in an experimental autoimmune encephalomyelitis mouse model VSOPs were found to bind to inflamed brain endothelium suggesting a sensitivity to inflammation (Berndt et al. 2017). Further *in vitro* experiments with brain endothelial cells showed significantly lower uptake of VSOPs after enzymatic degradation of hyaluronic acid (HA), heparin sulfate and CS. This underlines the importance of GAGs in VSOP uptake (Berndt et al. 2017).

Therefore, this work investigated the two ECM components HA and chondroitin sulfate proteoglycan 4 (CSPG4) in colon and ileum by immunohistochemistry. Immunohistochemistry revealed a significant change in the abundance of HA and CSPG4 during the disease course, and showed that HA and CSPG4 contents differ between the investigated mouse models (**Figure 4-10**). In DSS-induced colitis, HA content increased during the disease course (**Figure 4-10, A-D**), whereas it did not change throughout the transfer colitis disease course (**Figure 4-10, E-H**) and was dynamic in the ileum during disease course of $TNF^{\Delta ARE}$ mice (**Figure 4-10, I-L**). The CSPG4 content decreased in DSS-induced colitis (**Figure 4-10, A-D**), whereas it increased in transfer colitis (**Figure 4-10, E-H**) and did not change in the $TNF^{\Delta ARE}$ model (**Figure 4-10, I-L**). As these changes align with the finding that VSOPs accumulate only in DSS-induces colitis colon tissues this suggests that increased HA in the inflamed tissue promotes VSOP accumulation that induces a detectable T2 contrast in MRI examinations. Since in the transfer colitis colon tissue the HA content did not increase, VSOPs were not able to accumulate in detectable amounts. Strikingly, although the HA amount in the ileum of $TNF^{\Delta ARE}$ mice is comparable to the one in DSS-induced colitis, VSOPs still did not accumulate. However, the distribution of HA within the colon tissue of DSS-induced colitis was different compared to the HA distribution in the ileum of $TNF^{\Delta ARE}$ mice. In DSS-induced colitis the HA content increased in mucosa and submucosa but appeared organized, while HA in the ileum of $TNF^{\Delta ARE}$ mice is limited to the mucosa and further seemed more dispersed throughout the whole mucosa (**Figure 4-10, D,K,L**). This possibly could have led to a different distribution of VSOPs in the tissue which was insufficient to induce a T2 contrast in the MRI examinations of $TNF^{\Delta ARE}$ mice.

HA synthesis during the disease course of DSS-induced colitis was previously reported to be altered in colon tissue (Kessler et al. 2008, Kessler et al. 2015), and this is in line with the herein reported findings with increasing HA content measured by HPLC (**Figure 4-9, A**) and immunohistochemistry (**Figure 4-10, A**). Deposition of excessive HA in tissues can contribute to inflammatory processes while knockout of *Has3*, the gene encoding the hyaluronan

synthase 3 (HYAS3), that is a crucial enzyme in HA synthesis, was reported to protect mice from DSS-induced colitis (Kessler et al. 2015, Hundhausen et al. 2021). For additional validation of HA involvement in VSOP accumulation, a DSS-induced colitis experiment with *Has3* knockout mice and subsequent VSOP-enhanced MRI examination might be of interest. It should be kept in mind that HA synthesis can be compensated by HYAS1 and HYAS2 and complete knock out of all enzymes responsible for HA synthesis is likely lethal. Taken together, HA is an interesting target to assess intestinal inflammation as increased HA deposition is reported in IBD patients as well (Derkacz et al. 2021a).

5.3   Recruitment of VSOPs by CD44$^+$ macrophages

Previous studies showed interaction between CD44-expressing leukocytes and HA on endothelial cells of small vessels in colon tissue of DSS-induced colitis mice (Kessler et al. 2008). Additionally, de la Motte *et al*. detected increased mononuclear leukocyte adhesion to intestinal mucosal smooth muscle cells after virus infection via a CD44-HA interaction (de La Motte et al. 1999). In line with the higher HA content in colon tissue of DSS-induced colitis mice, the IMC data of these same mice showed a cluster of F4/80$^+$CD86$^+$ macrophages expressing CD44 (**Figure 4-11**). Interestingly, this cell cluster was also positive for VSOPs indicating that those cells co-localized with or phagocytosed the VSOPs. Due to IMC image resolution, it is not possible to conclude if VSOP-containing CD44$^+$ macrophages localize within small vessels in the colon tissue.

In addition, the CD31$^+$ endothelial cell cluster was positive for VSOPs as well. This is most likely owing to high amounts of VSOPs within the blood vessels as VSOPs were injected intravenously. Based on the results presented here it is not clear if VSOPs co-localize with CD31$^+$ endothelial cells additionally to CD44$^+$ macrophages or whether co-localization was detected due to interaction of both cell types.

Cell clusters containing VSOPs were detectable in early inflammation stages (**Figure 4-11, F**) and became more prominent in late inflammation (**Figure 4-11, G**), but were not found in healthy control (**Figure 4-11, E**). This supports the findings that CD44$^+$ macrophages get recruited to sites of inflammation due to increasing content of HA in colon tissue (de La Motte et al. 1999, Kessler et al. 2008). The results above suggest that CD44$^+$ macrophages containing VOSPs get recruited due to increased HA expression on endothelial cells of small vessels in inflamed colon tissue, while recruitment in healthy condition is not equally efficient due to lower HA expression on endothelial cells as graphically summarized in **Figure 5-1**.

A Inflammation

B Normal

CD44$^+$ Macrophage containing VSOPs   Endothelial cell   Hyaluronic acid
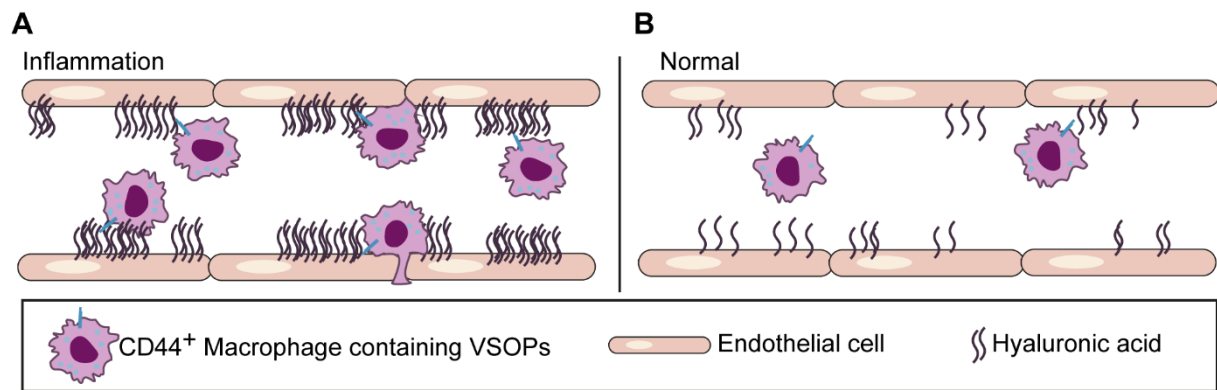
Figure 5-1: Proposed recruitment of VSOPs into inflamed colon tissue in the DSS-induced colitis mouse model. In the presence of inflammation endothelial cells of vessels in colon tissue show increased hyaluronic acid (HA) production that leads to CD44-HA-based interaction with CD44$^+$ macrophages that contain VSOPs, which then migrate into the inflamed tissue and induce a sufficient contrast change in MRI **(A)**. Under healthy conditions the HA content on endothelial cells is lower and interaction of CD44$^+$ macrophages containing VSOPs with HA is less likely and therefore no sufficient contrast change is detectable in MRI **(B)**.

So far, no studies describe the HA expression in transfer colitis mouse model apart from our own (Golusda et al. 2021).

In the transfer colitis mouse model, VSOPs mainly co-localized with CD31$^+$ endothelial cells (**Figure 4-12, D**). As mentioned above, this is likely due to intravenous injection of the contrast agent. Furthermore, the lower HA content in colon tissue of transfer colitis mice could reduce the recruitment of CD44$^+$ macrophages to the site of inflammation. Therefore, the additional factor transporting VSOPs to the site of inflammation is missing in the transfer colitis model. This might be a reason for the lack of T2 contrast in MRI examinations of transfer colitis mice even though IMC images show presence of VSOPs within the colon tissue. Thus, the significantly lower frequency of VSOP-positive cluster in colon tissues of transfer colitis mice compared to DSS-induced colitis might suggest an insufficient amount of VSOPs to induce T2 contrast in MRI (**Figure 13, C**). Within this work, no IMC analysis was done with the ileum tissue of *TNF$^{\Delta ARE}$* mice, which will be an important next step to understand lack of T2 contrast in this mouse model.

Strikingly, immunofluorescence staining against F4/80 and CD44 in colon tissue sections from DSS-induced colitis and transfer colitis did not reveal differences in the abundance of CD44$^+$ macrophages when compared to healthy colon tissue of respective control animals. Further, the DSS-induced colitis model and transfer colitis model showed same level of relative abundance of CD44$^+$ macrophages (**Figure 4-14**).

An upregulation of CD44 on vascular endothelial cells was reported under inflammatory condition (Mohamadzadeh et al. 1998). This can result in recruitment of macrophages expressing CD44 and binding in a sandwich-like manner as proposed in the model by Johnson and Ruffell 2009. Therefore, it would be of interest to investigate the expression of CD44 by endothelial cell in the intestinal tissue of experimental colitis mice. Still, IMC data in this study supports the idea that CD44$^+$ macrophages in DSS-induced colitis take up more VSOPs (**Figure 4-11, D**) compared to CD44$^+$ macrophages in transfer colitis (**Figure 4-12, D**), and differences in the relative amount of this cell type in both models was excluded as a reason for the differential accumulation of VSOPs (**Figure 4-14**). To comprehend why CD44$^+$ macrophages in DSS-induced colitis are more likely to internalize VSOPs needs further validation.

5.4 The influence of VSOPs on cells

One of the main concerns regarding contrast agents is their toxicity. Wagner *et al.* first reported *in vitro* experiments in mice and rats investigating the lethality of an acute single dose, finding that a level of 1.79 mmol Fe/kg in mice and 12.2 mmol Fe/kg in male rats and 8.7 mmol Fe/kg in female rats results in lethality within the first 24 hours. However, the applied doses in these experiments exceed the human dosage by a factor of 230 (Wagner et al. 2002). In a clinical phase I trial, VSOPs were injected into 18 healthy male human subjects where only 2 participants experienced a drop in blood, drop in oxygen saturation, dizziness and gastric spasms at the highest VSOP dose of 0.075 mmol Fe/kg few minutes after i.v. injection. Additional the effect on iron metabolism was investigated by assessing transferrin level, ferritin level and iron binding capacity. Short-term and dose-related changes were reported as increased ferritin levels were observed at 0.045 and 0.075 mmol Fe/kg after 2-8 days post i.v. injection (Taupitz et al. 2004). Up to today, no further *in-vivo* investigations addressing short-term and long-term consequences of VSOP application are published. Moreover, in the above-mentioned studies healthy animals as well as healthy human subjects were exposed to VSOPs. It would be of great importance to expose individuals suffering from various diseases to VSOPs since a burdened organism might react differently to VSOP exposure then healthy individuals.

5.4.1 Mesenteric lymph node-derived leukocytes

To assess the potential long-term effect of VSOPs on the immune cell compartment, mice experiencing colitis were exposed to VSOPs *in vivo*. This was performed by i.v. injection of VSOPs into transfer colitis mice and characterization of cell populations within the draining mesenteric lymph nodes (mLN). The draining mLN were investigated as this is where immunological information gets processed if relevant (Pabst et al. 2009). Importantly, the

VSOPs used in this experimental set-up were not doped with europium to prevent effect of manipulated VSOPs that might result in wrong conclusions.

While VSOPs have been used in various studies for MRI examinations *in vivo* (Millward et al. 2013, Berndt et al. 2017, Golusda et al. 2021, Silva et al. 2021, Wagner et al. 2002, Sharma et al. 2018) most of them focus on distribution within organs and basic toxicity effects but do not investigate the influence of VSOPs on specific cell types in detail and long-term. The mass cytometry characterization of CD45^{+} lymphocytes from mLN of transfer colitis mice exposed to VSOPs once and then analyzed 7, 10 and 18 days after exposure showed no significant changes in the abundance of cell populations in mLN (**Figure 4-16**).

A limitation in this experimental set-up is that the VSOPs were not traceable in the mLN as VSOPs without europium intercalation were used. Even though IMC data proved the presence of VSOPs in colon tissues of transfer colitis mice (**Figure 4-12**), it would be of great importance to evaluate the presence of VSOPs in mLN and additional organs like bone marrow and brain where VSOPs might accumulate. For an additional evaluation of VSOP influence on the intestinal immune system, lamina propria mononuclear cells need to be investigated. Up to today, long-term studies on VSOP exposure *in vivo* are lacking. The results presented in this thesis suggest no severe changes in cell phenotypes, activation states and proliferation rates up to 18 days post VSOP exposure.

Animals showed no signs of discomfort, such as dizziness or seizures, after VSOP injection that might indicate acute iron poisoning. Detailed analysis on the influence on iron metabolism was not done in this work. However, investigation of H&E-stained tissue sections from VSOP-exposed mice did not show differences in inflammation score compared to control (**Figure 4-17**). Several studies report an increase in serum iron level when animals are repeatedly injected with iron oxide nanoparticles (IONPs) (Bourrinet et al. 2006, Jain et al. 2008). In the above mentioned phase I clinical trial with VSOPs in 18 healthy male individuals an increase in ferritin was reported at 2-8 days post VSOP exposure at doses of 0.045 and 0.075 mmol Fe/kg (Taupitz et al. 2004). Even though the mass cytometry data and histopathology suggested no major long-term effects on lymphocyte populations and tissues in VSOP exposed mice, additional information on iron, transferrin and ferritin levels in serum or plasma and further investigations on long-term depositions of VSOPs and their excretion is required.

5.4.2 Human primary monocytes

The cytotoxicity effect of various IONPs *in vitro* has received increasing attention due to their promising use in IONP-based cell labeling for drug delivery or magnetic hyperthermia cancer treatment (Duguet et al. 2006, Dadfar et al. 2019). The same IONPs coating and size should always be considered when comparing results, since surface coating and particle size have

major influence on cytotoxicity (Malhotra et al. 2020, Singh et al. 2010). Soenen *et al*. investigated VSOPs with the same properties as those used within this study and evaluated the effect on cell cytoskeleton, morphology, proliferation, homeostasis, functionality, viability, and induction of reactive oxygen species (ROS) with three different cell lines (Soenen et al. 2011). The only reported effect was a high level of ROS production when the cells were labeled with 600 µg Fe/mL in culture. Additionally, poor internalization of VSOPs by mouse multi-potent neural progenitor (C17.2) cells was reported with a concentration of 18.65 ± 2.07 µg Fe/cell after 24h incubation (Soenen et al. 2011). In the experiments presented in this thesis, the concentration of VSOPs in monocytes after only 30 minutes of incubation was 3.93 ± 1.39 pg Fe/cell and after 180 minutes reached 12.47 ± 6.24 pg Fe/cell (**Figure 4-19, B**) which is consistent with studies investigating the VSOP uptake into the THP-1 monocyte cell line *in vitro* (Poller et al. 2016), but not with the above-mentioned study by Soenen et al., which might be due to higher VSOP concentrations used for *in vitro* stimulation (Soenen et al. 2011).

VSOP toxicity is largely evaluated with regard to *ex-vivo* cell labeling for *in-vitro* imaging or treatment. This procedure requires high concentrations of VSOPs for efficient labeling (Soenen et al. 2010, Soenen et al. 2011, Foldager et al. 2011, Radeloff et al. 2020, Radeloff et al. 2021, Stroh et al. 2005, Stroh et al. 2019, Stroh et al. 2006). In the study presented herein, VSOPs were applied as an intravenous contrast agent. Consequently, this led to lower exposure of cells to iron *in vivo*. As mass cytometry analysis of VSOP-treated whole blood identified monocytes as the main cell type responsible for particle uptake (**Figure 4-18**), this cell type was chosen for further investigations *in-vitro*. Previous reports focusing on labeling of murine monocytes with VSOPs with the same properties as the ones used in this thesis showed effects on monocyte viability which was significantly decreased after 24h stimulation while monocytes did not secrete pro-inflammatory cytokines following up to 24h exposure to VSOPs (Pohland et al. 2022). In line with this, RNA sequencing of *in vitro* VSOP-stimulated human monocytes showed no major gene expression changes (**Figure 4-20**). The most significant change was the downregulation of *Tfrc*, (Log2FC= -1.1, p_{adjust}<0.0001) (**Figure 4-20, A, C**), which is responsible for mediating cellular iron uptake and is regulated at transcriptional level upon iron stimulation (Gammella et al. 2017). Downregulation of *Tfrc* was reported upon stimulation with VSOPs (Soenen et al. 2011) and other IONPs (Schafer et al. 2007). Further *Mmp10* was one of the most significantly upregulated genes (**Figure 4-20, C**). *Mmp10* was reported to be upregulated by anti-inflammatory macrophages to clear scar tissue and is thought to be involved in healing processes of tissues (Koller et al. 2012, McMahan et al. 2016). Apart from this no other genes encoding for anti-inflammatory surface proteins or cytokines were up-regulated upon VSOP-stimulation.

IONPs with other properties than VSOPs have been reported to prime macrophages to adopt a pro-inflammatory phenotype (Mulens-Arias et al. 2015, Laskar et al. 2013). Kodali *et al*. reported a differential expression of 1,052 genes in macrophages treated with IONPs for 24h (Kodali et al. 2013). Importantly, exposure was longer than in the set-up presented in this study, while the concentration of IONPs is not stated and cannot be compared. Nonetheless, results on the influence of IONPs remain controversial because of high variability in experimental set-ups, the used cell type and IONPs properties.

In this thesis the viability of human-derived monocytes was neither influenced by different concentrations (0.5 mM, 0.75 mM and 1 mM) nor incubation times (30 or 90 minutes) of VSOP treatment when validated by flow cytometry (**Figure 4-21, B and E**) which is in line with previous findings by another study (Ludwig et al. 2013). Contrary to this, a different study reported an influence of VSOPs on cell viability in blood derived monocytes in mice (Pohland et al. 2022). The major difference in the study by Pohland *et al*. is the incubation time of 24h, whereas in the study presented herein the incubation time was 30 or 90 minutes. This could explain the different effects on cell variability.

In this study a deeper analysis of VSOP-treated monocytes showed that VSOPs did not induce a distinct differentiation. The frequencies of $CD14^{++}CD16^-$ cMon, $CD14^{++}CD16^+$ iMon and $CD14^+CD16^+$ ncMon were comparable to those of controls (**Figure 4-C, D, F and G**). Within the $CD14^{++}CD16^-$ cMon population, the abundance of $CCR2^-$ $CD206^+$ cells increased, at 48h after 90 minutes VSOP-exposure, with a statistically significant increase at a concentration of 1 mM (**Figure 4-21, H**). Moreover, the abundance of $HLA-DR^+CD86^+$ cell population within the $CD14^{++}CD16^-$ cMon increased with a statistical significance (**Figure 4-21, I**). These results suggest that VSOP treatment might prime cMon towards an iMon by increasing HLA-DR, CD86 and CD206 expression and down-regulating CCR2 (Kapellos et al. 2019).

Cytokine production of *in vitro* stimulated monocytes showed minor changes within cell culture supernatant at 24 h after VSOP exposure (**Figure 4-22**). TNFα concentrations were comparable to control levels in all conditions, indicating no major pro-inflammatory trigger by VSOPs (**Figure 4-22, A**). TNF-α is a good indicator for the pro-inflammatory state of monocytes, as it is usually upregulated in inflammatory condition, for example when exposed to lipopolysaccharides (LPS) *in vitro* (MacKenzie, Fernandez-Troy and Espel 2002). IL-1β is upregulated by monocytes as part of the inflammatory response, whereas IL-1RA prevents IL-1 signaling (Bent et al. 2018, Arend and Guthridge 2000). Monocyte supernatant showed increased concentrations of IL-1RA after 90 minutes of VSOP-stimulation (**Figure 4-22, B**) and in parallel downregulation of IL-1β by monocytes after 30 minutes VSOP-exposure (**Figure 4-22, D**). This indicates an inhibition of the pro-inflammatory response of cells upon VSOP treatment. Strikingly, 30 minutes of exposure induced a significant decrease in IL-1β

concentration but no increase in IL-1RA. In contrast, a 90 minutes exposure induced a significant increase in IL-1RA but no decrease in IL-1β (**Figure 4-22, B**). This requires further validation to connect the impact of VSOP uptake to signaling cascades in monocytes. The trend towards increased IL-10 concentrations further underlines priming of monocytes to an anti-inflammatory phenotype (**Figure 4-22, D**). Increased IL-10 secretion is strongly associated with anti-inflammatory responses (Rossato et al. 2012). This needs further validation with functional assays, for example proliferation or migration assays, stimulation responses of VSOP-treated monocytes to stimuli such as LPS or Interferon γ.

The flow cytometry and CBA results indicated slight shifts in the cell phenotype of monocytes upon VSOP treatment. Therefore, it would be important to investigate the influence of VSOPs on cells in an inflammatory milieu, for example during chronic inflammation as cells exposed to this kind of environment might react differently to VSOP-stimulation. Taken together, VSOPs do not influence viability nor induce major shifts in monocyte differentiation and activation state *in vitro*. Nevertheless, VSOP-exposed cells need to be thoroughly analyzed in functional assays and in an *in vivo* context, especially in an inflammatory set-up.

5.5 Clinical translation

The current standard procedure for clinical MRI examination in IBD patients includes T2w, fat-suppressed T2w and T1w pre and post GBCA for perianal CD and T2w measurements for the colon in CD patients. Further, the small bowel in CD patients is examined by application of oral contrast agent and T2w MRI scan plus T1w scans pre and post GBCA application (Shaban et al. 2022, Horsthuis et al. 2009). Intestinal peristaltic as well as breathing and other motion artefacts can limit accuracy of MRI examinations. Several technologies like breath-hold acquisition, respiratory compensation and administration of oral contrast agents improved this over the past years (Maccioni et al. 2000).

IONPs are investigated as oral contrast agents as oral administration induces a signal decrease in the intestinal lumen in T2w MRI. This oral application of IONPs can improve the signal in the surrounding intestinal wall (Hahn et al. 1990). So far, oral administration of IONPs in combination with i.v. GBCA was investigated in CD patients (Maccioni et al. 2000, Maccioni et al. 2006, Maccioni et al. 2002, Holzknecht et al. 2003, Holzknecht et al. 1998). With this combination in T1w MRI, the luminal signal decreases resulting in intestinal wall enhancement and a significant correlation of T1 parameter with the biologic activity in patients (Maccioni et al. 2006). Nonetheless, because of GBCA-associated concerns a set-up without the additional use of GBCAs is desired and applied in this thesis. To the best of my knowledge VSOPs have not been used to examine intestinal inflammation in mouse models so far.

In contrast to oral application, in this study VSOPs were applied i.v. for T2*w MRI examinations. Indeed, especially in T2*w pre-MR images, the problem of luminal contrast enhancement was observed during examination of inflamed colon (**Figure 4-3**) and it was not distinguishable if contrast enhancement derived from present edema or luminal content. Furthermore, air has the same contrast as VSOPs in a T*2w MR sequence and is present to a high amount in the colon lumen, providing an additional limitation. To ensure valid interpretation, an MRI examination before VSOP application is unavoidable. Since pre-MRI examinations were part of the experimental procedure in this study, the contrast changes in the colon region can be more precisely associated with VSOP-accumulation (**Figure 4-3**). An observed problem are motion artifacts in some of the MR images (**Figure 4-6; A**) which is a major limitation in the small animal MRI but various techniques are available for intestinal MRI of humans to counteract this limitation (Maccioni et al. 2002).

For T2 contrast agents the literature suggests the possibility of inducing a so-called "blooming effect" in MR images, which might lead to exaggeration in the size of labeled area or blur the image (Kim et al. 2011, Lee et al. 2011, Chen et al. 2022). In images of DSS-induced colitis mice, most of the colon areas represent a T2 contrast. Specific areas within the colon wall cannot be localized, which might be because of the blooming-effect, image resolution or simply the small size of the colon in mice. As the human intestine is larger compared to a mouse colon the limit of small organ size does not apply. Therefore, more precise determination of VSOP localization in for example mucosa or sub-mucosa might be possible. However, it has to be considered that the 7T MRI scanner which was used in this study provides a high resolution of MR images, while in a clinical set-up lower field intensities are used like for example a 3T MRI that in turn provides lower resolution in MR images (Hoyer et al. 2014). In general, MRI has the advantage to be non-invasive and provides a good overview of tissue and organs apart from mucosa, which is in contrast to endoscopy. However, the above-mentioned limitations in intestinal MRI examinations and VSOP-enhanced MRI need to be considered. Further, MRI examinations require high expertise and are associated with high costs thus limiting the availability of MRI machines in the clinic.

5.6 Conclusions

This thesis provides first steps towards VSOP-enhanced T2*w MRI that can be implemented for the detection of colon inflammation in DSS-induced colitis in early disease stages. The unsuccessful VSOP accumulation in inflamed intestines in two other mouse models needs further validation. It needs to be clarified if this is due to pathological integrity of tissue, the implemented MRI protocol or the VSOP incubation time. This is the most critical part for the translation into patients and clinical set-up. If VSOP accumulation is dependent on pathological

tissue integrity human translation will be challenging as IBD pathology is very heterogeneous. This heterogeneity was represented by the use of different mouse models and underlined by different contents of ECM components within inflamed tissues. The application of VSOPs as an alternative to GBCAs needs thorough investigation concerning their absorption, distribution, metabolism, and excretion which is currently incomplete, while the work in this thesis showed no major concerns. Moreover, various clinical trials will be needed to determine their valuable use in a heterogeneous disease type like IBD.

6   ABBREVIATIONS

APC	Antigen presenting cell
ARE	Adenosine-uracil rich elements
BM	Basal membrane
BSA	Bovine serum albumin
BSA	Bovine serum albumin
CBA	Cytometric bead array
CCR2	Chemokine receptor 2
CD	Crohn's disease
cDC	Conventional dendritic cell
cMon	Classical monocytes
CNR	Contrast to noise ratio
CSPG4	Chondroitin sulfate proteoglycan 4
CT	Computed tomography
CX_3CR1	C-X3-C motif chemokine receptor 1
CyTOF	Mass cytometry by time-of-flight
DC	Dendritic cell
DNA	Deoxyribonucleic acid
DSS	Dextran sodium sulfate
ECM	Extracellular Matrix
EDTA	Ethylenediaminetetraacetic acid
EMT	Epithelial to mesenchymal transition
FACS	Fluorescent activated cell sorting
FBS	Fetal bovine serum
FCS	Fetal bovine serum
FDA	Food and Drug Administration
GAG	Glycosaminogylcan

GBCA	Gadolinium based contrast agent
GM-CSF	granulocyte-macrophage colony stimulating factor
h	Hour
H&E	Hematoxylin and eosin
HA	Hyaluronic acid
HAS	Hyaluronic acid synthase
HBSS	Hank's Balanced Salt Solution
HLA-DR	Human leucocyte antigen receptor
HPF	High power field
HPLC	High-pressure liquid chromatography
HSC	Hematopoietic stem cell
HYAL	Hyaluronidase
i.v.	Intravenous
IL	Interleukin
IMC	Imaging mass cytometry
iMon	Intermediate monocytes
IONP	Iron oxide nanoparticle
LA-ICP-MS	Laser ablation inductively coupled mass spectrometry
LFA1	Lymphocyte function associated antigen-1
LOX	Lysyl oxidase
Ly6C	Lymphocyte antigen 6 complex
MACS	Magnetic-activated cell sorting
MHC	Major histocompatibility complex
min	Minutes
mLN	Mesenteric lymph nodes
MMP	Matrix metalloproteinases
MRA	Magnetic resonance angiography
MRI	Magnetic resonance imaging

ncMon	Non-classical monocytes
NK	Natural killer
PBS	Phosphate-buffered saline
PCR	Polymerase chain reaction
PCR	Polymerase chain reaction
pDC	plasmacytoid dendritic cell
PET	Positron emission tomography
PP	Peyer's patches
Pre-DC	Precursor dendritic cell
RA	Receptor antagonist
RNA	Ribonucleic acid
ROI	Region of interest
ROS	Reactive oxygen species
SD	Standard deviation
Sdc1	Syndecan-1
SNR	Signal to noise ratio
SPF	Specific pathogen free
SPIOs	Standard superparamagnetic iron oxide particles
T1w	T1-weighted
T2w	T2-weighted
TBST	Tris-buffered saline with tween20
TFRC	Transferrin receptor
T_H	T helper
TIMP	Tissue inhibitors of matrix metalloproteinases
TNF	Tumor necrosis factor
Treg	regulatory T cells
tSNE	t-distributed stochastic neighbor embedded
UC	Ulcerative colitis

UMAP	Uniform Manifold Approximation and Projection
US	Ultrasound
USPIOs	Ultra-small superparamagnetic iron oxide particles
VSOP	very small superparamagnetic iron particles
w/ VSOP	With very small superparamagnetic iron particles
w/o VSOP	Without very small superparamagnetic iron particles
WT	Wild-type

7 REFERENCES

Afratis, N., C. Gialeli, D. Nikitovic, T. Tsegenidis, E. Karousou, A. D. Theocharis, M. S. Pavao, G. N. Tzanakakis & N. K. Karamanos (2012) Glycosaminoglycans: key players in cancer cell biology and treatment. *FEBS J,* 279, 1177-97.

Aime, S. & P. Caravan (2009) Biodistribution of gadolinium-based contrast agents, including gadolinium deposition. *J Magn Reson Imaging,* 30, 1259-67.

Ali, A., H. Zafar, M. Zia, I. Ul Haq, A. R. Phull, J. S. Ali & A. Hussain (2016) Synthesis, characterization, applications, and challenges of iron oxide nanoparticles. *Nanotechnol Sci Appl,* 9, 49-67.

Arend, W. P. & C. J. Guthridge (2000) Biological role of interleukin 1 receptor antagonist isoforms. *Ann Rheum Dis,* 59 Suppl 1, i60-4.

Asseman, C., S. Read & F. Powrie (2003) Colitogenic Th1 cells are present in the antigen-experienced T cell pool in normal mice: control by CD4+ regulatory T cells and IL-10. *J Immunol,* 171, 971-8.

Atri, C., F. Z. Guerfali & D. Laouini (2018) Role of Human Macrophage Polarization in Inflammation during Infectious Diseases. *Int J Mol Sci,* 19.

Auffray, C., D. Fogg, M. Garfa, G. Elain, O. Join-Lambert, S. Kayal, S. Sarnacki, A. Cumano, G. Lauvau & F. Geissmann (2007) Monitoring of blood vessels and tissues by a population of monocytes with patrolling behavior. *Science,* 317, 666-70.

Bain, C. C. & A. M. Mowat (2014) Macrophages in intestinal homeostasis and inflammation. *Immunol Rev,* 260, 102-17.

Bain, C. C., C. L. Scott, H. Uronen-Hansson, S. Gudjonsson, O. Jansson, O. Grip, M. Guilliams, B. Malissen, W. W. Agace & A. M. Mowat (2013) Resident and pro-inflammatory macrophages in the colon represent alternative context-dependent fates of the same Ly6Chi monocyte precursors. *Mucosal Immunol,* 6, 498-510.

Bassler, K., J. Schulte-Schrepping, S. Warnat-Herresthal, A. C. Aschenbrenner & J. L. Schultze (2019) The Myeloid Cell Compartment-Cell by Cell. *Annu Rev Immunol,* 37, 269-293.

Baumgart, D. C. & W. J. Sandborn (2012) Crohn's disease. *Lancet,* 380, 1590-605.

Beltzer, A., T. Kaulisch, T. Bluhmki, T. Schoenberger, B. Stierstorfer & D. Stiller (2016) Evaluation of Quantitative Imaging Biomarkers in the DSS Colitis Model. *Mol Imaging Biol,* 18, 697-704.

Bent, R., L. Moll, S. Grabbe & M. Bros (2018) Interleukin-1 Beta-A Friend or Foe in Malignancies? *Int J Mol Sci,* 19.

Bernardo, D., M. Chaparro & J. P. Gisbert (2018) Human Intestinal Dendritic Cells in Inflammatory Bowel Diseases. *Mol Nutr Food Res,* 62, e1700931.

Berndt, D., J. M. Millward, J. Schnorr, M. Taupitz, V. Stangl, F. Paul, S. Wagner, J. T. Wuerfel, I. Sack, A. Ludwig & C. Infante-Duarte (2017) Inflammation-induced brain endothelial activation leads

to uptake of electrostatically stabilized iron oxide nanoparticles via sulfated glycosaminoglycans. *Nanomedicine,* 13**,** 1411-1421.

Bettenworth, D., A. Bokemeyer, M. Baker, R. Mao, C. E. Parker, T. Nguyen, C. Ma, J. Panes, J. Rimola, J. G. Fletcher, V. Jairath, B. G. Feagan, F. Rieder, T. Stenosis & C. Anti-Fibrotic Research (2019) Assessment of Crohn's disease-associated small bowel strictures and fibrosis on cross-sectional imaging: a systematic review. *Gut,* 68**,** 1115-1126.

Bianchi, A., T. Bluhmki, T. Schonberger, E. Kaaru, A. Beltzer, E. Raymond, A. Wunder, P. Thakker, B. Stierstorfer & D. Stiller (2016) Noninvasive Longitudinal Study of a Magnetic Resonance Imaging Biomarker for the Quantification of Colon Inflammation in a Mouse Model of Colitis. *Inflamm Bowel Dis,* 22**,** 1286-95.

Biskup, K., C. Stellmach, E. I. Braicu, J. Sehouli & V. Blanchard (2021) Chondroitin Sulfate Disaccharides, a Serum Marker for Primary Serous Epithelial Ovarian Cancer. *Diagnostics (Basel),* 11.

Biton, I. E., N. Stettner, O. Brener, A. Erez, A. Harmelin & J. R. Garbow (2018) Assessing Mucosal Inflammation in a DSS-Induced Colitis Mouse Model by MR Colonography. *Tomography,* 4**,** 4-13.

Bonnans, C., J. Chou & Z. Werb (2014) Remodelling the extracellular matrix in development and disease. *Nat Rev Mol Cell Biol,* 15**,** 786-801.

Bouatrouss, Y., F. E. Herring-Gillam, J. Gosselin, J. Poisson & J. F. Beaulieu (2000) Altered expression of laminins in Crohn's disease small intestinal mucosa. *Am J Pathol,* 156**,** 45-50.

Bourrinet, P., H. H. Bengele, B. Bonnemain, A. Dencausse, J. M. Idee, P. M. Jacobs & J. M. Lewis (2006) Preclinical safety and pharmacokinetic profile of ferumoxtran-10, an ultrasmall superparamagnetic iron oxide magnetic resonance contrast agent. *Invest Radiol,* 41**,** 313-24.

Braun, J., X. Baraliakos, W. Golder, K. G. Hermann, J. Listing, J. Brandt, M. Rudwaleit, S. Zuehlsdorf, M. Bollow, J. Sieper & D. van der Heijde (2004) Analysing chronic spinal changes in ankylosing spondylitis: a systematic comparison of conventional x rays with magnetic resonance imaging using established and new scoring systems. *Ann Rheum Dis,* 63**,** 1046-55.

Breynaert, C., T. Dresselaers, C. Perrier, I. Arijs, J. Cremer, L. Van Lommel, K. Van Steen, M. Ferrante, F. Schuit, S. Vermeire, P. Rutgeerts, U. Himmelreich, J. L. Ceuppens, K. Geboes & G. Van Assche (2013) Unique gene expression and MR T2 relaxometry patterns define chronic murine dextran sodium sulphate colitis as a model for connective tissue changes in human Crohn's disease. *PLoS One,* 8**,** e68876.

Chapuy, L. & M. Sarfati (2020) Single-Cell Protein and RNA Expression Analysis of Mononuclear Phagocytes in Intestinal Mucosa and Mesenteric Lymph Nodes of Ulcerative Colitis and Crohn's Disease Patients. *Cells,* 9.

Chassaing, B., J. D. Aitken, M. Malleshappa & M. Vijay-Kumar (2014) Dextran sulfate sodium (DSS)-induced colitis in mice. *Curr Protoc Immunol,* 104**,** 15 25 1-15 25 14.

Chen, C., J. Ge, Y. Gao, L. Chen, J. Cui, J. Zeng & M. Gao (2022) Ultrasmall superparamagnetic iron oxide nanoparticles: A next generation contrast agent for magnetic resonance imaging. *Wiley Interdiscip Rev Nanomed Nanobiotechnol,* 14**,** e1740.

Chen, H., L. Chen, X. Wang, X. Ge, L. Sun, Z. Wang, X. Xu, Y. Song, J. Chen, Q. Deng, H. Xie, T. Chen, Y. Chen, K. Ding, J. Wu & J. Wang (2021) Transgenic overexpression of ITGB6 in intestinal epithelial cells exacerbates dextran sulfate sodium-induced colitis in mice. *J Cell Mol Med,* 25**,** 2679-2690.

Coquery, N., A. Blesch, A. Stroh, F. Fernandez-Klett, J. Klein, C. Winter & J. Priller (2012) Intrahippocampal transplantation of mesenchymal stromal cells promotes neuroplasticity. *Cytotherapy,* 14**,** 1041-53.

Cosnes, J., C. Gower-Rousseau, P. Seksik & A. Cortot (2011) Epidemiology and natural history of inflammatory bowel diseases. *Gastroenterology,* 140**,** 1785-94.

da Silva, B. C., A. C. Lyra, R. Rocha & G. O. Santana (2014) Epidemiology, demographic characteristics and prognostic predictors of ulcerative colitis. *World J Gastroenterol,* 20**,** 9458-67.

Dadfar, S. M., K. Roemhild, N. I. Drude, S. von Stillfried, R. Knuchel, F. Kiessling & T. Lammers (2019) Iron oxide nanoparticles: Diagnostic, therapeutic and theranostic applications. *Adv Drug Deliv Rev,* 138**,** 302-325.

de La Motte, C. A., V. C. Hascall, A. Calabro, B. Yen-Lieberman & S. A. Strong (1999) Mononuclear leukocytes preferentially bind via CD44 to hyaluronan on human intestinal mucosal smooth muscle cells after virus infection or treatment with poly(I.C). *J Biol Chem,* 274**,** 30747-55.

de Schellenberger, A. A., R. Hauptmann, J. M. Millward, E. Schellenberger, Y. Kobayashi, M. Taupitz, C. Infante-Duarte, J. Schnorr & S. Wagner (2017) Synthesis of europium-doped VSOP, customized enhancer solution and improved microscopy fluorescence methodology for unambiguous histological detection. *J Nanobiotechnology,* 15**,** 71.

Deepak, P., K. J. Fowler, J. G. Fletcher & D. H. Bruining (2019) Novel Imaging Approaches in Inflammatory Bowel Diseases. *Inflamm Bowel Dis,* 25**,** 248-260.

Derkacz, A., P. Olczyk, A. Jura-Poltorak, K. Olczyk & K. Komosinska-Vassev (2021a) The Diagnostic Usefulness of Circulating Profile of Extracellular Matrix Components: Sulfated Glycosaminoglycans (sGAG), Hyaluronan (HA) and Extracellular Part of Syndecan-1 (sCD138) in Patients with Crohn's Disease and Ulcerative Colitis. *J Clin Med,* 10.

Derkacz, A., P. Olczyk, K. Olczyk & K. Komosinska-Vassev (2021b) The Role of Extracellular Matrix Components in Inflammatory Bowel Diseases. *J Clin Med,* 10.

Dieleman, L. A., M. J. Palmen, H. Akol, E. Bloemena, A. S. Pena, S. G. Meuwissen & E. P. Van Rees (1998) Chronic experimental colitis induced by dextran sulphate sodium (DSS) is characterized by Th1 and Th2 cytokines. *Clin Exp Immunol,* 114**,** 385-91.

Dobin, A., C. A. Davis, F. Schlesinger, J. Drenkow, C. Zaleski, S. Jha, P. Batut, M. Chaisson & T. R. Gingeras (2013) STAR: ultrafast universal RNA-seq aligner. *Bioinformatics,* 29**,** 15-21.

Duguet, E., S. Vasseur, S. Mornet & J. M. Devoiselle (2006) Magnetic nanoparticles and their applications in medicine. *Nanomedicine (Lond),* 1**,** 157-68.

Dulinska-Litewka, J., A. Lazarczyk, P. Halubiec, O. Szafranski, K. Karnas & A. Karewicz (2019) Superparamagnetic Iron Oxide Nanoparticles-Current and Prospective Medical Applications. *Materials (Basel),* 12.

Eichele, D. D. & K. K. Kharbanda (2017) Dextran sodium sulfate colitis murine model: An indispensable tool for advancing our understanding of inflammatory bowel diseases pathogenesis. *World J Gastroenterol,* 23**,** 6016-6029.

Erben, U., C. Loddenkemper, K. Doerfel, S. Spieckermann, D. Haller, M. M. Heimesaat, M. Zeitz, B. Siegmund & A. A. Kuhl (2014) A guide to histomorphological evaluation of intestinal inflammation in mouse models. *Int J Clin Exp Pathol,* 7**,** 4557-76.

Esterhazy, D., M. C. C. Canesso, L. Mesin, P. A. Muller, T. B. R. de Castro, A. Lockhart, M. ElJalby, A. M. C. Faria & D. Mucida (2019) Compartmentalized gut lymph node drainage dictates adaptive immune responses. *Nature,* 569**,** 126-130.

Ewels, P. A., A. Peltzer, S. Fillinger, H. Patel, J. Alneberg, A. Wilm, M. U. Garcia, P. Di Tommaso & S. Nahnsen (2020) The nf-core framework for community-curated bioinformatics pipelines. *Nat Biotechnol,* 38**,** 276-278.

Fang, C., N. Bhattarai, C. Sun & M. Zhang (2009) Functionalized nanoparticles with long-term stability in biological media. *Small,* 5**,** 1637-41.

Floer, M., M. Clausen, T. Meister, R. Vollenberg, D. Bettenworth & P. R. Tepasse (2021) Soluble syndecan-1 as marker of intestinal inflammation: A preliminary study and evaluation of a new panel of biomarkers for non-invasive prediction of active ulcerative colitis. *Adv Clin Exp Med,* 30**,** 655-660.

Floer, M., M. Gotte, M. K. Wild, J. Heidemann, E. S. Gassar, W. Domschke, L. Kiesel, A. Luegering & T. Kucharzik (2010) Enoxaparin improves the course of dextran sodium sulfate-induced colitis in syndecan-1-deficient mice. *Am J Pathol,* 176**,** 146-57.

Flood, T. F., N. V. Stence, J. A. Maloney & D. M. Mirsky (2017) Pediatric Brain: Repeated Exposure to Linear Gadolinium-based Contrast Material Is Associated with Increased Signal Intensity at Unenhanced T1-weighted MR Imaging. *Radiology,* 282**,** 222-228.

Florie, J., K. Horsthuis, D. W. Hommes, C. Y. Nio, J. B. Reitsma, S. J. van Deventer & J. Stoker (2005) Magnetic resonance imaging compared with ileocolonoscopy in evaluating disease severity in Crohn's disease. *Clin Gastroenterol Hepatol,* 3**,** 1221-8.

Foldager, C. B., M. Pedersen, S. Ringgaard, C. Bunger & M. Lind (2011) Chondrocyte gene expression is affected by very small iron oxide particles-labeling in long-term in vitro MRI tracking. *J Magn Reson Imaging,* 33**,** 724-30.

Frantz, C., K. M. Stewart & V. M. Weaver (2010) The extracellular matrix at a glance. *J Cell Sci,* 123**,** 4195-200.

Frericks, B. B., A. A. Kuhl, C. Loddenkemper, A. Stroux, S. Valdeig, B. Hotz, B. Misselwitz, J. C. Hoffmann & F. K. Wacker (2011) Gadofluorine M-enhanced magnetic resonance imaging of inflammatory bowel disease: quantitative analysis and histologic correlation in a rat model. *Invest Radiol,* 46**,** 478-85.

Gammella, E., P. Buratti, G. Cairo & S. Recalcati (2017) The transferrin receptor: the cellular iron gate. *Metallomics,* 9**,** 1367-1375.

Geppert, M. & M. Himly (2021) Iron Oxide Nanoparticles in Bioimaging - An Immune Perspective. *Front Immunol,* 12**,** 688927.

Gikas, A. & J. K. Triantafillidis (2014) The role of primary care physicians in early diagnosis and treatment of chronic gastrointestinal diseases. *Int J Gen Med,* 7**,** 159-73.

Ginhoux, F., M. Greter, M. Leboeuf, S. Nandi, P. See, S. Gokhan, M. F. Mehler, S. J. Conway, L. G. Ng, E. R. Stanley, I. M. Samokhvalov & M. Merad (2010) Fate mapping analysis reveals that adult microglia derive from primitive macrophages. *Science,* 330**,** 841-5.

Ginhoux, F. & S. Jung (2014) Monocytes and macrophages: developmental pathways and tissue homeostasis. *Nat Rev Immunol,* 14**,** 392-404.

Golusda, L., A. A. Kuhl, M. Lehmann, K. Dahlke, S. Mueller, P. Boehm-Sturm, J. Saatz, H. Traub, J. Schnorr, C. Freise, M. Taupitz, K. Biskup, V. Blanchard, O. Klein, I. Sack, B. Siegmund & D. Paclik (2022) Visualization of Inflammation in Experimental Colitis by Magnetic Resonance Imaging Using Very Small Superparamagnetic Iron Oxide Particles. *Front Physiol,* 13**,** 862212.

Golusda, L., A. A. Kuhl, B. Siegmund & D. Paclik (2021) Extracellular Matrix Components as Diagnostic Tools in Inflammatory Bowel Disease. *Biology (Basel),* 10.

Gomollon, F., A. Dignass, V. Annese, H. Tilg, G. Van Assche, J. O. Lindsay, L. Peyrin-Biroulet, G. J. Cullen, M. Daperno, T. Kucharzik, F. Rieder, S. Almer, A. Armuzzi, M. Harbord, J. Langhorst, M. Sans, Y. Chowers, G. Fiorino, P. Juillerat, G. J. Mantzaris, F. Rizzello, S. Vavricka, P. Gionchetti & Ecco (2017) 3rd European Evidence-based Consensus on the Diagnosis and Management of Crohn's Disease 2016: Part 1: Diagnosis and Medical Management. *J Crohns Colitis,* 11**,** 3-25.

Guan, Q. (2019) A Comprehensive Review and Update on the Pathogenesis of Inflammatory Bowel Disease. *J Immunol Res,* 2019**,** 7247238.

Guilliams, M., F. Ginhoux, C. Jakubzick, S. H. Naik, N. Onai, B. U. Schraml, E. Segura, R. Tussiwand & S. Yona (2014) Dendritic cells, monocytes and macrophages: a unified nomenclature based on ontogeny. *Nat Rev Immunol,* 14**,** 571-8.

Hahn, P. F., D. D. Stark, J. M. Lewis, S. Saini, G. Elizondo, R. Weissleder, C. J. Fretz & J. T. Ferrucci (1990) First clinical trial of a new superparamagnetic iron oxide for use as an oral gastrointestinal contrast agent in MR imaging. *Radiology,* 175**,** 695-700.

Halfter, W., P. Oertle, C. A. Monnier, L. Camenzind, M. Reyes-Lua, H. Hu, J. Candiello, A. Labilloy, M. Balasubramani, P. B. Henrich & M. Plodinec (2015) New concepts in basement membrane biology. *FEBS J,* 282**,** 4466-79.

Haniffa, M., V. Bigley & M. Collin (2015) Human mononuclear phagocyte system reunited. *Semin Cell Dev Biol,* 41**,** 59-69.

Hashimoto, D., A. Chow, C. Noizat, P. Teo, M. B. Beasley, M. Leboeuf, C. D. Becker, P. See, J. Price, D. Lucas, M. Greter, A. Mortha, S. W. Boyer, E. C. Forsberg, M. Tanaka, N. van Rooijen, A. Garcia-Sastre, E. R. Stanley, F. Ginhoux, P. S. Frenette & M. Merad (2013) Tissue-resident macrophages self-maintain locally throughout adult life with minimal contribution from circulating monocytes. *Immunity,* 38**,** 792-804.

Holzknecht, N., T. Helmberger, K. Herrmann, T. Ochsenkuhn, B. Goke & M. Reiser (2003) [MRI in Crohn's disease after transduodenal contrast administration using negative oral MRI contrast media]. *Radiologe,* 43**,** 43-50.

Holzknecht, N., T. Helmberger, C. von Ritter, J. Gauger, S. Faber & M. Reiser (1998) [MRI of the small intestine with rapid MRI sequences in Crohn disease after enteroclysis with oral iron particles]. *Radiologe,* 38**,** 29-36.

Horsthuis, K., A. J. Nederveen, M. W. de Feiter, C. Lavini, P. C. Stokkers & J. Stoker (2009) Mapping of T1-values and Gadolinium-concentrations in MRI as indicator of disease activity in luminal Crohn's disease: a feasibility study. *J Magn Reson Imaging,* 29**,** 488-93.

Hoyer, C., N. Gass, W. Weber-Fahr & A. Sartorius (2014) Advantages and challenges of small animal magnetic resonance imaging as a translational tool. *Neuropsychobiology,* 69**,** 187-201.

Hu, J., P. E. Van den Steen, Q. X. Sang & G. Opdenakker (2007) Matrix metalloproteinase inhibitors as therapy for inflammatory and vascular diseases. *Nat Rev Drug Discov,* 6**,** 480-98.

Hundhausen, C., R. Schneckmann, Y. Ostendorf, J. Rimpler, A. von Glinski, C. Kohlmorgen, N. Pasch, L. Rolauer, F. von Ameln, O. Eckermann, J. Altschmied, N. Ale-Agha, J. Haendeler, U. Flogel, J. W. Fischer & M. Grandoch (2021) Endothelial hyaluronan synthase 3 aggravates acute colitis in an experimental model of inflammatory bowel disease. *Matrix Biol,* 102**,** 20-36.

Hunger, M., E. Budinger, K. Zhong & F. Angenstein (2014) Visualization of acute focal lesions in rats with experimental autoimmune encephalomyelitis by magnetic nanoparticles, comparing different MRI sequences including phase imaging. *J Magn Reson Imaging,* 39**,** 1126-35.

Hynes, R. O. & A. Naba (2012) Overview of the matrisome--an inventory of extracellular matrix constituents and functions. *Cold Spring Harb Perspect Biol,* 4**,** a004903.

Hyun, S. B., Y. Kitazume, M. Nagahori, A. Toriihara, T. Fujii, K. Tsuchiya, S. Suzuki, E. Okada, A. Araki, M. Naganuma & M. Watanabe (2011) Magnetic resonance enterocolonography is useful for simultaneous evaluation of small and large intestinal lesions in Crohn's disease. *Inflamm Bowel Dis,* 17**,** 1063-72.

Iozzo, R. V. (1998) Matrix proteoglycans: from molecular design to cellular function. *Annu Rev Biochem,* 67**,** 609-52.

Iozzo, R. V. & L. Schaefer (2015) Proteoglycan form and function: A comprehensive nomenclature of proteoglycans. *Matrix Biol,* 42**,** 11-55.

Italiani, P., E. M. Mazza, D. Lucchesi, I. Cifola, C. Gemelli, A. Grande, C. Battaglia, S. Bicciato & D. Boraschi (2014) Transcriptomic profiling of the development of the inflammatory response in human monocytes in vitro. *PLoS One,* 9**,** e87680.

Jain, T. K., M. K. Reddy, M. A. Morales, D. L. Leslie-Pelecky & V. Labhasetwar (2008) Biodistribution, clearance, and biocompatibility of iron oxide magnetic nanoparticles in rats. *Mol Pharm,* 5**,** 316-27.

Jaynes, J. M., R. Sable, M. Ronzetti, W. Bautista, Z. Knotts, A. Abisoye-Ogunniyan, D. Li, R. Calvo, M. Dashnyam, A. Singh, T. Guerin, J. White, S. Ravichandran, P. Kumar, K. Talsania, V. Chen, A. Ghebremedhin, B. Karanam, A. Bin Salam, R. Amin, T. Odzorig, T. Aiken, V. Nguyen, Y. Bian, J. C. Zarif, A. E. de Groot, M. Mehta, L. Fan, X. Hu, A. Simeonov, N. Pate, M. Abu-Asab, M. Ferrer, N. Southall, C. Y. Ock, Y. Zhao, H. Lopez, S. Kozlov, N. de Val, C. C. Yates, B. Baljinnyam, J. Marugan & U. Rudloff (2020) Mannose receptor (CD206) activation in tumor-associated macrophages enhances adaptive and innate antitumor immune responses. *Sci Transl Med,* 12.

Jeon, M., M. V. Halbert, Z. R. Stephen & M. Zhang (2021) Iron Oxide Nanoparticles as T1 Contrast Agents for Magnetic Resonance Imaging: Fundamentals, Challenges, Applications, and Prospectives. *Adv Mater,* 33**,** e1906539.

Joeris, T., K. Muller-Luda, W. W. Agace & A. M. Mowat (2017) Diversity and functions of intestinal mononuclear phagocytes. *Mucosal Immunol,* 10**,** 845-864.

Johnson, P. & B. Ruffell (2009) CD44 and its role in inflammation and inflammatory diseases. *Inflamm Allergy Drug Targets,* 8**,** 208-20.

Jokerst, J. V., T. Lobovkina, R. N. Zare & S. S. Gambhir (2011) Nanoparticle PEGylation for imaging and therapy. *Nanomedicine (Lond),* 6**,** 715-28.

Kalluri, R. & M. Zeisberg (2006) Fibroblasts in cancer. *Nat Rev Cancer,* 6**,** 392-401.

Kamada, N., T. Hisamatsu, S. Okamoto, H. Chinen, T. Kobayashi, T. Sato, A. Sakuraba, M. T. Kitazume, A. Sugita, K. Koganei, K. S. Akagawa & T. Hibi (2008) Unique CD14 intestinal macrophages contribute to the pathogenesis of Crohn disease via IL-23/IFN-gamma axis. *J Clin Invest,* 118**,** 2269-80.

Kanda, T., K. Ishii, H. Kawaguchi, K. Kitajima & D. Takenaka (2014) High signal intensity in the dentate nucleus and globus pallidus on unenhanced T1-weighted MR images: relationship with increasing cumulative dose of a gadolinium-based contrast material. *Radiology,* 270**,** 834-41.

Kapellos, T. S., L. Bonaguro, I. Gemund, N. Reusch, A. Saglam, E. R. Hinkley & J. L. Schultze (2019) Human Monocyte Subsets and Phenotypes in Major Chronic Inflammatory Diseases. *Front Immunol,* 10**,** 2035.

Kaplan, G. G. (2015) The global burden of IBD: from 2015 to 2025. *Nat Rev Gastroenterol Hepatol,* 12**,** 720-7.

Karamanos, N. K., A. D. Theocharis, Z. Piperigkou, D. Manou, A. Passi, S. S. Skandalis, D. H. Vynios, V. Orian-Rousseau, S. Ricard-Blum, C. E. H. Schmelzer, L. Duca, M. Durbeej, N. A. Afratis, L. Troeberg, M. Franchi, V. Masola & M. Onisto (2021) A guide to the composition and functions of the extracellular matrix. *FEBS J,* 288**,** 6850-6912.

Karsdal, M. A., S. H. Nielsen, D. J. Leeming, L. L. Langholm, M. J. Nielsen, T. Manon-Jensen, A. Siebuhr, N. S. Gudmann, S. Ronnow, J. M. Sand, S. J. Daniels, J. H. Mortensen & D. Schuppan (2017) The good and the bad collagens of fibrosis - Their role in signaling and organ function. *Adv Drug Deliv Rev,* 121**,** 43-56.

Kaufels, N., R. Korn, S. Wagner, T. Schink, B. Hamm, M. Taupitz & J. Schnorr (2008) Magnetic resonance imaging of liver metastases: experimental comparison of anionic and conventional superparamagnetic iron oxide particles with a hepatobiliary contrast medium during dynamic and uptake phases. *Invest Radiol,* 43**,** 496-503.

Kessler, S., H. Rho, G. West, C. Fiocchi, J. Drazba & C. de la Motte (2008) Hyaluronan (HA) deposition precedes and promotes leukocyte recruitment in intestinal inflammation. *Clin Transl Sci,* 1**,** 57-61.

Kessler, S. P., D. R. Obery & C. de la Motte (2015) Hyaluronan Synthase 3 Null Mice Exhibit Decreased Intestinal Inflammation and Tissue Damage in the DSS-Induced Colitis Model. *Int J Cell Biol,* 2015**,** 745237.

Kim, B. H., N. Lee, H. Kim, K. An, Y. I. Park, Y. Choi, K. Shin, Y. Lee, S. G. Kwon, H. B. Na, J. G. Park, T. Y. Ahn, Y. W. Kim, W. K. Moon, S. H. Choi & T. Hyeon (2011) Large-scale synthesis of uniform and extremely small-sized iron oxide nanoparticles for high-resolution T1 magnetic resonance imaging contrast agents. *J Am Chem Soc,* 133**,** 12624-31.

Kirkegaard, T., A. Hansen, E. Bruun & J. Brynskov (2004) Expression and localisation of matrix metalloproteinases and their natural inhibitors in fistulae of patients with Crohn's disease. *Gut,* 53**,** 701-9.

Kobayashi, T., T. Chanmee & N. Itano (2020) Hyaluronan: Metabolism and Function. *Biomolecules,* 10.

Kodali, V., M. H. Littke, S. C. Tilton, J. G. Teeguarden, L. Shi, C. W. Frevert, W. Wang, J. G. Pounds & B. D. Thrall (2013) Dysregulation of macrophage activation profiles by engineered nanoparticles. *ACS Nano,* 7**,** 6997-7010.

Koivisto, L., J. Bi, L. Hakkinen & H. Larjava (2018) Integrin alphavbeta6: Structure, function and role in health and disease. *Int J Biochem Cell Biol,* 99**,** 186-196.

Koller, F. L., E. A. Dozier, K. T. Nam, M. Swee, T. P. Birkland, W. C. Parks & B. Fingleton (2012) Lack of MMP10 exacerbates experimental colitis and promotes development of inflammation-associated colonic dysplasia. *Lab Invest,* 92**,** 1749-59.

Kolset, S. O. & H. Tveit (2008) Serglycin--structure and biology. *Cell Mol Life Sci,* 65**,** 1073-85.

Kontoyiannis, D., M. Pasparakis, T. T. Pizarro, F. Cominelli & G. Kollias (1999) Impaired on/off regulation of TNF biosynthesis in mice lacking TNF AU-rich elements: implications for joint and gut-associated immunopathologies. *Immunity,* 10**,** 387-98.

Krause, P., V. Morris, J. A. Greenbaum, Y. Park, U. Bjoerheden, Z. Mikulski, T. Muffley, J. W. Shui, G. Kim, H. Cheroutre, Y. C. Liu, B. Peters, M. Kronenberg & M. Murai (2015) IL-10-producing intestinal macrophages prevent excessive antibacterial innate immunity by limiting IL-23 synthesis. *Nat Commun,* 6**,** 7055.

Kuroda, N., M. Masuya, I. Tawara, J. Tsuboi, M. Yoneda, K. Nishikawa, Y. Kageyama, K. Hachiya, K. Ohishi, H. Miwa, R. Yamada, Y. Hamada, K. Tanaka, T. Kato, Y. Takei & N. Katayama (2019) Infiltrating CCR2(+) monocytes and their progenies, fibrocytes, contribute to colon fibrosis by inhibiting collagen degradation through the production of TIMP-1. *Sci Rep,* 9**,** 8568.

Lakatos, G., F. Sipos, P. Miheller, I. Hritz, M. Z. Varga, M. Juhasz, B. Molnar, Z. Tulassay & L. Herszenyi (2012) The behavior of matrix metalloproteinase-9 in lymphocytic colitis, collagenous colitis and ulcerative colitis. *Pathol Oncol Res,* 18**,** 85-91.

Larsson, A. E., S. Melgar, E. Rehnstrom, E. Michaelsson, L. Svensson, P. Hockings & L. E. Olsson (2006) Magnetic resonance imaging of experimental mouse colitis and association with inflammatory activity. *Inflamm Bowel Dis,* 12**,** 478-85.

Laskar, A., J. Eilertsen, W. Li & X. M. Yuan (2013) SPION primes THP1 derived M2 macrophages towards M1-like macrophages. *Biochem Biophys Res Commun,* 441**,** 737-42.

Latella, G., J. Di Gregorio, V. Flati, F. Rieder & I. C. Lawrance (2015) Mechanisms of initiation and progression of intestinal fibrosis in IBD. *Scand J Gastroenterol,* 50**,** 53-65.

Lawrance, I. C., G. Rogler, G. Bamias, C. Breynaert, J. Florholmen, G. Pellino, S. Reif, S. Speca & G. Latella (2017) Cellular and Molecular Mediators of Intestinal Fibrosis. *J Crohns Colitis,* 11**,** 1491-1503.

Lee, N., H. Kim, S. H. Choi, M. Park, D. Kim, H. C. Kim, Y. Choi, S. Lin, B. H. Kim, H. S. Jung, H. Kim, K. S. Park, W. K. Moon & T. Hyeon (2011) Magnetosome-like ferrimagnetic iron oxide nanocubes for highly sensitive MRI of single cells and transplanted pancreatic islets. *Proc Natl Acad Sci U S A,* 108**,** 2662-7.

Leeb, S. N., D. Vogl, M. Gunckel, S. Kiessling, W. Falk, M. Goke, J. Scholmerich, C. M. Gelbmann & G. Rogler (2003) Reduced migration of fibroblasts in inflammatory bowel disease: role of inflammatory mediators and focal adhesion kinase. *Gastroenterology,* 125**,** 1341-54.

Lehmann, M., K. Allers, C. Heldt, J. Meinhardt, F. Schmidt, Y. Rodriguez-Sillke, D. Kunkel, M. Schumann, C. Bottcher, C. Stahl-Hennig, S. Elezkurtaj, C. Bojarski, H. Radbruch, V. M. Corman, T. Schneider, C. Loddenkemper, V. Moos, C. Weidinger, A. A. Kuhl & B. Siegmund (2021) Human small intestinal infection by SARS-CoV-2 is characterized by a mucosal infiltration with activated CD8(+) T cells. *Mucosal Immunol,* 14**,** 1381-1392.

Levine, J. H., E. F. Simonds, S. C. Bendall, K. L. Davis, A. D. Amir el, M. D. Tadmor, O. Litvin, H. G. Fienberg, A. Jager, E. R. Zunder, R. Finck, A. L. Gedman, I. Radtke, J. R. Downing, D. Pe'er & G. P. Nolan (2015) Data-Driven Phenotypic Dissection of AML Reveals Progenitor-like Cells that Correlate with Prognosis. *Cell,* 162**,** 184-97.

Liao, Z. X., D. L. Ou, M. J. Hsieh & C. C. Hsieh (2021) Synergistic Effect of Repolarization of M2 to M1 Macrophages Induced by Iron Oxide Nanoparticles Combined with Lactate Oxidase. *Int J Mol Sci,* 22.

Lindholm, M., L. E. Godskesen, T. Manon-Jensen, J. Kjeldsen, A. Krag, M. A. Karsdal & J. H. Mortensen (2021) Endotrophin and C6Ma3, serological biomarkers of type VI collagen remodelling, reflect endoscopic and clinical disease activity in IBD. *Sci Rep,* 11**,** 14713.

Litwiniuk, M., A. Krejner, M. S. Speyrer, A. R. Gauto & T. Grzela (2016) Hyaluronic Acid in Inflammation and Tissue Regeneration. *Wounds,* 28**,** 78-88.

Love, M. I., W. Huber & S. Anders (2014) Moderated estimation of fold change and dispersion for RNA-seq data with DESeq2. *Genome Biol,* 15**,** 550.

Ludwig, A., W. C. Poller, K. Westphal, S. Minkwitz, G. Lattig-Tunnemann, S. Metzkow, K. Stangl, G. Baumann, M. Taupitz, S. Wagner, J. Schnorr & V. Stangl (2013) Rapid binding of electrostatically stabilized iron oxide nanoparticles to THP-1 monocytic cells via interaction with glycosaminoglycans. *Basic Res Cardiol,* 108**,** 328.

Lynch, M. D. & F. M. Watt (2018) Fibroblast heterogeneity: implications for human disease. *J Clin Invest,* 128**,** 26-35.

Maccioni, F., A. Bruni, A. Viscido, M. C. Colaiacomo, A. Cocco, C. Montesani, R. Caprilli & M. Marini (2006) MR imaging in patients with Crohn disease: value of T2- versus T1-weighted gadolinium-enhanced MR sequences with use of an oral superparamagnetic contrast agent. *Radiology,* 238**,** 517-30.

Maccioni, F., A. Viscido, L. Broglia, M. Marrollo, R. Masciangelo, R. Caprilli & P. Rossi (2000) Evaluation of Crohn disease activity with magnetic resonance imaging. *Abdom Imaging,* 25**,** 219-28.

Maccioni, F., A. Viscido, M. Marini & R. Caprilli (2002) MRI evaluation of Crohn's disease of the small and large bowel with the use of negative superparamagnetic oral contrast agents. *Abdom Imaging,* 27**,** 384-93.

MacKenzie, S., N. Fernandez-Troy & E. Espel (2002) Post-transcriptional regulation of TNF-alpha during in vitro differentiation of human monocytes/macrophages in primary culture. *J Leukoc Biol,* 71**,** 1026-32.

Magro, F., P. Gionchetti, R. Eliakim, S. Ardizzone, A. Armuzzi, M. Barreiro-de Acosta, J. Burisch, K. B. Gecse, A. L. Hart, P. Hindryckx, C. Langner, J. K. Limdi, G. Pellino, E. Zagorowicz, T. Raine, M. Harbord, F. Rieder, C. s. European & O. Colitis (2017) Third European Evidence-based Consensus on Diagnosis and Management of Ulcerative Colitis. Part 1: Definitions, Diagnosis, Extra-intestinal Manifestations, Pregnancy, Cancer Surveillance, Surgery, and Ileo-anal Pouch Disorders. *J Crohns Colitis,* 11**,** 649-670.

Mak, K. M., C. Y. Png & D. J. Lee (2016) Type V Collagen in Health, Disease, and Fibrosis. *Anat Rec (Hoboken),* 299**,** 613-29.

Malhotra, N., J. S. Lee, R. A. D. Liman, J. M. S. Ruallo, O. B. Villaflores, T. R. Ger & C. D. Hsiao (2020) Potential Toxicity of Iron Oxide Magnetic Nanoparticles: A Review. *Molecules,* 25.

Maschmeyer, P., J. Zimmermann & A. A. Kuhl (2021) Murine T-Cell Transfer Colitis as a Model for Inflammatory Bowel Disease. *Methods Mol Biol,* 2285**,** 349-373.

Mathies, F., N. Steffens, D. Kleinschmidt, F. Stuhlmann, F. J. Huber, U. Roy, T. Meyer, M. Luetgehetmann, M. von Petersdorff, O. Seiz, J. Herkel, C. Schramm, R. A. Flavell, N. Gagliani, C. Krebs, U. Panzer, Z. Abdullah, T. Strowig, T. Bedke & S. Huber (2018) Colitis Promotes a Pathological Condition of the Liver in the Absence of Foxp3(+) Regulatory T Cells. *J Immunol,* 201**,** 3558-3568.

McBride, O. M., N. V. Joshi, J. M. Robson, T. J. MacGillivray, C. D. Gray, A. M. Fletcher, M. R. Dweck, E. J. van Beek, J. H. Rudd, D. E. Newby & S. I. Semple (2016) Positron Emission Tomography and Magnetic Resonance Imaging of Cellular Inflammation in Patients with Abdominal Aortic Aneurysms. *Eur J Vasc Endovasc Surg,* 51**,** 518-26.

McKaig, B. C., D. McWilliams, S. A. Watson & Y. R. Mahida (2003) Expression and regulation of tissue inhibitor of metalloproteinase-1 and matrix metalloproteinases by intestinal myofibroblasts in inflammatory bowel disease. *Am J Pathol,* 162**,** 1355-60.

McMahan, R. S., T. P. Birkland, K. S. Smigiel, T. C. Vandivort, M. G. Rohani, A. M. Manicone, J. K. McGuire, S. A. Gharib & W. C. Parks (2016) Stromelysin-2 (MMP10) Moderates Inflammation by Controlling Macrophage Activation. *J Immunol,* 197**,** 899-909.

Melgar, S., P. G. Gillberg, P. D. Hockings & L. E. Olsson (2007) High-throughput magnetic resonance imaging in murine colonic inflammation. *Biochem Biophys Res Commun,* 355**,** 1102-7.

Michael, S., L. M. Keubler, A. Smoczek, M. Meier, F. Gunzer, C. Pohlmann, U. Krause-Buchholz, H. J. Hedrich & A. Bleich (2013) Quantitative phenotyping of inflammatory bowel disease in the IL-10-deficient mouse by use of noninvasive magnetic resonance imaging. *Inflamm Bowel Dis,* 19**,** 185-93.

Millward, J. M., A. Ariza de Schellenberger, D. Berndt, L. Hanke-Vela, E. Schellenberger, S. Waiczies, M. Taupitz, Y. Kobayashi, S. Wagner & C. Infante-Duarte (2019) Application of Europium-Doped

Very Small Iron Oxide Nanoparticles to Visualize Neuroinflammation with MRI and Fluorescence Microscopy. *Neuroscience,* 403**,** 136-144.

Millward, J. M., J. Schnorr, M. Taupitz, S. Wagner, J. T. Wuerfel & C. Infante-Duarte (2013) Iron oxide magnetic nanoparticles highlight early involvement of the choroid plexus in central nervous system inflammation. *ASN Neuro,* 5**,** e00110.

Miner, J. H. (2008) Laminins and their roles in mammals. *Microsc Res Tech,* 71**,** 349-56.

Mizoguchi, A. (2012) Animal models of inflammatory bowel disease. *Prog Mol Biol Transl Sci,* 105**,** 263-320.

Mohamadzadeh, M., H. DeGrendele, H. Arizpe, P. Estess & M. Siegelman (1998) Proinflammatory stimuli regulate endothelial hyaluronan expression and CD44/HA-dependent primary adhesion. *J Clin Invest,* 101**,** 97-108.

Molodecky, N. A., I. S. Soon, D. M. Rabi, W. A. Ghali, M. Ferris, G. Chernoff, E. I. Benchimol, R. Panaccione, S. Ghosh, H. W. Barkema & G. G. Kaplan (2012) Increasing incidence and prevalence of the inflammatory bowel diseases with time, based on systematic review. *Gastroenterology,* 142**,** 46-54 e42; quiz e30.

Mortensen, J. H., M. Lindholm, L. L. Langholm, J. Kjeldsen, A. C. Bay-Jensen, M. A. Karsdal & T. Manon-Jensen (2019) The intestinal tissue homeostasis - the role of extracellular matrix remodeling in inflammatory bowel disease. *Expert Rev Gastroenterol Hepatol,* 13**,** 977-993.

Mulens-Arias, V., J. M. Rojas, S. Perez-Yague, M. P. Morales & D. F. Barber (2015) Polyethylenimine-coated SPIONs trigger macrophage activation through TLR-4 signaling and ROS production and modulate podosome dynamics. *Biomaterials,* 52**,** 494-506.

Mustafi, D., X. Fan, U. Dougherty, M. Bissonnette, G. S. Karczmar, A. Oto, J. Hart, E. Markiewicz & M. Zamora (2010) High-resolution magnetic resonance colonography and dynamic contrast-enhanced magnetic resonance imaging in a murine model of colitis. *Magn Reson Med,* 63**,** 922-9.

Na, Y. R., M. Stakenborg, S. H. Seok & G. Matteoli (2019) Macrophages in intestinal inflammation and resolution: a potential therapeutic target in IBD. *Nat Rev Gastroenterol Hepatol,* 16**,** 531-543.

Narasimhan, P. B., P. Marcovecchio, A. A. J. Hamers & C. C. Hedrick (2019) Nonclassical Monocytes in Health and Disease. *Annu Rev Immunol,* 37**,** 439-456.

Nasseri, M., S. Gahramanov, J. P. Netto, R. Fu, L. L. Muldoon, C. Varallyay, B. E. Hamilton & E. A. Neuwelt (2014) Evaluation of pseudoprogression in patients with glioblastoma multiforme using dynamic magnetic resonance imaging with ferumoxytol calls RANO criteria into question. *Neuro Oncol,* 16**,** 1146-54.

Negaard, A., V. Paulsen, L. Sandvik, A. E. Berstad, A. Borthne, K. Try, I. Lygren, T. Storaas & N. E. Klow (2007) A prospective randomized comparison between two MRI studies of the small bowel in Crohn's disease, the oral contrast method and MR enteroclysis. *Eur Radiol,* 17**,** 2294-301.

Nielsen, O. H., G. Rogler, D. Hahnloser & O. O. Thomsen (2009) Diagnosis and management of fistulizing Crohn's disease. *Nat Clin Pract Gastroenterol Hepatol,* 6**,** 92-106.

Nowicka, M., C. Krieg, H. L. Crowell, L. M. Weber, F. J. Hartmann, S. Guglietta, B. Becher, M. P. Levesque & M. D. Robinson (2017) CyTOF workflow: differential discovery in high-throughput high-dimensional cytometry datasets. *F1000Res,* 6**,** 748.

O'Shea, N. R. & A. M. Smith (2014) Matrix metalloproteases role in bowel inflammation and inflammatory bowel disease: an up to date review. *Inflamm Bowel Dis,* 20**,** 2379-93.

Ordas, I., L. Eckmann, M. Talamini, D. C. Baumgart & W. J. Sandborn (2012) Ulcerative colitis. *Lancet,* 380**,** 1606-19.

Oxford, J. T., J. C. Reeck & M. J. Hardy (2019) Extracellular Matrix in Development and Disease. *Int J Mol Sci,* 20.

Pabst, O., B. Wahl, G. Bernhardt & S. I. Hammerschmidt (2009) Mesenteric lymph node stroma cells in the generation of intestinal immune responses. *J Mol Med (Berl),* 87**,** 945-51.

Panes, J., R. Bouzas, M. Chaparro, V. Garcia-Sanchez, J. P. Gisbert, B. Martinez de Guerenu, J. L. Mendoza, J. M. Paredes, S. Quiroga, T. Ripolles & J. Rimola (2011) Systematic review: the use of ultrasonography, computed tomography and magnetic resonance imaging for the diagnosis, assessment of activity and abdominal complications of Crohn's disease. *Aliment Pharmacol Ther,* 34**,** 125-45.

Parsonage, G., A. D. Filer, O. Haworth, G. B. Nash, G. E. Rainger, M. Salmon & C. D. Buckley (2005) A stromal address code defined by fibroblasts. *Trends Immunol,* 26**,** 150-6.

Pasquini, L., A. Napolitano, E. Visconti, D. Longo, A. Romano, P. Toma & M. C. Rossi Espagnet (2018) Gadolinium-Based Contrast Agent-Related Toxicities. *CNS Drugs,* 32**,** 229-240.

Petrey, A. C. & C. A. de la Motte (2019) Hyaluronan in inflammatory bowel disease: Cross-linking inflammation and coagulation. *Matrix Biol,* 78-79**,** 314-323.

Pizarro, T. T., K. O. Arseneau & F. Cominelli (2000) Lessons from genetically engineered animal models XI. Novel mouse models to study pathogenic mechanisms of Crohn's disease. *Am J Physiol Gastrointest Liver Physiol,* 278**,** G665-9.

Pohland, M., C. Pohland, J. Kiwit & J. Glumm (2022) Magnetic labeling of primary murine monocytes using very small superparamagnetic iron oxide nanoparticles. *Neural Regen Res,* 17**,** 2311-2315.

Pohlmann, A., L. C. Tilling, A. Robinson, O. Woolmer, S. McCleary, L. Kruidenier, L. C. Warnock, H. D. Lewis, A. R. Hobson & M. F. James (2009) Progression and variability of TNBS colitis-associated inflammation in rats assessed by contrast-enhanced and T2-weighted MRI. *Inflamm Bowel Dis,* 15**,** 534-45.

Poller, W. C., N. Lowa, F. Wiekhorst, M. Taupitz, S. Wagner, K. Moller, G. Baumann, V. Stangl, L. Trahms & A. Ludwig (2016) Magnetic Particle Spectroscopy Reveals Dynamic Changes in the Magnetic Behavior of Very Small Superparamagnetic Iron Oxide Nanoparticles During Cellular Uptake and Enables Determination of Cell-Labeling Efficacy. *J Biomed Nanotechnol,* 12**,** 337-46.

Powrie, F. & D. Mason (1990) OX-22high CD4+ T cells induce wasting disease with multiple organ pathology: prevention by the OX-22low subset. *J Exp Med,* 172**,** 1701-8.

Puhakka, K. B., A. G. Jurik, B. Schiottz-Christensen, G. V. Hansen, N. Egund, J. V. Christiansen & K. Stengaard-Pedersen (2004) MRI abnormalities of sacroiliac joints in early spondylarthropathy: a 1-year follow-up study. *Scand J Rheumatol,* 33**,** 332-8.

Qiu, Y., R. Mao, B. L. Chen, X. H. Li, Y. He, Z. R. Zeng, Z. P. Li & M. H. Chen (2014) Systematic review with meta-analysis: magnetic resonance enterography vs. computed tomography enterography for evaluating disease activity in small bowel Crohn's disease. *Aliment Pharmacol Ther,* 40**,** 134-46.

Rackov, G., E. Hernandez-Jimenez, R. Shokri, L. Carmona-Rodriguez, S. Manes, M. Alvarez-Mon, E. Lopez-Collazo, A. C. Martinez & D. Balomenos (2016) p21 mediates macrophage reprogramming through regulation of p50-p50 NF-kappaB and IFN-beta. *J Clin Invest,* 126**,** 3089-103.

Radeloff, K., A. Radeloff, M. Ramos Tirado, A. Scherzad, R. Hagen, N. H. Kleinsasser & S. Hackenberg (2020) Toxicity and Functional Impairment in Human Adipose Tissue-Derived Stromal Cells (hASCs) Following Long-Term Exposure to Very Small Iron Oxide Particles (VSOPs). *Nanomaterials (Basel),* 10.

Radeloff, K., M. Ramos Tirado, D. Haddad, K. Breuer, J. Muller, S. Hochmuth, S. Hackenberg, A. Scherzad, N. Kleinsasser & A. Radeloff (2021) Superparamagnetic Iron Oxide Particles (VSOPs) Show Genotoxic Effects but No Functional Impact on Human Adipose Tissue-Derived Stromal Cells (ASCs). *Materials (Basel),* 14.

Randolph, G. J., S. Ivanov, B. H. Zinselmeyer & J. P. Scallan (2017) The Lymphatic System: Integral Roles in Immunity. *Annu Rev Immunol,* 35**,** 31-52.

Ricard-Blum, S., G. Baffet & N. Theret (2018) Molecular and tissue alterations of collagens in fibrosis. *Matrix Biol,* 68-69**,** 122-149.

Rieder, F., J. Brenmoehl, S. Leeb, J. Scholmerich & G. Rogler (2007) Wound healing and fibrosis in intestinal disease. *Gut,* 56**,** 130-9.

Rieder, F., E. M. Zimmermann, F. H. Remzi & W. J. Sandborn (2013) Crohn's disease complicated by strictures: a systematic review. *Gut,* 62**,** 1072-84.

Rogler, G., A. Singh, A. Kavanaugh & D. T. Rubin (2021) Extraintestinal Manifestations of Inflammatory Bowel Disease: Current Concepts, Treatment, and Implications for Disease Management. *Gastroenterology,* 161**,** 1118-1132.

Rossato, M., G. Curtale, N. Tamassia, M. Castellucci, L. Mori, S. Gasperini, B. Mariotti, M. De Luca, M. Mirolo, M. A. Cassatella, M. Locati & F. Bazzoni (2012) IL-10-induced microRNA-187 negatively regulates TNF-alpha, IL-6, and IL-12p40 production in TLR4-stimulated monocytes. *Proc Natl Acad Sci U S A,* 109**,** E3101-10.

Rutella, S. & F. Locatelli (2011) Intestinal dendritic cells in the pathogenesis of inflammatory bowel disease. *World J Gastroenterol,* 17**,** 3761-75.

Schafer, R., R. Kehlbach, J. Wiskirchen, R. Bantleon, J. Pintaske, B. R. Brehm, A. Gerber, H. Wolburg, C. D. Claussen & H. Northoff (2007) Transferrin receptor upregulation: in vitro labeling of rat mesenchymal stem cells with superparamagnetic iron oxide. *Radiology,* 244**,** 514-23.

Scharlach, C., L. Muller, S. Wagner, Y. Kobayashi, H. Kratz, M. Ebert, N. Jakubowski & E. Schellenberger (2016) LA-ICP-MS Allows Quantitative Microscopy of Europium-Doped Iron

Oxide Nanoparticles and is a Possible Alternative to Ambiguous Prussian Blue Iron Staining. *J Biomed Nanotechnol,* 12**,** 1001-10.

Scheibe, K., C. Kersten, A. Schmied, M. Vieth, T. Primbs, B. Carle, F. Knieling, J. Claussen, A. C. Klimowicz, J. Zheng, P. Baum, S. Meyer, S. Schurmann, O. Friedrich, M. J. Waldner, T. Rath, S. Wirtz, G. Kollias, A. B. Ekici, R. Atreya, E. L. Raymond, M. L. Mbow, M. F. Neurath & C. Neufert (2019) Inhibiting Interleukin 36 Receptor Signaling Reduces Fibrosis in Mice With Chronic Intestinal Inflammation. *Gastroenterology,* 156**,** 1082-1097 e11.

Schellenberger, E., F. Rudloff, C. Warmuth, M. Taupitz, B. Hamm & J. Schnorr (2008a) Protease-specific nanosensors for magnetic resonance imaging. *Bioconjug Chem,* 19**,** 2440-5.

Schellenberger, E., J. Schnorr, C. Reutelingsperger, L. Ungethum, W. Meyer, M. Taupitz & B. Hamm (2008b) Linking proteins with anionic nanoparticles via protamine: ultrasmall protein-coupled probes for magnetic resonance imaging of apoptosis. *Small,* 4**,** 225-30.

Schnorr, J., S. Wagner, C. Abramjuk, R. Drees, T. Schink, E. A. Schellenberger, H. Pilgrimm, B. Hamm & M. Taupitz (2006) Focal liver lesions: SPIO-, gadolinium-, and ferucarbotran-enhanced dynamic T1-weighted and delayed T2-weighted MR imaging in rabbits. *Radiology,* 240**,** 90-100.

Schnorr, J., S. Wagner, C. Abramjuk, I. Wojner, T. Schink, T. J. Kroencke, E. Schellenberger, B. Hamm, H. Pilgrimm & M. Taupitz (2004) Comparison of the iron oxide-based blood-pool contrast medium VSOP-C184 with gadopentetate dimeglumine for first-pass magnetic resonance angiography of the aorta and renal arteries in pigs. *Invest Radiol,* 39**,** 546-53.

Schnorr, J., S. Wagner, H. Pilgrimm, B. Hamm & M. Taupitz (2002) Preclinical characterization of monomer-stabilized very small superparamagnetic iron oxide particles (VSOP) as a blood pool contrast medium for MR angiography. *Acad Radiol,* 9 Suppl 2**,** S307-9.

Shaban, N., C. L. Hoad, I. Naim, M. Alshammari, S. J. Radford, C. Clarke, L. Marciani & G. Moran (2022) Imaging in inflammatory bowel disease: current and future perspectives. *Frontline Gastroenterol,* 13**,** e28-e34.

Sharma, A., C. Cornejo, J. Mihalic, A. Geyh, D. E. Bordelon, P. Korangath, F. Westphal, C. Gruettner & R. Ivkov (2018) Physical characterization and in vivo organ distribution of coated iron oxide nanoparticles. *Sci Rep,* 8**,** 4916.

Silva, R. V., A. S. Morr, S. Mueller, S. P. Koch, P. Boehm-Sturm, Y. Rodriguez-Sillke, D. Kunkel, H. Tzschatzsch, A. A. Kuhl, J. Schnorr, M. Taupitz, I. Sack & C. Infante-Duarte (2021) Contribution of Tissue Inflammation and Blood-Brain Barrier Disruption to Brain Softening in a Mouse Model of Multiple Sclerosis. *Front Neurosci,* 15**,** 701308.

Singh, N., G. J. Jenkins, R. Asadi & S. H. Doak (2010) Potential toxicity of superparamagnetic iron oxide nanoparticles (SPION). *Nano Rev,* 1.

Sinha, R., P. Murphy, P. Hawker, S. Sanders, A. Rajesh & R. Verma (2009) Role of MRI in Crohn's disease. *Clin Radiol,* 64**,** 341-52.

Soenen, S. J., U. Himmelreich, N. Nuytten & M. De Cuyper (2011) Cytotoxic effects of iron oxide nanoparticles and implications for safety in cell labelling. *Biomaterials,* 32**,** 195-205.

Soenen, S. J., N. Nuytten, S. F. De Meyer, S. C. De Smedt & M. De Cuyper (2010) High intracellular iron oxide nanoparticle concentrations affect cellular cytoskeleton and focal adhesion kinase-mediated signaling. *Small,* 6**,** 832-42.

Song, Y., F. Zhang & R. J. Linhardt (2021) Glycosaminoglycans. *Adv Exp Med Biol,* 1325**,** 103-116.

Sorushanova, A., L. M. Delgado, Z. Wu, N. Shologu, A. Kshirsagar, R. Raghunath, A. M. Mullen, Y. Bayon, A. Pandit, M. Raghunath & D. I. Zeugolis (2019) The Collagen Suprafamily: From Biosynthesis to Advanced Biomaterial Development. *Adv Mater,* 31**,** e1801651.

Spenle, C., T. Hussenet, J. Lacroute, O. Lefebvre, M. Kedinger, G. Orend & P. Simon-Assmann (2012) Dysregulation of laminins in intestinal inflammation. *Pathol Biol (Paris),* 60**,** 41-7.

Stroh, A., C. Faber, T. Neuberger, P. Lorenz, K. Sieland, P. M. Jakob, A. Webb, H. Pilgrimm, R. Schober, E. E. Pohl & C. Zimmer (2005) In vivo detection limits of magnetically labeled embryonic stem cells in the rat brain using high-field (17.6 T) magnetic resonance imaging. *Neuroimage,* 24**,** 635-45.

Stroh, A., J. Kressel, R. Coras, A. Y. Dreyer, W. Frohlich, A. Forschler, D. Lobsien, I. Blumcke, S. Zoubaa, J. Schlegel, C. Zimmer & J. Boltze (2019) A Safe and Effective Magnetic Labeling Protocol for MRI-Based Tracking of Human Adult Neural Stem Cells. *Front Neurosci,* 13**,** 1092.

Stroh, A., C. Zimmer, N. Werner, K. Gertz, K. Weir, G. Kronenberg, J. Steinbrink, S. Mueller, K. Sieland, U. Dirnagl, G. Nickenig & M. Endres (2006) Tracking of systemically administered mononuclear cells in the ischemic brain by high-field magnetic resonance imaging. *Neuroimage,* 33**,** 886-97.

Sun, T., A. Nguyen & J. L. Gommerman (2020) Dendritic Cell Subsets in Intestinal Immunity and Inflammation. *J Immunol,* 204**,** 1075-1083.

Swaminathan, S. (2016) Gadolinium toxicity: Iron and ferroportin as central targets. *Magn Reson Imaging,* 34**,** 1373-1376.

Tahir, S. & S. Steffens (2021) Nonclassical monocytes in cardiovascular physiology and disease. *Am J Physiol Cell Physiol,* 320**,** C761-C770.

Tang, X., F. Cai, D. X. Ding, L. L. Zhang, X. Y. Cai & Q. Fang (2018) Magnetic resonance imaging relaxation time in Alzheimer's disease. *Brain Res Bull,* 140**,** 176-189.

Taupitz, M., J. Schnorr, C. Abramjuk, S. Wagner, H. Pilgrimm, H. Hunigen & B. Hamm (2000) New generation of monomer-stabilized very small superparamagnetic iron oxide particles (VSOP) as contrast medium for MR angiography: preclinical results in rats and rabbits. *J Magn Reson Imaging,* 12**,** 905-11.

Taupitz, M., J. Schnorr, S. Wagner, C. Abramjuk, H. Pilgrimm, D. Kivelitz, T. Schink, J. Hansel, G. Laub, H. Hunigen & B. Hamm (2002) Coronary MR angiography: experimental results with a monomer-stabilized blood pool contrast medium. *Radiology,* 222**,** 120-6.

Taupitz, M., S. Wagner, J. Schnorr, I. Kravec, H. Pilgrimm, H. Bergmann-Fritsch & B. Hamm (2004) Phase I clinical evaluation of citrate-coated monocrystalline very small superparamagnetic iron oxide particles as a new contrast medium for magnetic resonance imaging. *Invest Radiol,* 39**,** 394-405.

Thakor, A. S., J. V. Jokerst, P. Ghanouni, J. L. Campbell, E. Mittra & S. S. Gambhir (2016) Clinically Approved Nanoparticle Imaging Agents. *J Nucl Med,* 57**,** 1833-1837.

Torres, J., S. Mehandru, J. F. Colombel & L. Peyrin-Biroulet (2017) Crohn's disease. *Lancet,* 389**,** 1741-1755.

Tysiak, E., P. Asbach, O. Aktas, H. Waiczies, M. Smyth, J. Schnorr, M. Taupitz & J. Wuerfel (2009) Beyond blood brain barrier breakdown - in vivo detection of occult neuroinflammatory foci by magnetic nanoparticles in high field MRI. *J Neuroinflammation,* 6**,** 20.

Uca, Y. O., D. Hallmann, B. Hesse, C. Seim, N. Stolzenburg, H. Pietsch, J. Schnorr & M. Taupitz (2021) Microdistribution of Magnetic Resonance Imaging Contrast Agents in Atherosclerotic Plaques Determined by LA-ICP-MS and SR-muXRF Imaging. *Mol Imaging Biol,* 23**,** 382-393.

Varol, C., E. Zigmond & S. Jung (2010) Securing the immune tightrope: mononuclear phagocytes in the intestinal lamina propria. *Nat Rev Immunol,* 10**,** 415-26.

Volpi, N., F. Galeotti, B. Yang & R. J. Linhardt (2014) Analysis of glycosaminoglycan-derived, precolumn, 2-aminoacridone-labeled disaccharides with LC-fluorescence and LC-MS detection. *Nat Protoc,* 9**,** 541-58.

von Lampe, B., B. Barthel, S. E. Coupland, E. O. Riecken & S. Rosewicz (2000) Differential expression of matrix metalloproteinases and their tissue inhibitors in colon mucosa of patients with inflammatory bowel disease. *Gut,* 47**,** 63-73.

Wagner, M., S. Wagner, J. Schnorr, E. Schellenberger, D. Kivelitz, L. Krug, M. Dewey, M. Laule, B. Hamm & M. Taupitz (2011) Coronary MR angiography using citrate-coated very small superparamagnetic iron oxide particles as blood-pool contrast agent: initial experience in humans. *J Magn Reson Imaging,* 34**,** 816-23.

Wagner, S., J. Schnorr, A. Ludwig, V. Stangl, M. Ebert, B. Hamm & M. Taupitz (2013) Contrast-enhanced MR imaging of atherosclerosis using citrate-coated superparamagnetic iron oxide nanoparticles: calcifying microvesicles as imaging target for plaque characterization. *Int J Nanomedicine,* 8**,** 767-79.

Wagner, S., J. Schnorr, H. Pilgrimm, B. Hamm & M. Taupitz (2002) Monomer-coated very small superparamagnetic iron oxide particles as contrast medium for magnetic resonance imaging: preclinical in vivo characterization. *Invest Radiol,* 37**,** 167-77.

Waisman, A., D. Lukas, B. E. Clausen & N. Yogev (2017) Dendritic cells as gatekeepers of tolerance. *Semin Immunopathol,* 39**,** 153-163.

Walldorf, J., M. Hermann, M. Porzner, S. Pohl, H. Metz, K. Mader, A. Zipprich, B. Christ & T. Seufferlein (2015) In-vivo monitoring of acute DSS-Colitis using Colonoscopy, high resolution Ultrasound and bench-top Magnetic Resonance Imaging in Mice. *Eur Radiol,* 25**,** 2984-91.

Wang, S., B. Hesse, M. Roman, D. Stier, H. Castillo-Michel, M. Cotte, J. P. Suuronen, A. Lagrange, H. Radbruch, F. Paul, M. Taupitz, E. Schellenberger, I. Sack & C. Infante-Duarte (2019) Increased Retention of Gadolinium in the Inflamed Brain After Repeated Administration of Gadopentetate Dimeglumine: A Proof-of-Concept Study in Mice Combining ICP-MS and Micro- and Nano-SR-XRF. *Invest Radiol,* 54**,** 617-626.

Wang, Y., E. C. Song & M. B. Resnick (2020) Elastin in the Tumor Microenvironment. *Adv Exp Med Biol,* 1272**,** 1-16.

Weinstein, J. S., C. G. Varallyay, E. Dosa, S. Gahramanov, B. Hamilton, W. D. Rooney, L. L. Muldoon & E. A. Neuwelt (2010) Superparamagnetic iron oxide nanoparticles: diagnostic magnetic resonance imaging and potential therapeutic applications in neurooncology and central nervous system inflammatory pathologies, a review. *J Cereb Blood Flow Metab,* 30**,** 15-35.

White, G. W., W. A. Gibby & M. F. Tweedle (2006) Comparison of Gd(DTPA-BMA) (Omniscan) versus Gd(HP-DO3A) (ProHance) relative to gadolinium retention in human bone tissue by inductively coupled plasma mass spectroscopy. *Invest Radiol,* 41**,** 272-8.

Wu, R. Q., D. F. Zhang, E. Tu, Q. M. Chen & W. Chen (2014) The mucosal immune system in the oral cavity-an orchestra of T cell diversity. *Int J Oral Sci,* 6**,** 125-32.

Xavier, R. J. & D. K. Podolsky (2007) Unravelling the pathogenesis of inflammatory bowel disease. *Nature,* 448**,** 427-34.

Xie, H., Y. Jiao, X. Zhou, X. Liao, J. Chen, H. Chen, L. Chen, S. Yu, Q. Deng, L. Sun, X. Xu & J. Wang (2022) Integrin alphavbeta6 contributes to the development of intestinal fibrosis via the FAK/AKT signaling pathway. *Exp Cell Res,* 411**,** 113003.

Yablecovitch, D., A. Stein, M. Shabat-Simon, T. Naftali, G. Gabay, I. Laish, A. Oren & F. M. Konikoff (2015) Soluble Syndecan-1 Levels Are Elevated in Patients with Inflammatory Bowel Disease. *Dig Dis Sci,* 60**,** 2419-26.

Yilmaz, A., M. A. Dengler, H. van der Kuip, H. Yildiz, S. Rosch, S. Klumpp, K. Klingel, R. Kandolf, X. Helluy, K. H. Hiller, P. M. Jakob & U. Sechtem (2013) Imaging of myocardial infarction using ultrasmall superparamagnetic iron oxide nanoparticles: a human study using a multi-parametric cardiovascular magnetic resonance imaging approach. *Eur Heart J,* 34**,** 462-75.

Yona, S., K. W. Kim, Y. Wolf, A. Mildner, D. Varol, M. Breker, D. Strauss-Ayali, S. Viukov, M. Guilliams, A. Misharin, D. A. Hume, H. Perlman, B. Malissen, E. Zelzer & S. Jung (2013) Fate mapping reveals origins and dynamics of monocytes and tissue macrophages under homeostasis. *Immunity,* 38**,** 79-91.

Yousaf, T., G. Dervenoulas & M. Politis (2018) Advances in MRI Methodology. *Int Rev Neurobiol,* 141**,** 31-76.

Yu, L. L., H. S. Yang, B. T. Zhang, Z. W. Lv, F. R. Wang, C. Y. Zhang, W. B. Chen & H. M. Zhang (2015) Diffusion-weighted magnetic resonance imaging without bowel preparation for detection of ulcerative colitis. *World J Gastroenterol,* 21**,** 9785-92.

Zanganeh, S., G. Hutter, R. Spitler, O. Lenkov, M. Mahmoudi, A. Shaw, J. S. Pajarinen, H. Nejadnik, S. Goodman, M. Moseley, L. M. Coussens & H. E. Daldrup-Link (2016) Iron oxide nanoparticles inhibit tumour growth by inducing pro-inflammatory macrophage polarization in tumour tissues. *Nat Nanotechnol,* 11**,** 986-994.

Zhang, W., S. Cao, S. Liang, C. H. Tan, B. Luo, X. Xu & P. E. Saw (2020) Differently Charged Super-Paramagnetic Iron Oxide Nanoparticles Preferentially Induced M1-Like Phenotype of Macrophages. *Front Bioeng Biotechnol,* 8**,** 537.

Zhang, Y. Z. & Y. Y. Li (2014) Inflammatory bowel disease: pathogenesis. *World J Gastroenterol,* 20**,** 91-9.

Zhao, M., L. Gonczi, P. L. Lakatos & J. Burisch (2021) The Burden of Inflammatory Bowel Disease in Europe in 2020. *J Crohns Colitis,* 15**,** 1573-1587.

Ziegler-Heitbrock, L., P. Ancuta, S. Crowe, M. Dalod, V. Grau, D. N. Hart, P. J. Leenen, Y. J. Liu, G. MacPherson, G. J. Randolph, J. Scherberich, J. Schmitz, K. Shortman, S. Sozzani, H. Strobl, M. Zembala, J. M. Austyn & M. B. Lutz (2010) Nomenclature of monocytes and dendritic cells in blood. *Blood,* 116**,** e74-80.

Zimmermann, J., A. A. Kuhl, M. Weber, J. R. Grun, J. Loffler, C. Haftmann, R. Riedel, P. Maschmeyer, K. Lehmann, K. Westendorf, M. F. Mashreghi, M. Lohning, M. Mack, A. Radbruch & H. D. Chang (2016) T-bet expression by Th cells promotes type 1 inflammation but is dispensable for colitis. *Mucosal Immunol,* 9**,** 1487-1499.

8 APPENDIX

8.1 Publications

Parts of this work are published in:

Visualization of Inflammation in Experimental Colitis by Magnetic Resonance Imaging Using Very Small Superparamagnetic Iron Oxide Particles. Laura Golusda*, Anja A. Kühl*, Malte Lehmann, Katja Dahlke, Susanne Mueller, Philipp Boehm-Sturm, Jessica Saatz, Heike Traub, Joerg Schnorr, Christian Freise, Matthias Taupitz, Karina Biskup, Véronique Blanchard, Oliver Klein, Ingolf Sack, Britta Siegmund, Daniela Packlik, * these authors contributed equally. *Front. Physiol.,* **July 2022**, https://www.frontiersin.org/articles/10.3389/fphys.2022.862212/full

Additional Publications

Reducing Pain in Experimental Models of Intestinal Inflammation Affects the Immune Response. Laura Golusda, Anja A. Kühl, Britta Siegmund, Daniela Paclik. *Inflammatory Bowel Diseases, Volume 28, Issue 5*, **December 2021**, https://doi.org/10.1093/ibd/izab290

Extracellular Matrix Components as Diagnostic Tools in Inflammatory Bowel Disease. Laura Golusda, Anja A. Kühl, Britta Siegmund, Daniela Paclik. *Biology*, **October 2021**, https://doi.org/10.3390/biology10101024

Deficiency in IκBα in the intestinal epithelium leads to spontaneous inflammation and mediates apoptosis in the gut. Nadine Mikuda, Ruth Schmidt-Ullrich, Eva Krägel, Laura Golusda, Jana Wolf, Uta E. Höpken, Claus Scheidereit, Anja A. Kühl, Marina Kolesnichenko. *J Pathol., Volume 251, Issue 2*, **June 2020**, https://doi.org/10.3390/biology10101024

8.2 Supplementary figures
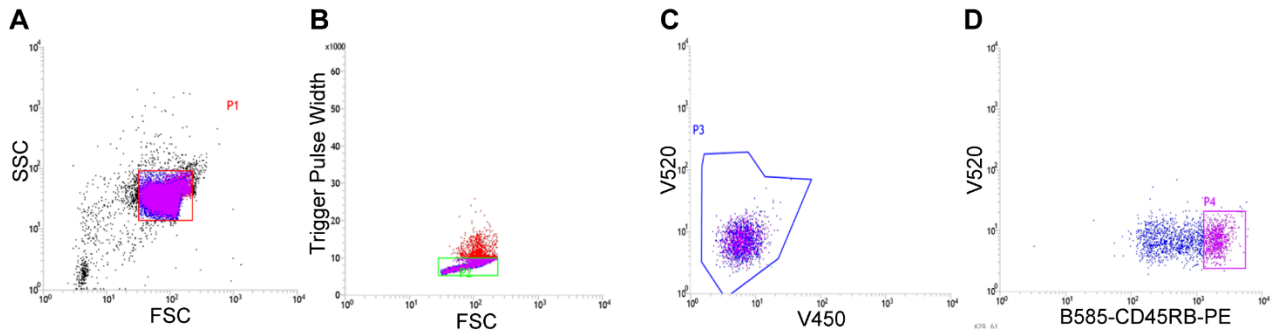
Supplementary Figure 1: <u>Gating strategy for sorting CD4$^+$CD45RB^{high} T cells for the transfer colitis mouse model.</u> CD4$^+$ T cells isolated from spleen of wild type mice were sorted with FACSJazz^{TM} by gating on cells **(A)**, single cells **(B)**, living cells **(C)** and gated on cells highly expressing CD45RB **(D)**.
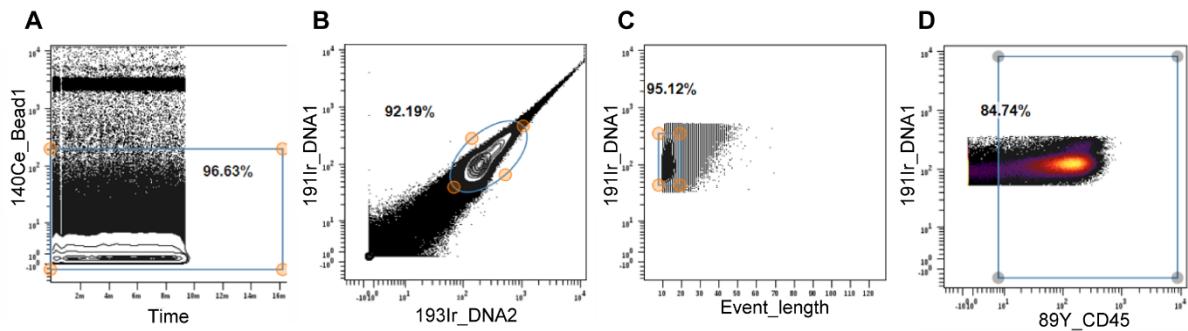
Supplementary Figure 2: <u>Gating strategy for CyTOF experiments.</u> Samples were gated cells **(A)**, single cells **(B)** and single **(C)**. After debarcoding and normalization all files were gated on CD45$^+$ cells for further analysis **(D)**.